January 2016

X-Ray Absorption Spectroscopy Studies Of The Atomic Structure Of Zirconium-Doped Lithium Silicate Glasses And Glass-Ceramics, Zirconium-Doped Lithium Borate Glasses, And Vitreous Rare-Earth Phosphates

Changhyeon Yoo

X-RAY ABSORPTION SPECTROSCOPY STUDIES OF THE ATOMIC STRUCTURE
OF ZIRCONIUM-DOPED LITHIUM SILICATE GLASSES AND GLASS-
CERAMICS, ZIRCONIUM-DOPED LITHIUM BORATE GLASSES, AND
VITREOUS RARE-EARTH PHOSPHATES

by

Changhyeon Yoo
Bachelor of Science, Seoul National University – South Korea, 2003
Master of Science, University of Massachusetts Lowell, 2010

A Dissertation

Submitted to the Graduate Faculty

of the

University of North Dakota

in partial fulfillment of the requirements
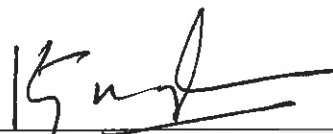
for the degree of

Doctor of Philosophy

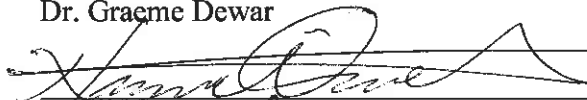Grand Forks, North Dakota

August
2016

This dissertation, submitted by Changhyeon Yoo in partial fulfillment of the requirements for the degree of Doctor of Philosophy from the University of North Dakota, has been read by the Faculty Advisory Committee under whom the work has been done and is hereby approved.

_____
Dr. Kanishka Marasinghe

_____
Dr. Graeme Dewar

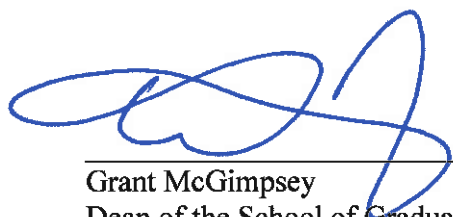_____
Dr. Nuri Öncel

_____
Dr. Yen Lee Loh

_____
Dr. Lothar Stahl

This dissertation is being submitted by the appointed advisory committee as having met all of the requirements of the School of Graduate Studies at the University of North Dakota and is hereby approved.

_____
Grant McGimpsey
Dean of the School of Graduate Studies

_____July 26, 2016_____
Date

iii

PERMISSION

Title	X-Ray Absorption Spectroscopy Studies of the Atomic Structure of Zirconium-Doped Lithium Silicate Glasses and Glass-Ceramics, Zirconium-Doped Lithium Borate Glasses, and Vitreous Rare-Earth Phosphates
Department	Physics and Astrophysics
Degree	Doctor of Philosophy

In presenting this dissertation in partial fulfillment of the requirements for a graduate degree from the University of North Dakota, I agree that the library of this University shall make it freely available for inspection. I further agree that permission for extensive copying for scholarly purposes may be granted by the professor who supervised my dissertation work or, in his absence, by the Chairperson of the department or the dean of the School of Graduate Studies. It is understood that any copying or publication or other use of this dissertation or part thereof for financial gain shall not be allowed without my written permission. It is also understood that due recognition shall be given to me and to the University of North Dakota in any scholarly use which may be made of any material in my dissertation.

Changhyeon Yoo
July 25, 2016

TABLE OF CONTENTS

LIST OF FIGURES

LIST OF TABLES

ACKNOWLEDGMENTS

To my mom, my dad, and my sister.

Be happy and healthy.

ABSTRACT

In the first part of this work, the atomic-scale structure around rare-earth (RE = Pr, Nd, Eu, Dy, and Er) cations (RE^{3+}) in rare-earth sodium ultraphosphate (REUP) glasses were investigated using RE L_{III}-edge (RE = Nd, Er, Dy, and Eu) and K-edge (RE = Pr and Dy) Extended X-ray Absorption Fine Structure (EXAFS) spectroscopy. $(RE_2O_3)_x(Na_2O)_y(P_2O_5)_{1-x-y}$ glasses in the compositional range $0 \leq x \leq 0.14$ and $0.3 \leq x + y \leq 0.4$ were studied. For the nearest oxygen shell, the RE-oxygen (RE-O) coordination number decreases from 10.8 to 6.5 with increasing RE content for Pr-, Nd-, Dy-, and Er-doped sodium ultraphosphate glasses. For Eu-doped samples, the Eu-O coordination number was between 7.5 and 8.8. Also, the RE-O mean distance ranges were between 2.43–2.45 Å, 2.40–2.43 Å, 2.36–2.38 Å, 2.30–2.35 Å, and 2.28–2.30 Å for Pr-, Nd-, Eu-, Dy-, and Er-doped samples, respectively.

In the second part, a series of Zr-doped (3–10 mol%) lithium silicate (ZRLS) glass-ceramics and their parent glasses and a series of Zr-doped (2–6 mol% ZrO_2) lithium borate (ZRLB) glasses were investigated using Zr K-edge EXAFS and X-ray Absorption Near Edge Structure (XANES) spectroscopy. Immediate coordination environments of all ZRLS glasses are remarkably similar for different compositions. For the nearest oxygen shell, the Zr-O coordination number ranges were between 6.1 and 6.3 for nucleated and crystallized samples, respectively. Also, the Zr-O mean distance remains similar around 2.10 Å. For these glasses, the composition dependence of structural parameters was

small. Small changes in the coordination environment were observed for ZRLS glass-ceramics after thermal treatments.

In contrast, Zr coordination environment in ZRLB glasses appear to depend appreciably on the Zr concentration. For the nearest oxygen shell, the Zr-O coordination number increased from 6.1 to 6.8 and the Zr-O distance decreased from 2.18 Å to 2.14 Å with decreasing ZrO_2 content.

CHAPTER I

INTRODUCTION

Glass is commonly described as a fusion product of inorganic materials which lacks long range periodicity at the atomic scale [1, 2]. Most common oxide glasses are processed from good glass formers such as silica (SiO_2), boron trioxide (B_2O_3), and phosphorus pentoxide (P_2O_5). Such good glass formers form single component glasses when quenched from a melt under normal conditions, *i.e.* rapidly cooling a melt at a rate high enough (usually a few hundred ºC/s) to avoid crystallization [1, 2].

Rare-earth (RE) elements play an important role in modern optical technology. For example, rare-earth doped (RE_2O_3) oxide glasses have applications in optical devices, such as high power lasers and amplifiers in fiber-optic communication [3]. Specifically, lanthanides readily show easy population inversion because of their unfilled $4f^n$ shell ground electronic configuration making them candidates for three or four level lasing schemes as shown in **Figure 1** [3, 5, 6].
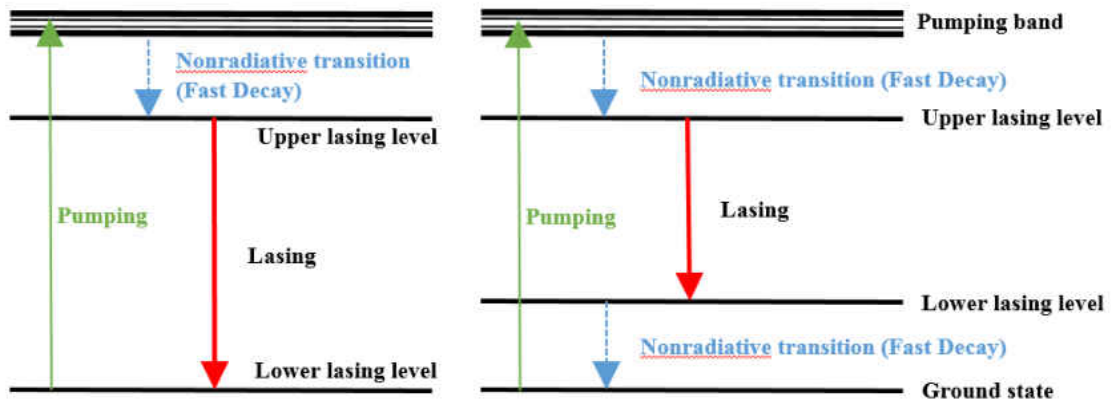
Figure 1. Three- (left) and four-level laser schemes (right).

Most common RE-doped oxide glasses are phosphate and silicate glasses. Certain characteristics of RE-doped phosphate glasses make them attractive for a range of applications. They have lower dispersions, relatively lower refractive indices and low absorption losses in the UV to infrared spectral region than silicate glasses. Also, they can be prepared at moderate temperatures and have low production costs. Other applications of phosphate glasses include special hermetic seals for lithium-ion batteries due to their high thermal expansion coefficients, nuclear waste storage hosts due to their chemical durability, and medical applications due to their bio-compatible nature [3, 4]. Rare-earth phosphate glasses have been widely explored as a gain medium in optically pumped high energy solid-state lasers [3, 5]. Adding RE modifiers (or dopants) to phosphate glasses significantly changes their chemical and optical properties. For example, RE-doped phosphate glasses can be used as gain media for high energy (10^3–10^6 J) / high peak power (10^{12}–10^{15} W) lasers because they have large stimulated emission cross sections due to lasing RE^{3+} cations and low thermo-optical coefficients [3, 5, 6].

When compared to crystals, glasses have broader emission lines which enable the laser threshold to increase by stretching and compressing the emission spectra during the amplification [3]. As a result, they store large amounts of energy in excited states making it possible to significantly amplify short light pulses [7]. Also, glasses are optically isotropic and their good mechanical and chemical durability are suitable for optical components that require a good optical surface. The low production cost, mechanical and chemical hardness, fusibility with other glasses, and ability to tune properties using modifiers and dopants are some of the main positive characteristics of glasses over crystals [2].

When the RE concentration is high, the separations between RE^{3+} cations are small and the probability of non-radiative energy transfer between RE^{3+} cations increases. Non-radiative losses, such as concentration quenching due to RE^{3+}–RE^{3+} interactions and multiphonon absorption which are classified as intrinsic processes will decrease the lasing efficiency. RE-doped phosphate glasses classified as metaphosphates (oxygen/phosphorus ([O] / [P]) ratio = 3.0) and ultraphosphates ([O] / [P] < 3) have shown to be good lasing media because the population inversion in RE^{3+} cations is large [7, 8]. Also, the separation between RE^{3+} cations is also large, which reduces non-radiative processes. **Figure 2** illustrates intrinsic processes that depend on the glass structure during manufacturing and extrinsic processes that depend on impurities for Nd-doped glasses [3].
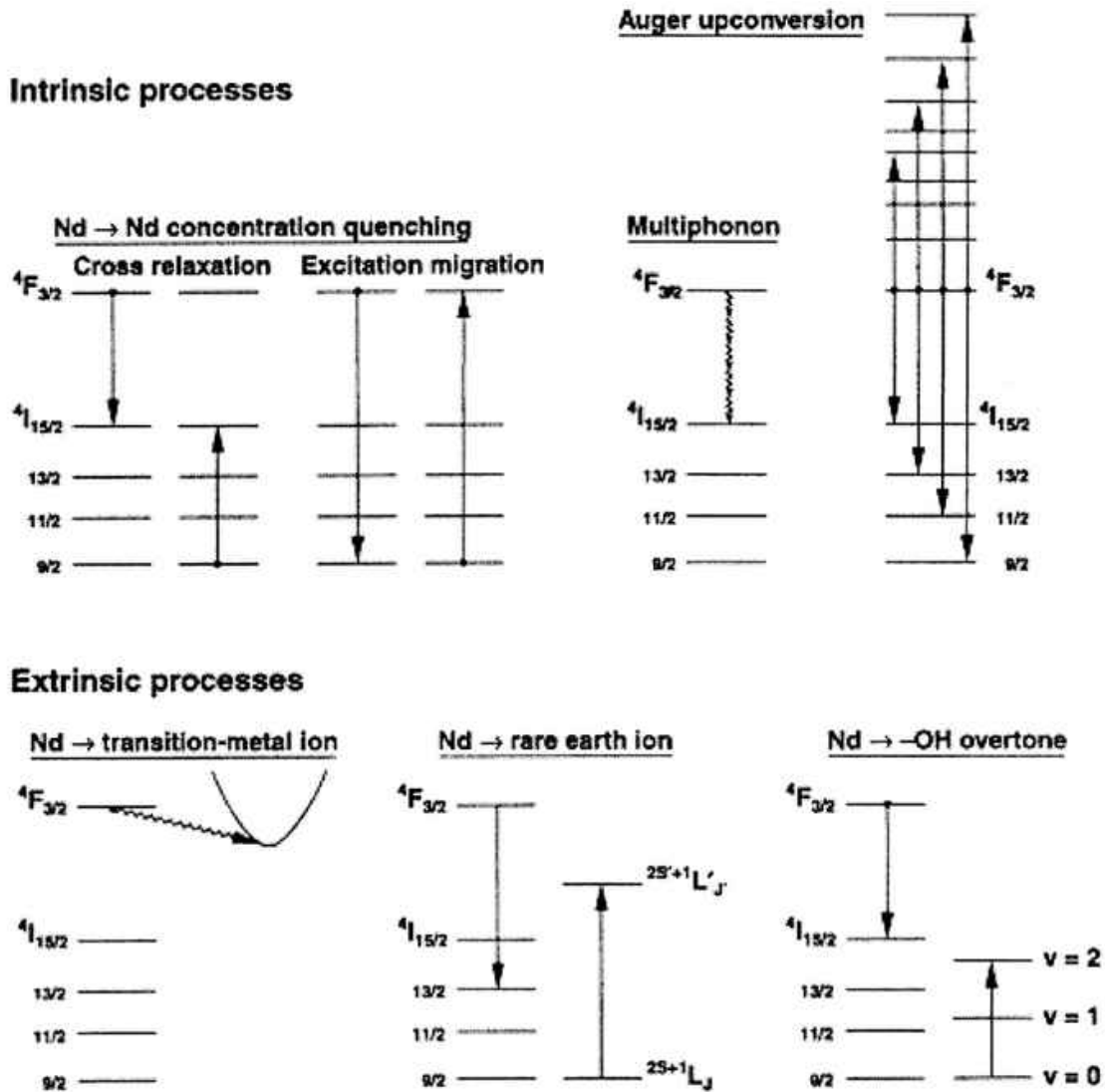
Figure 2. Non-radiative energy transitions between two nearby Nd^{3+} cations (top), multiphonon interactions (top), and a Nd^{3+} cation with others (bottom) [3].

Two undesired properties of phosphate glasses are their hygroscopic nature and the partial loss of P_2O_5 during melting [9]. RE-doped phosphate glasses containing relatively large amounts (> 80 mol%) of P_2O_5 are known to absorb water from the surrounding environment. Thus handling and storing these samples must be done in dry atmospheres. In order to address this problem, moderate amounts sodium oxide (Na_2O) were added as a 'filler' in order to keep RE content low without increasing P_2O_5 content. In the first part of the research described in this dissertation, the local structure around

RE^{3+} cations in RE-doped ultraphosphate (REUP) glasses ($[O] / [P] = 2.7$–2.9) has been studied using RE L_{III}-edge (RE = Nd, Er, Dy, and Eu) and K-edge (RE = Nd, Pr, Dy, and Eu) Extended X-ray Absorption Fine Structure (EXAFS) spectroscopy. $(RE_2O_3)_x(Na_2O)_y(P_2O_5)_{1-x-y}$ glasses in the compositional range $0 \leq x \leq 0.14$ and $x + y = 0.3$ (RE = Nd, Dy, and Eu) & 0.4 (RE = Pr and Er) were studied.

The second part of this dissertation is on zirconium doped lithium silicate (ZRLS) glasses and glass-ceramics and zirconium doped lithium borate (ZRLB) glasses. Glass-ceramics consist of polycrystalline phases embedded in an amorphous phase. They are synthesized as glasses followed by a sequential heat treatment process that causes the growth of crystalline regions within the glass matrix. The crystallization process consists of two steps, nucleation and crystal growth. During the nucleation stage, very small regions of ordered structures (nuclei) form around the nucleating agents such as zirconium atoms. Further heat treatment can cause some of these nuclei to grow and become crystalline phases [8]. By controlling the base glass composition and the crystallization process, glass-ceramics having a wide range of useful properties, such as high chemical durability, high temperature stability, low negative thermal expansion, low porosity, high strength, biocompatibility, high resistivity, low dielectric constant, and superconductivity can be synthesized [1, 2]. Hence, glass-ceramics are used in a wide range of applications, such as kitchen cooktops, sensors, thermal insulators, inductors, fiber optics, biomedical implants, dental restoration, automotive fuel cells, ceramic superconductors, and large telescope mirrors.

The ZRLS glass-ceramics studied herein have a wide ranging and growing field of applications from architectural materials to mirrors for next-generation space

telescopes and inactive nuclear waste glasses [10]. In ZRLS samples, the crystallization process is initiated with internal nucleation induced by nucleating element zirconium (Zr). Compositions of both glass and crystalline phases, glass to crystalline phase fraction, the distribution pattern of the crystalline phase in the glass matrix, and local structure around Zr play key roles in determining physical, thermal, electrical, and chemical properties of these materials.

Little is known about how zirconium cations (Zr^{4+}) are incorporated into the glass structure and their different roles, such as acting as a nucleating agent and a property modifier. Zr^{4+} cations are expected to act as nucleating agents in ZRLS / ZRLB glasses of nominal composition $(ZrO_2)_x(Li_2O)_y(SiO2)_{1-x-y}$ and $(ZrO_2)_x(Li_2O)_y(B_2O_3)_{1-x-y-z}(Al_2O_3)_z$ where Li_2O, Al_2O_3, and ZrO_2 act as a property modifier [2, 8, 10]. A series of Zr-doped (3–10 mol% Zr) lithium silicate (ZRLS) glasses and glass-ceramics, a series of Zr-doped (2–6 mol%) lithium borate (ZRLB) glasses, and two reference samples (zircon $ZrSiO_4$ and monoclinic-ZrO_2) were used to study their incoordinated structure into the glass as 6-coordinated octahedral [10].

In the second part of my dissertation research, Zr K-edge EXAFS and Zr K-edge X-ray Absorption Near Edge Structure (XANES), were used to investigate the complex atomic-scale structure of these materials. Zr K-edge EXAFS spectroscopy is being used to probe the short- to intermediate-range coordination environment of Zr^{4+} cations. The effects of the ZrO_2 content, the thermal treatment (crystallization process), and the temperature during the measurement on the Zr local environment are investigated.

CHAPTER II

GLASSES AND GLASS-CERAMICS

2.1 General

A glass is an amorphous solid material with no long-range periodicity in its atomic-level structure. All glasses are amorphous, having a continuous random network of the glass formers, but not all amorphous materials are glasses. The term glass generally refers to the fusion product of inorganic materials cooled from a melt to a rigid state without crystallization [2]. Silicates are the earliest forms of glasses known to humans. Hence, early theories on glasses focused primarily on their formation. Now we know of a vast number of non-silicate glasses, such as glass formed from polymers, metals, and non-oxide inorganic compounds. In principle, any material can form a glass by cooling its liquid form below its melting point (freezing point) or by compressing the liquid [1, 2]. Currently, the emphasis of glass science is on the kinetic part, the control of glass formation, and the kinetic theory of glass formation.
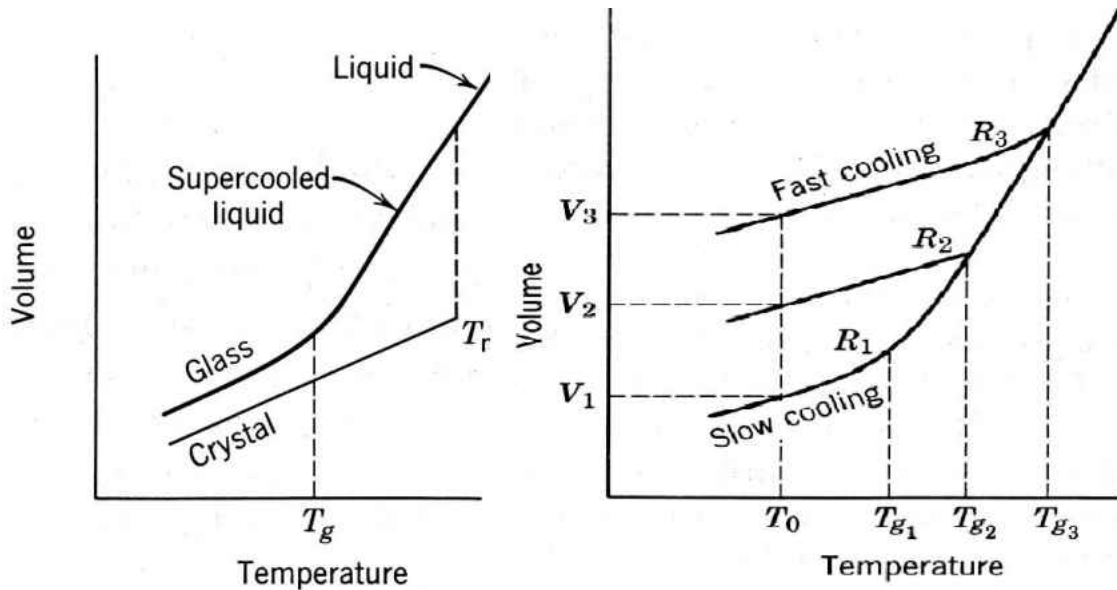
Figure 3. Typical volume versus temperature diagram for liquid, crystalline, and glassy states [11].

Glass formation by cooling can be explained by the volume versus temperature diagram shown in **Figure 3**. T_g represents the glass transition (or glass formation) temperature and T_r represents the melting temperature. When the cooling rate is slow and nuclei are present, crystallization will initiate at T_r, resulting in a sudden decrease in volume [1, 2]. When the cooling rate is sufficiently high, the volume will decrease smoothly until the glass is formed at T_g (T_g is a temperature in the temperature region between the two linear sections of the graph shown in Figure 3) and the volume vs. temperature graphs have slopes similar to that of the crystal. Also, depending on the cooling rate (slow cooling and fast cooling) within the T_g region, the volume of the glass will be slightly different at different temperatures (density change from limiting their kinetic state by T), but the slopes of the volume-temperature graphs will be similar below the transition region as shown in **Figure 3** (right) [11].

In reality, however, only a small number of compounds are capable of forming a glass without forced cooling. The good glass formers form glasses at moderate cooling

rates (not more than a few hundred C°/s) but poor glass formers require rapid or extreme cooling rates. The priors are called network formers (or self-glass formers) and are oxides such as B_2O_3, GeO_2, SiO_2, and P_2O_5. They readily form single component glasses by the conventional melt-quenching method. These oxides are p-block elements, and have strong bonds to oxygen, and also tend to favor tetrahedral structures (or triangular structures). In addition, they provide the base for other mixed oxides [1, 2].

The s-group elements, such as lithium (Li), sodium (Na), and potassium (K) in alkali-metal oxide forms (Li_2O, Na_2O, K_2O, Rb_2O, and Cs_2O) are called network modifiers [1, 2]. They show weak, non-directional bonds to oxygen, flexible geometry, and a broad distribution of bond lengths. When network modifiers are mixed with network formers, they (network modifier ions) modify the glass network because they interrupt covalent bonding, reduce network connectivity, and distort the network due to their size and strong ionic bonding [1, 2].

Dopants are small amounts of modifiers added to provide new properties. For example, adding rare-earth (RE) elements can cause a glass to luminesce and adding Zr decreases the thermal expansion coefficient of a glass.

The amount of a modifier that can be added is limited due to interactions between modifiers, such as RE-RE, Na-Na, Na-Re, Zr-Zr, Zr-Li, and Zr-Al interactions, which can lead to phase separation. There is a competition between enthalpy and entropy of the system expressed as $\Delta G_{mix} = \Delta H_{mix} - T\Delta S_{mix}$ [1]. When ΔG_{mix} is negative, the mixture become homogeneous (miscible) [1]. So, when the mixture is separated, lowering ΔG_{mix} is required.

The structure of these oxide glasses can be described by the network structural rules of Zachariasen and Smekal's mixed bonding hypothesis [1, 2]. Zachariasen's random networking theory (1932) states that the formation of an oxide glass may occur when (1) no oxygen may be linked to more than two cations, (2) the number of oxygen atoms surrounding a cation must be small (around 3–4), (3) the oxygen polyhedral share corners with each other, not edges of faces, and (4) at least three corners of each polyhedron must be shared (network can be 3D only if at least three corners of oxygen polyhedron are shared) [1, 2].

There are several exceptions to the above rules. For (1), even though the cation coordination number (CN) of oxygen is two in most oxide glasses, in some cases, such as binary Ti_2O - B_2O_3 glasses, this number can be three. For (2), the oxygen CN of the cation for silica and phosphate oxides are four while that for borate oxides is three to four and for tellurium (Te) oxides it can be as high as six in some cases. For (3), and (4), Hagg pointed out that an infinite 3D network may not be a necessary condition for glass formation [1]. Also, Smekal proposed that glasses are only formed from melts which contain intermediate bonds between those that are purely covalent bonds and those that are purely ionic bonds [1, 2]. Purely covalent bonds prevent the formation of a non-periodic network while purely ionic bonds lack any directional characteristics. Thus for glass formation, a mixture of chemical bonds in a material is necessary. These widely accepted descriptions will be used to describe the effects of dopants (RE and Zr) in oxide glasses.

The role of oxygens can be explained using the Q^i terminology, see **Figure 5**. In general, there are three different classifications for oxygens in a phosphate glass. The

bridging oxygens (BOs) are oxygens connecting two tetrahedra via a $-P-O-P-$ link. Double-bonded oxygens taking part in $-P=O$ bonds are called terminal oxygens (TOs). A non-bridging oxygens (NBO) is bonded to a phosphorus on one side and to a modifier cation such as Li, Na, Al, RE, Zr, etc. on the other side. They break $-P-O-P-$ links and $-P=O$ bonds to create $-P-O-$ cation $-$ links. The Q^i terminology was first introduced by Liebau to describe structure and bonding in crystals, where 'i' is the number of BOs per tetrahedron [13]. The relative concentration of the various Q^i units depends on the composition of a glass.

2.2 Rare-Earth Doped Sodium Phosphate Glasses

The structure of phosphate glasses is based on $(PO_4)^{3-}$ phosphate tetrahedral building blocks linked to each other via BOs, as shown in **Figure 4**. Three of the four oxygens of a tetrahedron are connected to three other tetrahedra via $-P-O-P-$ links and the fourth one is double-bonded (TO) to the central phosphorus atom. When network modifiers, such as Na_2O and RE_2O_3 are added, the cations (C) will cause breaking of the phosphate glass network by creating more NBOs ($-P-O-C-$ link).
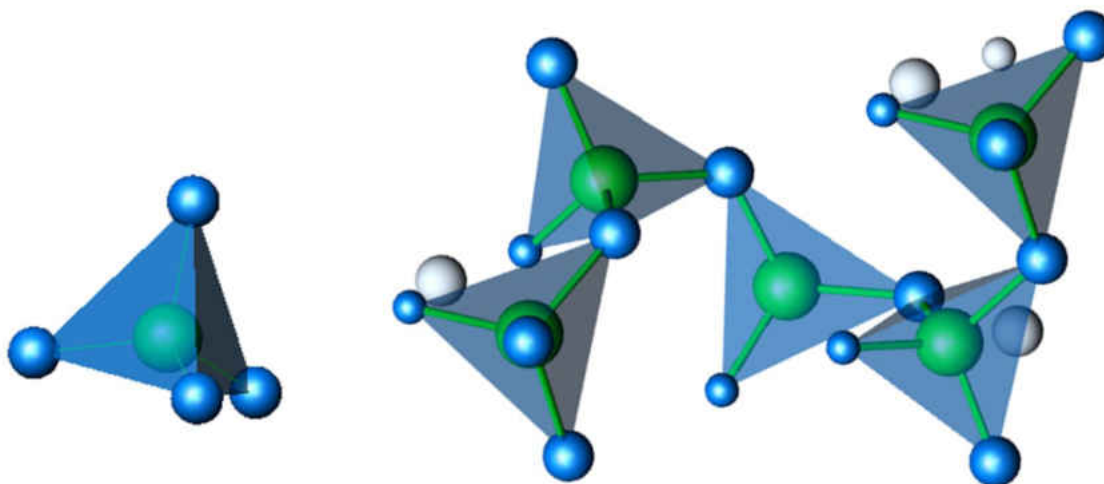
Figure 4. Basic PO_4^{3-} unit (left), -P-O-P- network of the P_2O_5 glass (right). The blue spheres are oxygen atoms and at the center of each tetrahedron is a phosphorus atom (green).

Phosphate glasses are divided into five main categories based on their [O] / [P] ratio as shown in **Table 1**. Glasses with [O] / [P] = 2.5–3.0 are 'ultraphosphates' and the primary network is a cross linked network of Q^2 and Q^3 tetrahedra. Those for which [O] / [P] = 3 are known as 'metaphosphates' and the primary network is composed of chains or rings of Q^2. Glasses for which [O] / [P] = 3.0–3.5 are known as 'polyphosphates' and the primary network is composed of chains of Q^2 ending in Q^1 dimers. 'Pyrophosphates' have a [O] / [P] ratio of 3.5. Finally, at [O] / [P] > 3.5, the structure is dominated by Q^1 dimers and isolated Q^0 and these glasses are called 'orthophosphates.' This nomenclature is summarized in **Table 1** [3, 12]. The atomic-scale structure of phosphate glasses described by the Q^i terminology is shown in **Figure 5**.

Table 1. Five main categories of phosphate glasses by [O] / [P] ratio.

Phosphate type	$\frac{[O]}{[P]}$ ratio	Q^i	Primary network
Ultraphosphates	$2.5 < \frac{[O]}{[P]} < 3$	Q^2 and Q^3	Cross linked network of Q^2 and Q^3
Metaphosphates	$\frac{[O]}{[P]} = 3$	Q^2	Chains or rings of Q^2
Polyphosphates	$3 < \frac{[O]}{[P]} < 3.5$	Q^1 and Q^2	Chains of Q^2 ending in Q^1
Pyrophosphates	$\frac{[O]}{[P]} = 3.5$	Q^1	Q^1 dimers
Orthophosphates	$3.5 < \frac{[O]}{[P]}$	Q^1 and Q^0	Isolated Q^0 and Q^1
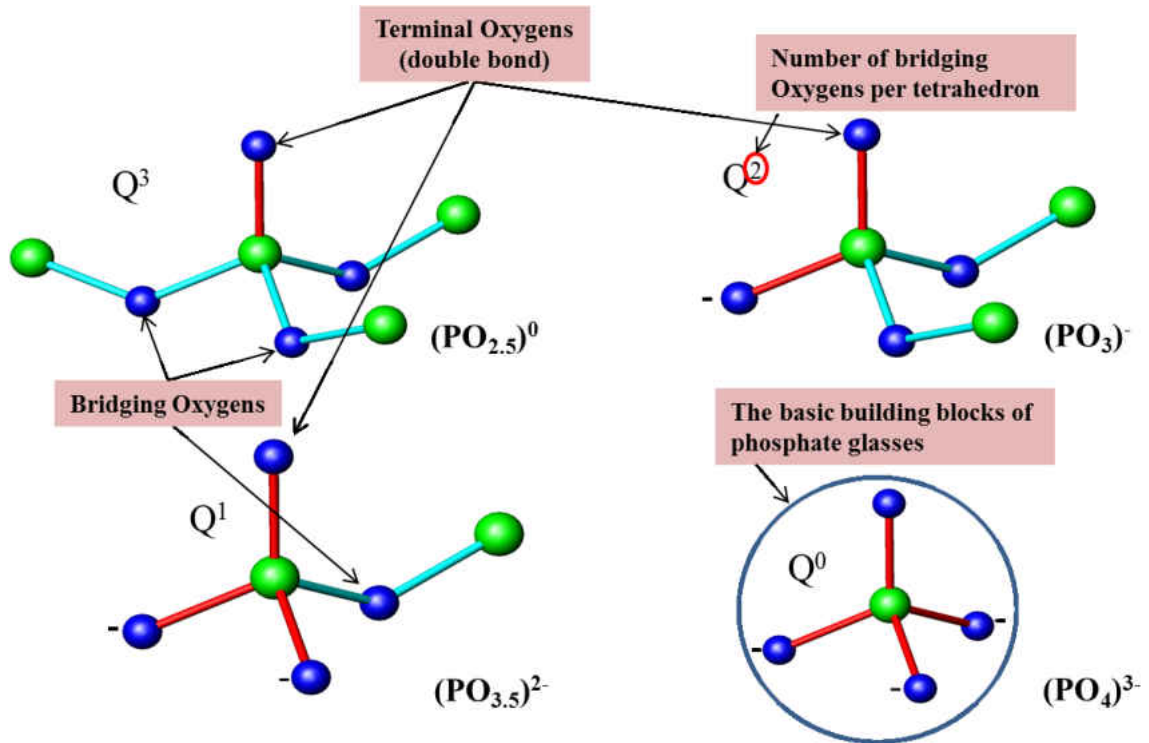
Figure 5. Phosphate units observed in phosphate glasses [15]. Green spheres are silicon atoms and blue spheres are oxygen atoms.

Even though one would think that increasing RE content may lead to an increase in lasing efficiency, previous researches have shown that the distance between RE^{3+} cations and the coordination enviroment around RE^{3+} cations play critical and complex roles in determining the lasing characteristics of these glasses [12, 14]. Non-radiating energy losses due to RE^{3+}-RE^{3+} interactions can be significant and adversely affect laser gain when the distances between RE^{3+} ions are relatively short [12]. Hence, RE phosphate glasses classified as ultraphosphates and metaphosphates have been observed to have better lasing properties than phosphate glasses with higher RE contents [7, 12, 14]. **Figure 6** shows the energy levels and laser transitions of RE^{3+} cations studied in this research.
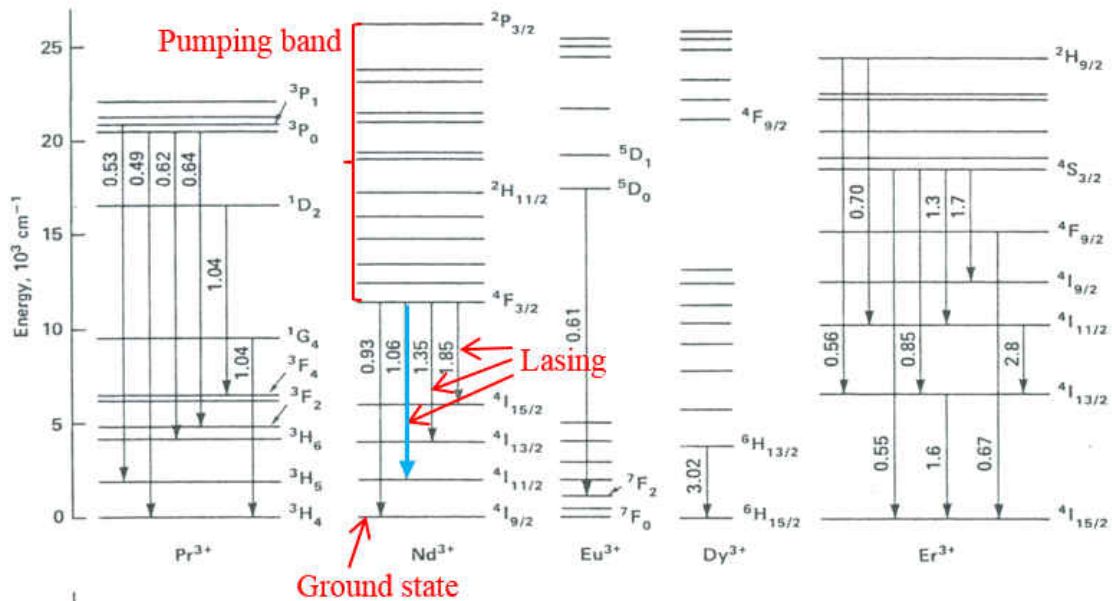
Figure 6. Radiative transitions of the five rare-earth ions studied. Wavelengths of transitions are in μm [6]. Typical four-level laser scheme is indicated for Nd^{3+} ion.

At low RE concentrations, binary RE-doped phosphate (REP) glasses can be highly hygroscopic because of their relatively large P_2O_5 content. The amounts of P_2O_5 and RE_2O_3 in the samples investigated were kept below 70 mol% and 15 mol%, respectively, by using

Na$_2$O as a filler modifier. This allowed us to keep the [O] / [P] ratio in the metaphosphate region while keeping the rare-earth content below 15 mol%.

The first part of this research is focused on obtaining short- to intermediate-range structural information for above mentioned rare-earth sodium phosphate glasses using the EXAFS techniques. Using this information, we will try to find the concentration of RE modifiers, and processing conditions and techniques, to determine how these factors affect their lasing properties and especially on how to minimize non-radiating energy losses, such as concentration quenching and multiphonon absorption.

2.3 Zirconium-Doped Lithium Silicate Glass-ceramics

(SiO$_4$)$^{4-}$ tetrahedron is the basic building block of silicate glasses. In pure SiO$_2$ glass, each oxygen at the four corners of a tetrahedron is shared by another tetrahedron to form a continuous 3-dimensional network. Such tetrahedra, which contain four BOs are designated as Q^4 units, as shown in **Figure 7**. Disorder is due to connecting angle between tetrahedra Si – O – Si links [1, 2]. The structure of silicate glasses is well described by the network structural rules of Zachariasen [1, 2]. The addition of any alkali oxide, such as Li$_2$O forming a binary glass will reduce the viscosity of the melt and decrease the connectivity of the melt by increasing NBOs.
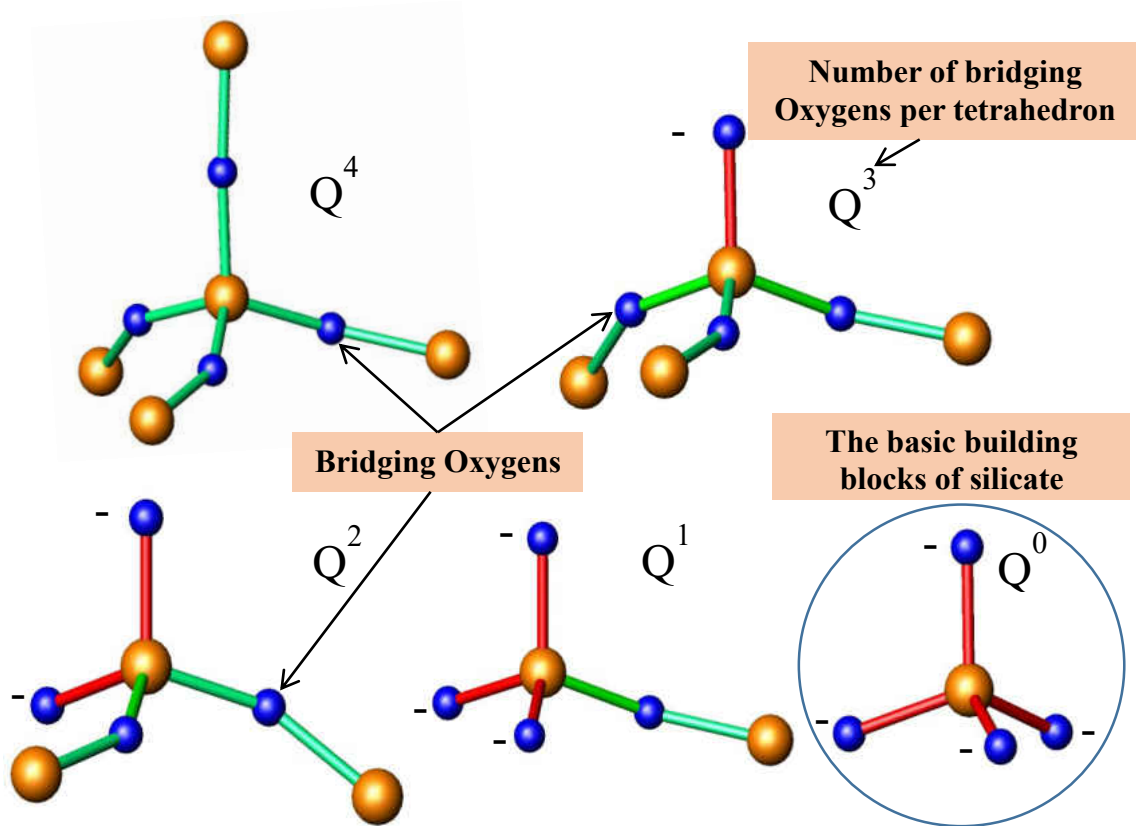
Figure 7. Silicate units observed in silicate glasses. Orange spheres are silicon atoms and blue spheres are oxygen atoms.

Table 2. Different categories of silicate glasses by [O]/[Si] ratio [11].

Silicate type	$\dfrac{[O]}{[Si]}$ ratio	Q^i	Primary network
Network	$\dfrac{[O]}{[Si]} = 2$	Q^4	Q^4 fully linked network (4 BOs, no NBOs)
Region of interest	$2 < \dfrac{[O]}{[Si]} < 2.5$	Q^3 and Q^4	Q^3 and Q^4
Phyllosilicates (Sheets)	$\dfrac{[O]}{[Si]} = 2.5$	Q^3	Q^3
Network and chains or rings	$2.5 < \dfrac{[O]}{[Si]} < 3$	Q^2 and Q^3	Network and chains or rings of Q^2 and Q^3
Metasilicates (Inosilicates, chains and Cyclosilicates, rings)	$\dfrac{[O]}{[Si]} = 3$	Q^2	Q^2
Chains, rings, and Pyrosilicates ions.	$3 < \dfrac{[O]}{[Si]} < 3.5$	Q^1 and Q^2	Chains and rings of Q^1 and Q^0
Pyrosilicates (Sorosilicates)	$\dfrac{[O]}{[Si]} = 3.5$	Q^1	Q^1
Pyrosilicates ions and Orthosilicates ions.	$3.5 < \dfrac{[O]}{[Si]} < 4$	Q^0 and Q^1	Q^1 and Q^0
Orthosilicates (Nesosilicates)	$\dfrac{[O]}{[Si]} = 4$	Q^0	Q^0

Silicate glasses are classified by their oxygen/silicate ([O] / [Si]) ratio. They are divided into four main categories (phyllosilicates, metasilicates, pyrosilicates, and orthosilicates) by [O] / [Si] ratio as shown in **Table 2**. Alkali oxides break Q^4 network and increase NBOs. Alkali ions occupy spaces between tetrahedra reducing the unoccupied free volume of the structure. Due to the increase of NBOs, alkali oxides greatly decrease the viscosity of the melt, and the glass transition temperature (about 500 K), and increase density, refractive indices, and electrical conductivity [1].

The alkali silicate glasses in this study contain 26.7–30 mol% of lithium oxide (Li_2O). Introduction of Li_2O tends to increase the conductivity by several orders of

magnitude, decrease the glass transition temperature, and increase the thermal expansion coefficient [1, 2].

2.3.1 Glass-ceramics

Glass-ceramics are a mix of disordered and polycrystalline phases of ultra-fine grain size formed by controlled crystallization of glasses through regulated heat treatments. They exhibit both properties of glasses and ceramics depending on the degree of crystallinity (up to 99.9% crystallinity) [1, 8]. They show superior strength when compared to glass, can have zero porosity (measure of void), and contain more than one phase enabling adjustment of their properties by changing relative phase amounts [1]. Some of the preferred properties for the commercial uses are, high mechanical strength, low thermal expansion coefficient, good chemical durability, and tunable electrical conductivity [1].

The basic glass-ceramics formation process requires two processes: *nucleation and crystal growth* [1]. When glasses are first formed they are heated at the nucleation temperature at a well-characterized rate [1]. During this nucleation stage, presence of nucleating agents, such as zirconates (Zr in our case), metals, fluorides and other species are required to initiate the process. Nucleation may be either homogeneous (classical nucleation theory) or heterogeneous (diverse in content, nucleus created with the influence of foreign particles). The homogeneous nucleation is based on the classical nucleation theory assuming nuclei are formed with equal probability and they form extremely small crystalline phases at their sites but too small to be detected. Then glasses are reheated at higher temperature for growth of crystal phases, as shown in **Figure 8**.

They are heated until the desired degree of crystallinity is reached. In zirconium-doped lithium silicate glasses we investigated, Zr^{4+} cations are expected to act as the nucleating agent.

Metastable Zone of Undercooling

Growth Nucleation

Rate
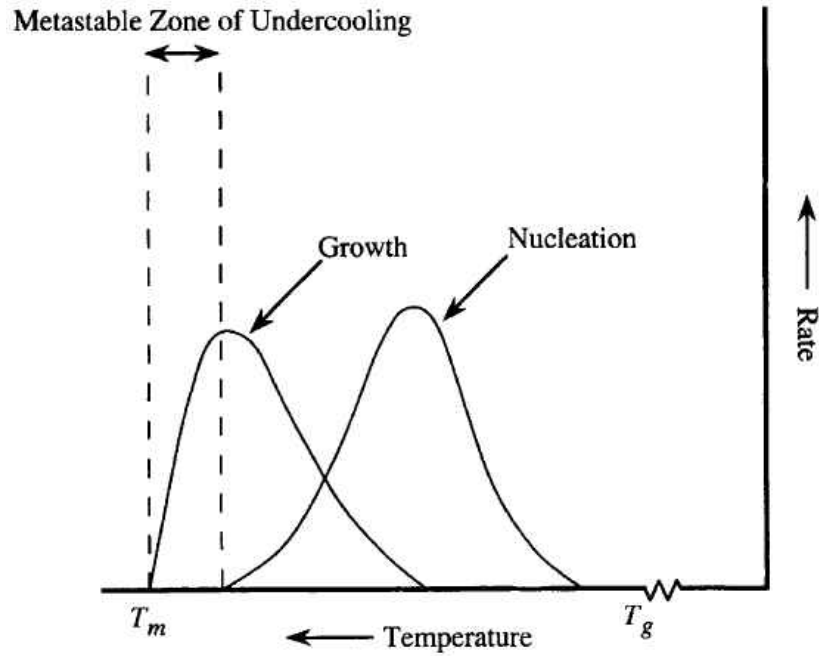
T_m Temperature T_g

Figure 8. Effects of temperature on rates of nucleation and crystal growth for a glass forming melt [1]. T_g is the glass transition temperature and T_m is the melting point temperature.

When the viscosity of the melt is low, nucleation rate is large due to kinetic obstruction reduction, and the growth rate is high. When temperature increases around T_m, the viscosity increases rapidly slowing nucleation and crystal growth.

2.4 Zirconium-Doped Lithium Borate Glasses

The structural model for borate glasses is significantly different from silicate glasses. Crystalline borate oxides show triangular (3-fold) or tetrahedral (4-fold) structure. The building block for borate glasses, however, is $(BO_3)^{3-}$. The borate glass

structure is composed of boroxol rings or boroxol groups, as shown in **Figure 9**. All three corners of each oxygen are connected to another boron to form a complete planar network instead of 3-dimensional network. By crumpling, the planar network forms a 3-dimensional network but bonds in 3-dimension are weak, and the structure is easily disrupted due to a large concentration of an intermediate unit such as a tetraborate unit (one triangle from a boroxol ring having been converted to a tetrahedron) from addition of alkali oxide [1, 11]. Addition of more alkali oxide (< 25 mol%) eventually induces more diborate groups (two tetrahedral per three-membered ring) to be formed from tetraborate groups and the complete disappearance of boroxol rings [1].
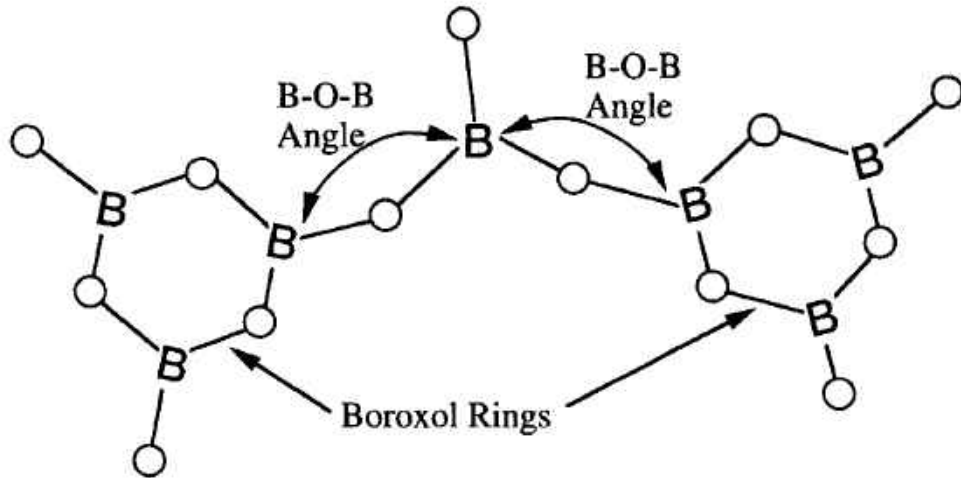
Figure 9. Boroxol ring structures in borate glasses and alkali borate glasses [1].

Borate glasses with alkali oxides show different characteristics compared to silicate glasses with alkali oxides. The transition temperature increases and the thermal expansion coefficient decreases with the additions of small amounts of alkali oxide such as lithium, sodium, and potassium. Also, introducing alkali oxides will change the 3-fold structure to 4-fold structure with no NBO formation. Additions of more than 25 mol% of

alkali oxide, eventually cause the formation of NBOs and the disruption of the structure (diborate groups) [1, 2]. In this study, the amount of lithium oxides (Li_2O) were kept between 14.5–20.9 mol%, indicating a large concentration of boroxol ring structures in our borate glass samples, as shown in **Figure 9**.

CHAPTER III

EXPERIMENTAL METHODS

3.1 X-ray Absorption Spectroscopy (XAS)

When X-rays pass through matter they interact with electrons. There are several types of interactions, such as absorption, elastic scattering, and inelastic scattering [16]. For EXAFS, we focus on X-ray absorption. The acronym "XAS" is a broad one describing any experiment involving absorbed photons. XAS data are collected by tuning the energy of X-rays using a crystalline monochromator around a range where core electrons can be excited. It measures the absorption coefficient μ versus the photon energy $E = hv$. When plotted, μ decreases smoothly with increasing photon energy except at certain energies known as absorption edges. The principal quantum numbers n = 1, 2, and 3, correspond to the K-, L-, and M-edges, respectively [16, 17, 18].

Absorption edges were first measured by Maurice De Broglie in 1913. Then in 1920, M. Siegbahn observed "fine structure", which is energy dependent variations (EXAFS oscillations) in absorption coefficient $\mu(E)$ [17, 18]. Then for another 50 years, theoretical work was still obscure until Stern, Sayers and Lytle resolved the confusion between long-range order model and short-range model in 1971 [19, 20, 21]. They explored and theorized X-ray Absorption Fine Structure (XAFS) by providing satisfactory description of the physical process. They used Fourier methods to show that XAFS is a practical tool for structural determination and that the local geometry of samples can be characterized for a wide range of materials using this technique. After

that, the use of synchrotron radiation facilities such Stanford Synchrotron Radiation Laboratory, which started in 1974, allowed a rapid development of connecting theory and experiment. X-rays from synchrotron sources improved speed and accuracy of data collection and allowed rapid progress in XAFS techniques.
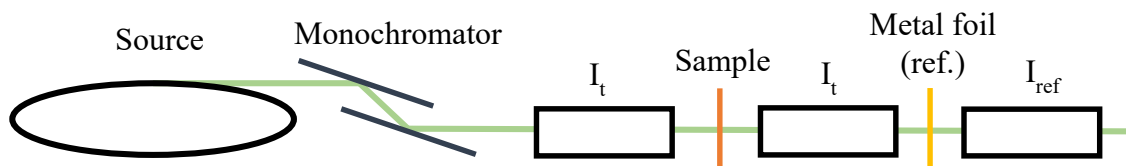
Figure 10. Transmission mode XAFS experiment using the synchrotron source.

Intense and tunable X-rays are required for the XAS spectroscopy. For this reason, synchrotron radiation sources are the preferred choice for XAS experiments. X-rays with a narrow band width of 1 eV or less are produced by tuning crystalline monochromators, as shown in **Figure 10**. Such a narrow band width is required to resolve XANES features around the main absorption edge. [16].

3.2 X-ray Absorption Fine Structure (XAFS)

XAFS spectroscopy is a unique tool to investigate the local structure around selected elements at atomic and molecular scale. XAFS spectra represent the probability of photon absorption as a function of energy. The absorption coefficient $\mu(E)$ is measured while changing the energy of the incident X-rays. XAFS shows how X-rays are absorbed by a selected element near and above the core-binding energies of that atom showing the modulation of an atom's X-ray absorption probability due to the chemical

and physical state of the atom [16–22]. XAFS can be applied to crystals, amorphous materials, glasses, quasicrystals, and so on [16, 17, 18]. Thus XAFS is used in materials science, synthetic chemistry, structural biology, environmental science, etc. XAFS does not provide complete answers to the physical and chemical structure of the investigated materials [16, 18]. It is a scientific tool that requires knowledge and proper judgement to yield correct answers.

XAFS includes XANES (X-ray Absorption Near Edge Structure), NEXAFS (Near-Edge X-ray Absorption Fine Structure), SEXAFS (Surface Extended X-ray Absorption Fine Structure), and EXAFS (Extended X-ray Absorption Fine Structure). The basic physics is fundamentally the same but they have different approximations, techniques, terminology, and theoretical approaches [18].

XANES is the region typically within 30–50 eV of the edge energy E_0 (sharp rise in X-ray absorption spectrum). NEXAFS is a synonym for XANES and generally only used for low-energy edges below 1000 eV (low-Z elements). EXAFS is the oscillations above the XANES region typically 30–50 eV above the edge. SEXAFS is the EXAFS performed at a glancing angle so the region near the surface of the sample is probed. Of all XAFS related techniques, EXAFS is the primary interest in this work.

XAFS can be measured in fluorescence mode, electron yield mode, and transmission mode. Fluorescence mode measures the incident intensity and the fluorescence intensity emitted after the X-ray absorption event due to the core-hole relaxation. Electron yield mode measures ejected electrons as the core-hole is filled. Transmission mode simply measures X-ray intensity before and after the beam is passed

through a uniform sample with certain thickness x, as shown in **Figure 10** and **Figure 11**.

The relationship between I_0 and I_t is expressed as Eq. (3.2.1).
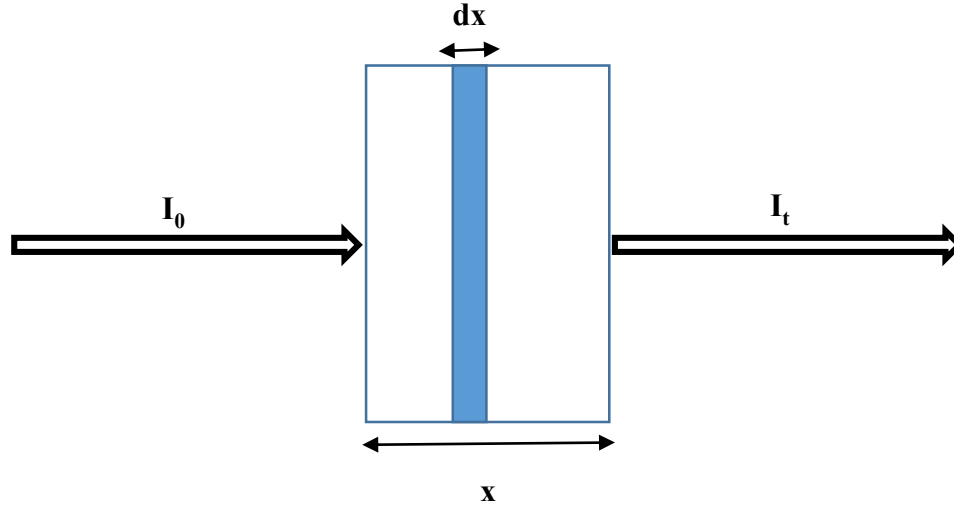
Figure 11. An incident beam of monochromatic X-rays of intensity I_0 passes through a sample of thickness x, and transmitted intensity I_t for the transmission mode XAS.

$$I_t = I_0 e^{-\mu(E)x}$$
(3.2.1)

In transmission mode, the X-ray absorption coefficient $\mu(E)x$ (proportional to the X-ray absorption probability) is measured. The measured energy dependence of the absorption coefficient $\mu(E)$ of a sample of thickness x, is expressed as Eq. (3.2.2).

$$\mu(E)x = \ln\frac{I_o}{I_t}$$
(3.2.2)

An XAFS measurement is a measure of the energy dependence of the X-ray absorption coefficient $\mu(E)x$, near and above the binding energy of a known core level of a known atomic species [22]. After an absorption event, one of the core electrons is ejected as the photoelectron wave leaving a core-hole. The excited state of the atom (after the absorption event) decays within a few femtoseconds of the absorption [22].

XAFS phenomena are due to the wave nature of the photoelectron. The ejected photoelectron wave can scatter from the neighboring atom of the absorbing atom and the scattered photoelectron waves return to the absorbing atom. The backscattered waves will alter the absorption coefficient $\mu(E)$ since the absorption coefficient $\mu(E)$ depends on whether there is an available electronic state (an electron at the location of the atom with appropriate energy and momentum) [18, 20, 22]. As the energy of a photoelectron is changed, its wavelength and phase will vary. The distance between the absorbing atom and the backscattering atom, and the type of surrounding atom determine the phase and strength of the backscattered wave.

The XAFS spectrum symbolized as $\chi(E)$ represents the fractional change in absorption coefficient $\mu(E)$ due to neighboring atoms as

$$\chi(E) = \frac{\mu(E) - \mu_0(E)}{\Delta\mu_0(E_0)} \qquad (3.2.3)$$

where $\mu_0(E)$ is estimated smooth spline background function, representing the absorption of an isolated atom (absorption coefficient of the absorber atom assuming no neighboring atoms) and $\Delta\mu_0(E_0)$ is the estimate of the edge step (a normalization factor that arise from the net increase in the total atomic background absorption at the edge).

3.2.1 Extended X-ray Absorption Fine Structure (EXAFS) spectroscopy

EXAFS is the fine structure in X-ray absorption coefficient, starting from around 30–50 eV above the absorption edge up to 1000 eV or further depending on the absorption edge type (K-edge, L_{III}-edge, etc.), as shown in **Figure 12**. Region near the

absorption edge is XANES where interaction between ejected photoelectron and potential of the surrounding atom is too strong for EXAFS analysis.
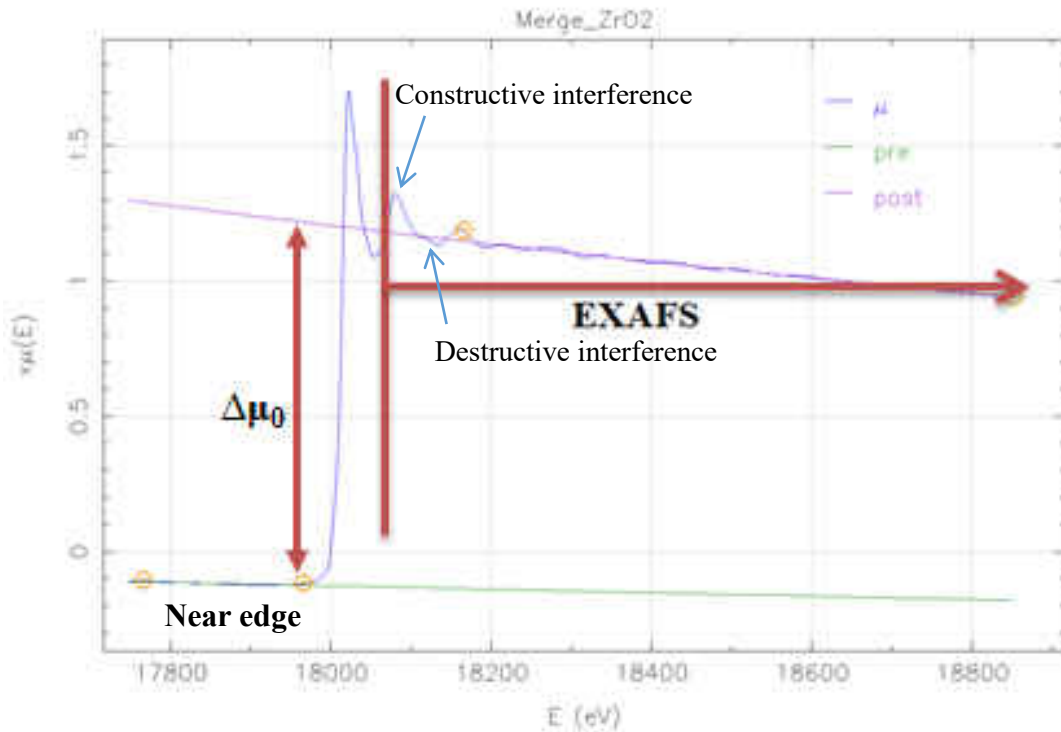
Figure 12. K-edge XAFS $\mu(E)$ for monoclinic-ZrO$_2$. EXAFS region starting approximately at about 30–50 eV above the edge.

The main useful (positive) properties related with EXAFS are [18]:

1. No requirement for long-range order. Amorphous and crystalline solids can be treated on the same basis. The major application of EXAFS is to determine the structure of disordered materials.

2. Local atomic arrangement can be determined for neighboring atoms of the same type separately with higher resolution than conventional scattering techniques.

3. The measurement process is quick and relatively easy.

Some disadvantages are

1. EXAFS is short-range order probe, so long-range order information is limited. It is a complementary tool to diffraction.

2. When RMS disorder is greater than about 0.3 Å, structural information is limited.

3. Data analysis is tedious and complicated.

3.3 Basics of EXAFS Theory

EXAFS can be observed when atoms are in a condensed state. When an X-ray photon has energy comparable to an absorption edge of an atom, it will eject a bound electron corresponding to that edge. K- and L-edges are the most commonly used edges for EXAFS [16, 18].

The ejected photoelectron is treated as a spherical wave radiating outward with a wavelength $\lambda = h / p$ given by de Broglie relation where p is the momentum of the photoelectron and h is the Planck's constant.

XAFS is a quantum mechanical phenomenon based on the X-ray Photoelectric effect. The absorption of the X-ray is quantum mechanically explained by a matrix element between initial and final states of the absorbing atom. Modification of the photoelectron by surrounding atoms at the center of the absorbing atom determines EXAFS. Backscattered waves will interfere with the outgoing wave at the center depending on their relative phase. Interference between the outgoing wave and the backscattered wave from surrounding atoms will change the probability of the absorption of an X-ray. These quantum interference effects cause an energy-dependent variation in the X-ray absorption probability of the absorber atom. The absorption is enhanced if it

leads to constructive interference at the location of the absorbing atom and reduced when destructive interference occurs.

In the rest of this section, we outline the derivation of the EXAFS equation that we use in this research, building it up factor by factor. We start by thinking about a plane wave instead of treating as a spherical wave bouncing off a soft boundary with no change in phase [18].

$$2R = n\lambda \tag{3.3.1}$$

For constructive interference, Eq. (3.3.1) needs to be satisfied where R is the distance between the absorber and the scatterer. The XAFS spectrum $\chi(E)$ is proportional to the interference pattern given as,

$$\chi(E) \propto Cos(2\pi \frac{2R}{\lambda}) \tag{3.3.2}$$

In EXAFS, XAFS function χ is analyzed in k-space and R-space. Thus $\chi(E)$ needs to be converted to $\chi(k)$. From basic physics, momentum p of the photoelectron is related to its kinetic energy $T = E - E_0$ as

$$\frac{p^2}{2m} = h\nu - E_0 = E - E_0 \tag{3.3.3}$$

where m is the mass of an electron and E_0 is the edge energy. The kinetic energy of the ejected photoelectron equals the absorbed photon's energy minus the electron's binding energy in the atom. When the ejected photoelectron's energy is greater than 15 eV ($E - E_0 > 15$ eV) then it is greater than the interaction energy with the surrounding atoms by about 3 eV, interaction with the surrounding atom can be treated as a perturbation about an isolated atom [17, 18]. Using Eq. (3.3.3), the momentum p can be expressed as

$$p = \sqrt{2m(hv - E_0)} \qquad (3.3.4)$$

Then combining Eq. (3.3.3), Eq. (3.3.4) and $p = \hbar k$ yields

$$k = \sqrt{\frac{2m(hv - E_0)}{\hbar^2}} = \frac{1}{\hbar}\sqrt{2m(E - E_0)} \qquad (3.3.5)$$

Using Eq. (3.3.5), we can represent χ with respect to the photoelectron momentum index k.

Because the wave number k is defined by $k = \frac{2\pi}{\lambda}$, Eq. (3.3.2) can be rewritten as

$$\chi(k) \propto Cos(2kR) \qquad (3.3.5)$$

From Eq. (3.3.5), the plane wave scattering amplitude $f(k)$ is applied which describes the element dependent nature. Thus $\chi(k)$ provide types of atoms nearby and distance from absorber atom given by,

$$\chi(k) = f(k)\,Cos(2kR) \qquad (3.3.6)$$

When we consider multiple neighbors, then the scattering events contribute separately, thus modulating the absorption probabilities given by,

$$\chi(k) = \sum_i f_i(k)\,Cos(2kR_i) \qquad (3.3.7)$$

Also, we consider degeneracy N_i by the same species at the same average distance. Then N_i will be multiplied to Eq. (3.3.7).

$$\chi(k) = \sum_i N_i\,f_i(k)\,Cos(2kR_i) \qquad (3.3.8)$$

Now instead of assuming soft boundary around the nearby atoms, we have to introduce phase-shifts due to varying potentials of the center atom and the backscattering atom. Then the above expression becomes,

$$\chi(k) = \sum_i N_i \, f_i(k) \, Sin(2kR_i + \delta_i(k)) \qquad (3.3.9)$$

where $\delta_i(k)$ is the effective scattering phase-shift.

Now instead of assuming a plane wave, the spherical wave expression with scattering probability reduction factor proportional to $\frac{1}{R^2}$ is applied. The new expression with spherical wave effects accounted for is,

$$\chi(k) = \sum_i N_i \, \frac{F_i(k)}{k \, R_i^2} Sin(2kR_i + \delta_i(k)) \qquad (3.3.10)$$

Here $F_i(k)$ is redefined from previous expression $f_i(k)$ and is called the effective scattering amplitude.

The final state of the absorbing atom is different from the initial state due to a core-hole. More positive charge from the nucleus and orbitals adjusted to this change will result as incomplete overlap. The effect due to the difference in potential around the absorber atom is modeled by an element-dependent constant, the amplitude reduction factor S_0^2 [17, 18]:

$$\chi(k) = S_0^2 \sum_i N_i \, \frac{F_i(k)}{k \, R_i^2} Sin(2kR_i + \delta_i(k)) \qquad (3.3.11)$$

S_0^2 is typically between from 0.7 to 1 and the chemical environment is not important for S_0^2. It is due to the many-body relaxation effect, dynamically varying potential due to relaxation effects interfering with the ejected electron, which is one of

the many-body effects. The many-body effects are due to rearrangement of electrons in the absorbing atom and in surrounding environment (passive electrons) due to core-hole excitation and electron-electron correlation between initial state and final state of the active electron [17, 18]. They are mostly related with electrons interacting with one another through Coulomb potential depending on instantaneous positions of other electrons [16, 17, 18].

The other many-body effects are due to electron-electron scattering related with the mean free path $\lambda(k)$. Its contribution has a strong R_i dependence because instead of being scattered elastically, the photoelectron might scatter inelastically by exciting a valence electron from nearby atoms or a phonon in the crystal. The energy of the photoelectron will be lost and it will change the wavelength and the interference condition. Also, when R_i increases, the probability of inelastic effects, such as inelastic scattering of the photoelectron (extrinsic events) and the creation of the core-hole (intrinsic events), will increase than the probability of elastic scattering effects [16, 18]. In addition, the final state of the absorber atom depends on decay of the core-hole. The fluorescence due to an electron in a higher orbital falling into the core-hole or ejection of another electron (Auger electron) will change the final state of the absorber atom [16, 17]. Thus contributions from the suppression due to inelastic scattering and the core-hole decay, can be applied together as [16]

$$\chi(k) = S_0^2 \sum_i N_i \frac{F_i(k)}{k\, R_i^2} Sin(2kR_i + \delta_i(k))\, e^{-\frac{2R_i}{\lambda(k)}} \qquad (3.3.12)$$

The Eq. (3.3.13) is for a single photon absorbed by a single atom. Since EXAFS is an average in a real material, surrounding environment may differ due to different

crystallographic environments (more than one phase around the absorbing atom), local

differences due to defects (random scatter), static disorder (amorphous material), gradient

within a material (composition change within a material), and vibrations between the

absorber and the scatterer (thermal vibration results in thermal disorder) [16, 18]. The

EXAFS equation is modified with an additional factor of the mean square radial

displacement (or XAFS Debye-Waller factor) σ_i^2. The standard, simplified EXAFS

equation is given by

$$\chi(k) = \sum_i S_i^2(k) \frac{N_i}{kR_i^2} F_i(k) \sin(2kR_i + \delta_i(k)) e^{-\frac{2R_i}{\lambda(k)}} e^{-2\sigma_i^2 k^2} \qquad (3.3.13)$$

The above Eq. (3.3.13) is the equation recommended by IUCR (International

Union of Crystallography, 2011) and we will treat it as the standard EXAFS equation for

this research.

3.4 Sample Preparation

Rare-earth sodium phosphate glasses listed in Table 3 were prepared by melting

stoichiometric amounts of RE_2O_3, P_2O_4, and $NaHCO_3$ powders in an open alumina

crucible at 1300 °C for about an hour and then quenching in air using steel molds. Melts

were homogenized by stirring during melting. Silica or alumina contamination may be

possible from the alumina crucibles used during the melting process. Quenched samples

were annealed at 200–450 °C for about two hours. X-ray diffraction was used to confirm

that glass samples were free of crystalline components. **Figure 13** shows a ternary plot

(top) of investigated RE samples based on batched compositions for all RE samples and

the analyzed composition for Nd, Dy, and Er samples from Elemental Analysis Inc. using

Photon Induced X-ray Emission (PIXE).

Table 3. Batched and analyzed compositions of the investigated REUP glass. The analyzed composition is from Elemental Analysis Inc. using Photon Induced X-ray Emission (PIXE).

Sample	RE	RE_2O_3 (Batched) x	Na_2O (Batched) y	RE_2O_3 (analyzed) x	Na_2O (analyzed) y	O / P Ratio
Pr07	Pr	0.005	0.395			2.84
Pr08	Pr	0.010	0.390			2.85
Pr10	Pr	0.030	0.370			2.88
Pr12	Pr	0.050	0.350			2.92
Er13	Er	0.005	0.395			2.84
Er14	Er	0.010	0.390			2.85
Er18	Er	0.050	0.350			2.92
Nd19	Nd	0.054	0.236	0.047	0.337	2.78
Nd20	Nd	0.099	0.198	0.083	0.328	2.85
Nd21	Nd	0.138	0.158	0.127	0.257	2.91
Dy22	Dy	0.053	0.247	0.046	0.383	2.79
Dy23	Dy	0.090	0.200	0.076	0.357	2.83
Dy24	Dy	0.138	0.164	0.121	0.310	2.91
Eu25	Eu	0.053	0.237	0.052	0.369	2.78
Eu26	Eu	0.090	0.213	0.083	0.328	2.85
Eu27	Eu	0.137	0.155	0.127	0.257	2.90
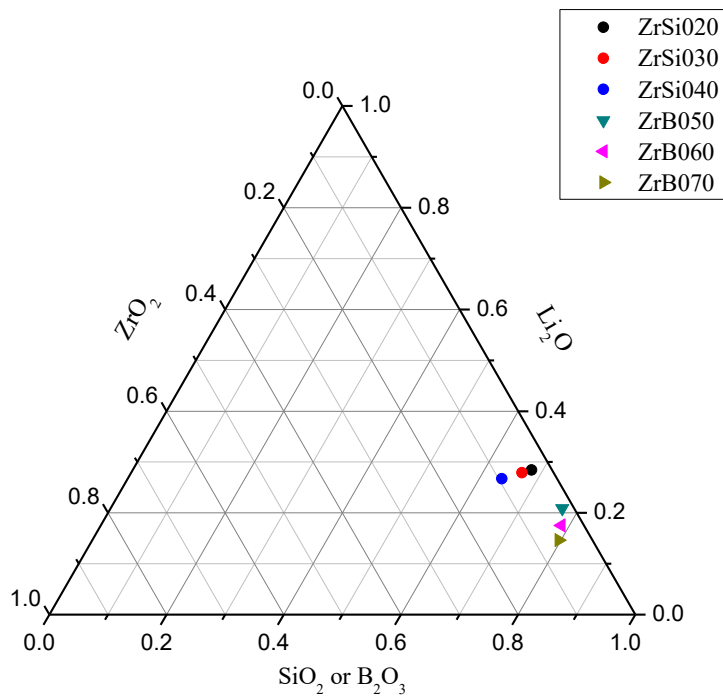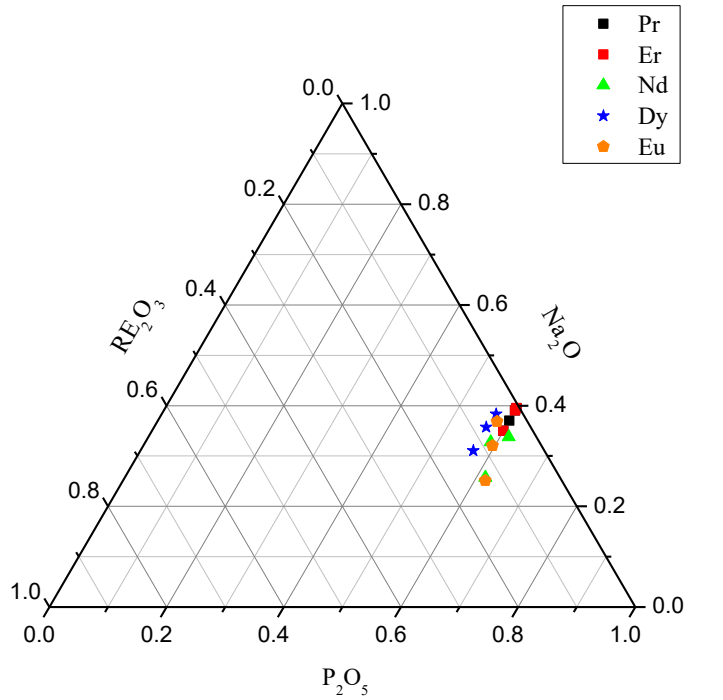
Figure 13. Ternary plot representing the composition of investigated rare-earth doped ultraphosphate glasses (top). Ternary plot representing the composition of investigated Zr-doped lithium silicate glasses / glass-ceramics and Zr-doped lithium borate glasses (bottom).

Table 4. Compositions and thermal treatments applied for Zr-doped lithium silicate glasses / glass-ceramics and Zr-doped lithium borate glasses.

Sample ID	ZrO_2 p	Li_2O q	Al_2O_3 r	SiO_2 s	B_2O_3 1-p-q-r-s
ZrSi010	0	0.295	0	0.705	0
ZrSi020	0.035	0.284	0	0.681	0
ZrSi021	After nucleation (ZrSi020 annealed at 520 °C/10min)				
ZrSi022	After nucleation (ZrSi020 annealed at 520 °C/10min) & crystallization (annealed at 720 °C/20min)				
ZrSi030	0.054	0.279	0	0.668	0
ZrSi031	After nucleation (ZrSi030 annealed at 520 °C/10min)				
ZrSi032	After nucleation (ZrSi030 annealed at 520 °C/10min) & crystallization (annealed at 720 °C/20min)				
ZrSi040	0.094	0.267	0	0.639	0
ZrB050	0.020	0.209	0	0	0.771
ZrB060	0.038	0.174	0.008	0	0.780
ZrB070	0.057	0.145	0.008	0	0.790

The zirconium lithium silicate and zirconium lithium borate samples listed in Table 4 and two reference samples (monoclinic-ZrO_2, and zircon $ZrSiO_4$) were studied using Zr K-edge XAFS. These samples were prepared by Dr. Wolfram Höland's group at Ivoclar Vivadent (glass-ceramic research company). **Figure 13** shows a ternary plot (bottom) representing the composition of investigated ZRLS samples and ZRLB glasses based on analyzed composition. ZrB060 and ZrB070 contain Al_2O_3 content around 0.8 mol% but they were not applied for the ternary plot.

3.5 Absorber Preparation

Absorbers meant for transmission mode XAS spectroscopy must have chemical homogeneity, fine grains, uniform thickness, and must be free of pin holes. Also, in order

to achieve the best signal-to-noise ratio, absorption lengths should be between 2 to 3 as in **Figure 14** [22, 23].
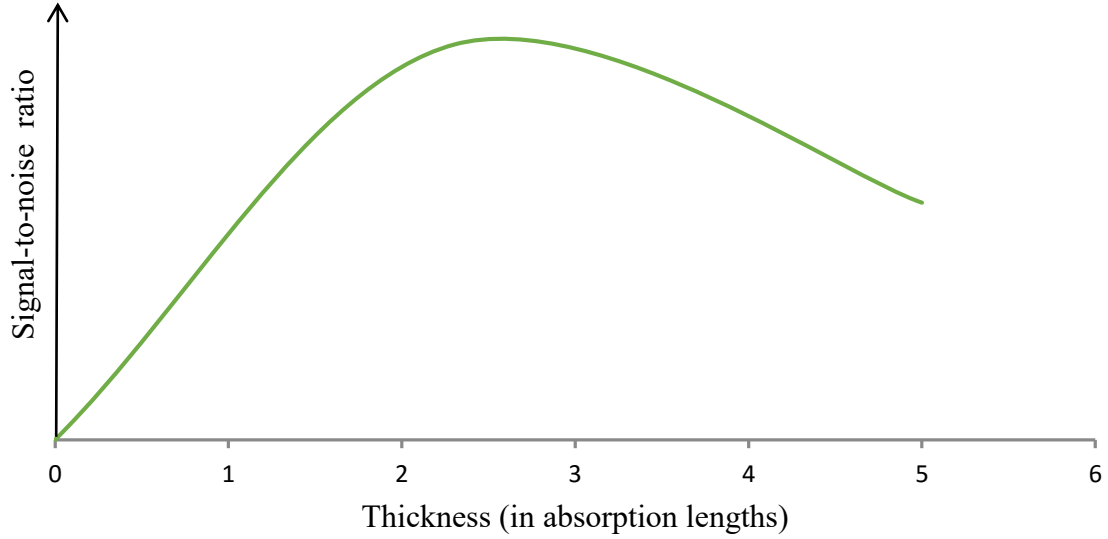
Figure 14. X-ray absorption signal-to-noise ratio as a function of absorption length [22–24]

The amount of finely ground sample required within a sample holder or in a pellet form was calculated using the Eq. (3.5.1).

$$\mu_{norm} = \rho\mu_m x = \frac{m}{V}\mu_m x = \frac{m}{A}\mu_m = ln\left(\frac{I_0}{I_t}\right) \qquad (3.5.1)$$

Where μ_{norm} is the normalized absorption coefficient, x is the sample thickness, m is the mass of the sample, V is the sample volume, A is the sample area, and μ_m is the mass absorption coefficient [22, 25]. For strongly absorbing samples with high concentration of target element, a low X-ray absorbing material, such as biobeads (polystyrene beads) was used to dilute the sample and avoid cracks. The glass samples and matrix were ground together in a mortar and pestle to a 200 mesh (< 47 μm) size using a sieve. Then, using a pelletizer (or a press), the mixture was pressed into a pellet

and sealed with Kapton tape (insulating heat resistant polyimide tape) as shown in **Figure 15**.

Figure 15. A pelletizer (left) [16] and a prepared ZRLS glass absorber covered with Kapton tape for the XAFS measurement (right).

3.6 XAS Measurement

X-ray absorption spectroscopy (XAS) data for ZRLS glass-ceramics, and ZRLB glasses were collected at beamline 10-BM-B and XAS data for REP glasses were collected at beamline 10-ID-B at the Advance Photon Source (APS), Argonne National Laboratory (ANL), Chicago, IL. The beamline 10-BM-B provides an X-ray energy range of 4–32 KeV with resolution ($\Delta E/E$) of 1 x 10^{-4} with an unfocused beam size of 50 mm x 3 mm using a Si (111) monochromator consisting of a cryo-cooled first crystal. The beamline 10-ID-B provides an X-ray energy range of 15–90 KeV with resolution ($\Delta E/E$) of 2 x 10^{-5} with an unfocused beam size of 2µm x 2µm. Typically, a XAS scan requires 50–200 eV before the absorption edge for the pre-edge fit and 100–1000 eV above the absorption edge for the post-edge fit. For our samples, 200 eV before and 1000 eV after the absorption edge was used for XAS scans for K-edge. Edge energies used for different samples are shown in **Table 5**.
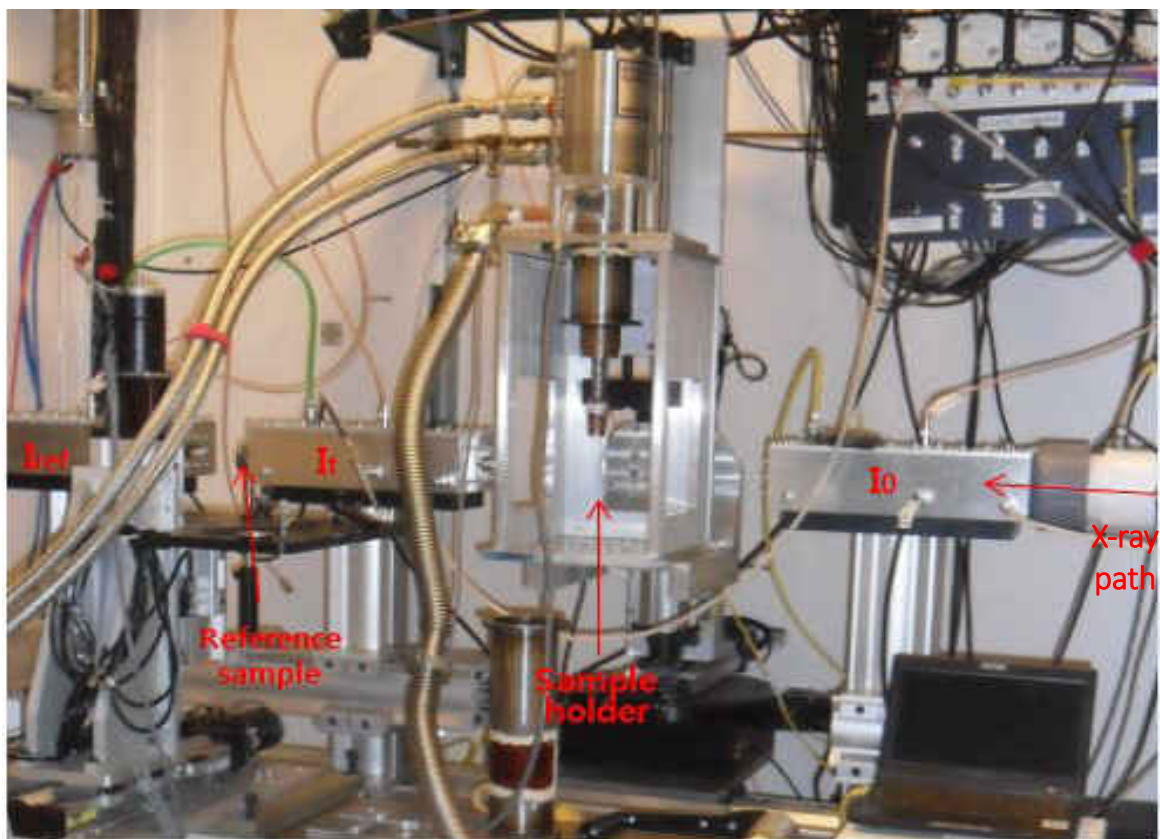
Figure 16. XAS transmission mode setup at the 10-BM-B beamline.

Table 5. Absorption edges and edge energies used at the 10-BM-B beamline and the 10-ID-B beamline for each element.

Element	Edge	Edge Energy
^{40}Zr	K-edge	17.998 KeV
^{59}Pr	K-edge	41.991 KeV
^{60}Nd	L_{III}-edge	6.208 KeV
^{68}Er	L_{III}-edge	8.358 KeV
^{66}Dy	L_{III}-edge / K-edge	7.790 KeV / 53.789 KeV
^{63}Eu	L_{III}-edge	6.977 KeV

A photograph of the XAS transmission mode experimental setup at the 10-BM-B beamline is shown in **Figure 16**. The XAFS data for Zr-doped samples were collected at

the Zr K-edge (17,998 eV) in the transmission mode at room temperature (300 K) and at low temperature (20 K) using a helium cryostat and standard ion chambers. The energy calibration was monitored using a third ion chamber and a Zr foil. The XAFS data for RE samples were collected at room temperature.

CHAPTER IV

DATA PROCESSING AND ANALYSIS

EXAFS analysis provides information about the coordination environment around

the absorbing atom. The main objective of the EXAFS measurement is to extract

structural parameters such as the coordination number CN, the interatomic distance R (the

average distance between the absorber and scatterer for single scattering SS path or the

average half-path length of multiple scattering MS path), and the XAFS Debye-Waller

factor σ^2 (DWF, attenuation of $\chi(k)$ due to the thermal and static disorder in the bond

length) with maximum possible accuracy [17, 18]. From EXAFS, two different types of

questions can be answered. First is the speciation, which is identifying the pureness,

possible impurities in the target sample, the proportion of each constituents of a mixed

sample, and the change in qualitative features of a sample with different temperature and

pressure conditions during measurement. Second is the characterization of the sample.

EXAFS can provide information about the oxidation state of particular elements, the

environment of a particular dopant element in a material, and the local structure

difference from the theoretical standard [18].

4.1 Data Processing

Measured XAS data are first reduced to a $\chi(k)$ function. Then they can be fit in k-

space and Fourier-transformed R-space. The data reduction process is usually

straightforward but one has to always check each stage of data reduction by graphically

checking the output. During the data reduction, background subtraction might be difficult since it requires a lot of manual intervention. Sometimes there might not be sufficient information to determine parameters in the model which makes modeling complicated. Often creativity, intuition, and predictions are required in order to minimize the number of fitting parameters.

From eq. (3.2.3), $\mu_0(E)$ is calculated during the data reduction process since it is not suitable to measure absorption for isolated absorber experimentally. Thus, one has to estimate the edge step $\Delta\mu_0(E_0)$ in order to scale it to 1 (normalization) and estimate the smooth background curve $\mu_0(E)$ (fitting a polynomial spline function to the normalized XAFS spectrum) in order to remove several extraneous contributions to the $\chi(k)$ signal, such as sample's thickness factor and absorptions from other elements in the sample.

Usually contributions from nearby atoms below R < 3 Å are strong and they show low frequency oscillations in the $\chi(k)$ spectra. More distant atoms (beyond R > 3 Å) show higher frequency oscillations. Waves scattered from two atoms in adjoining rows in the periodic table tend to have a scattering phase difference of about π radians [16]. When such two atoms are at similar distances from the absorber, the two scattered waves tend to interfere destructively and cancel out. A lesser degree of similar effect (destructive interference) occurs when there is any phase difference between scattered photo-electron waves [16, 18].

ATHENA is the front-end program for data processing (or data reduction) that uses IFEFFIT [26] for most numerical calculations and has a good integrated graphical interface in E, q, k, and R. IFEFFIT is an open source interactive program for XAFS analysis and is a flexible data reduction / fitting engine that allows a variety of user

interfaces. ATHENA is capable of many different features to handle data of interest at the beamline or for preparing the data to begin XAFS analysis [27]. Some of those features are converting measured raw data to absorption coefficient in energy $\mu(E)$, processing and plotting multiple data files simultaneously, merging data in energy, k-, and Fourier-transformed R-space, calibrating edge energy E_0, deglitching $\mu(E)$ data, fitting linear combinations of standards to XANES or EXAFS data, fitting peak functions to XANES data, removing background using the AUTOBK [28] algorithm, and much more [27].

4.1.1 Energy shift adjustment and edge energy determination

During an XAS measurement of a sample, several scans are measured and merged together to improve statistics. Often, not every scan is usable as measured. Two primary phenomena can corrupt a scan. One is that the energy calibration of the monochromator can shift during an experiment. The other is a glitch in incident intensity I_0 which may not be taken care of during normalization. Hence, before merging, some scans may need to be deglitched and all scans need to be aligned. During an EXAFS experiment, XAS data for an appropriate reference sample (I_{ref}) for which the edge energy is known is measured simultaneously, as shown in **Figure 16**. Measured transmitted intensity I_t and I_{ref} are used to align scans using the energy shift adjustment necessary.

E_0 is the energy necessary to remove the photoelectron from the target atom and it is always on or near the rising portion of the edge. Usually, E_0 can be selected roughly as the energy with the maximum of the first derivative. Alternatively, the zero crossing of the second derivative or the half-height of the edge step can also be used [16, 18, 27]. Derivative methods usually provide slightly higher values than half-height method, but it

can be adjusted during the data analysis process using ARTEMIS (ΔE will be determined). For this research, all scans were aligned using I_{ref} and then derivative methods were used to determine E_0, as shown in **Figure 17**.
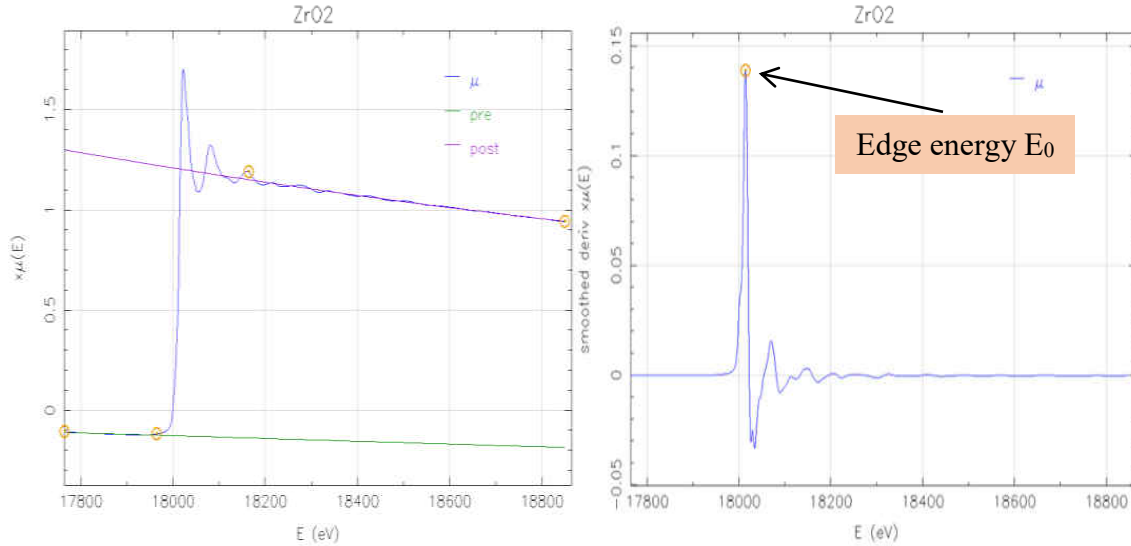
Figure 17. Experimental Zr K-edge XAFS spectra $\mu(E)x$ (left) of monoclinic-ZrO_2 and E_0 determined using the first derivative method (right). Determined E_0 is slightly higher than the actual edge energy of 17,998 eV for Zr K-edge.

4.1.2 Deglithching, truncation and averaging multiple scans

A scan might contain sharp spikes called 'glitches' at certain energies as mentioned above. Glitches are localized disturbances that can be removed by interpolating a value from the surrounding energy region or by removing certain points from the data. If several scans are performed on the same sample, glitches have no significant effect. Large glitches observed can be removed by manually removing selected data points and contributions from small glitches can be avoided from multiple scans

Truncation is the process of removing data in a scan that is outside the useful energy range so it will not interfere with analysis. Data may not be usable above or below

a certain energy due to another edge nearby (usually for L_{III}-edge) or due to a severe set of gltches.

Once data for individual scans are processed as described above, usable processed scans for a given sample were merged into one. Merged data sets were used in further analysis.

4.1.3 Normalization

The raw measured absorption coefficient before normalization process depends on sample thickness, gases used in detectors, filters and collimators used, absorber concentration, detector settings, amplifier settings, etc. In order to compare XAFS spectra, the measured data need to be normalized, which is removing external factors, such as experimental settings, and experimental conditions. The normalization process is scaling data in order to set the edge jump equal to 1, as shown in **Figure 18** (right) [17, 18]. It scales on a per-atom basis and factors out unnecessary parameters (irrelevant quantities), such as thickness factor *x* and concentration.
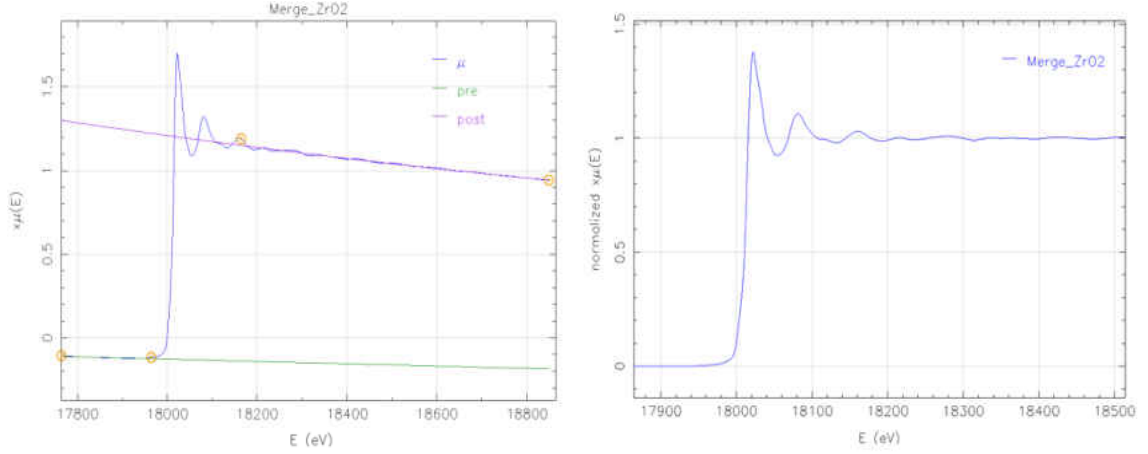
Figure 18. Experimental K-edge XAFS spectrum $\mu(E)x$ of monoclinic-ZrO$_2$ with green pre-edge and purple post-edge lines (left) and its normalized $\mu(E)x$ (right).

First, pre-edge and post-edge lines need to be defined by extrapolating them to E_0, as shown in **Figure 18** (left). The pre-edge region is a fairly featureless part of the XAFS spectrum and the range is typically from around 200 eV below E_0 up to 30 eV below E_0. Post-edge region contains valuable EXAFS oscillations and usually starts from 100 eV above E_0 up to near the end of the data. By fitting the pre-edge region and the post-edge region using low-order polynomial functions, the difference at E_0 (the edge jump) called the normalization constant $\Delta\mu_{Norm}(E_0)$ is set to 1. Since $\Delta\mu_{Norm}(E_0) = 1$, the difference between measured $\mu_{exp}(E)$ and $\mu_{Norm}(E)$ will be the XAFS spectrum $\chi(E)$, as shown in Eq. (4.1.3.1). After this stage, data reduction process is complete for XANES analysis. For EXAFS, more reduction processes are required.

$$\chi(E) = \frac{\mu(E) - \mu_0(E)}{\Delta\mu_0(E_0)} = \frac{\mu_{exp}(E) - \mu_{bkg}(E)}{\Delta\mu_{Norm}(E_0)} \qquad (4.1.3.1)$$

4.1.4 Background subtraction

The pre-edge and post-edge fits are to determine the normalization constant $\Delta\mu_{Norm}(E_0)$. The background subtraction is done after the normalization. EXAFS is the rapid oscillations of the absorption coefficient due to neighboring atoms that can be separated from the smoothly varying background [16]. The background is absorption due to an isolated absorber atom. Since we cannot measure this background, we use a spline function to define and remove background $\mu_{bkg}(E)$ from Eq. (4.1.3.1). It approximates $\mu_{bkg}(E)$ using an adjustable, smooth spline (cubic spline) function down to near E_0 region, as shown in **Figure 19**. We want to choose a spline that will match the low frequency components of measured $\mu_{exp}(E)$. Main reason is that we want to separate rapidly varying EXAFS oscillations from the slowly varying background. Also, Fourier transforming over a finite k-range does not perfectly localize signals for the Fourier-transformed (FTed) spectrum of $\chi(R)$ in R-space [16]. Thus, $\mu_{bkg}(E)$ is varied until the FTed spectrum of $\chi(R)$ between 0 and R_{bkg}, the low-R components of $\chi(R)$, is optimized [16–18]. The parameter 'R_{bkg}' is the R-space cutoff between the background and the data. Usually R_{bkg} is set to 1.0 Å or half of the first peak distance (near-neighbor distance) for the initial guess. By removing the background, the difference yields the XAFS spectrum $\chi(E)$ and then converted from energy to k-space to isolate $\chi(k)$.
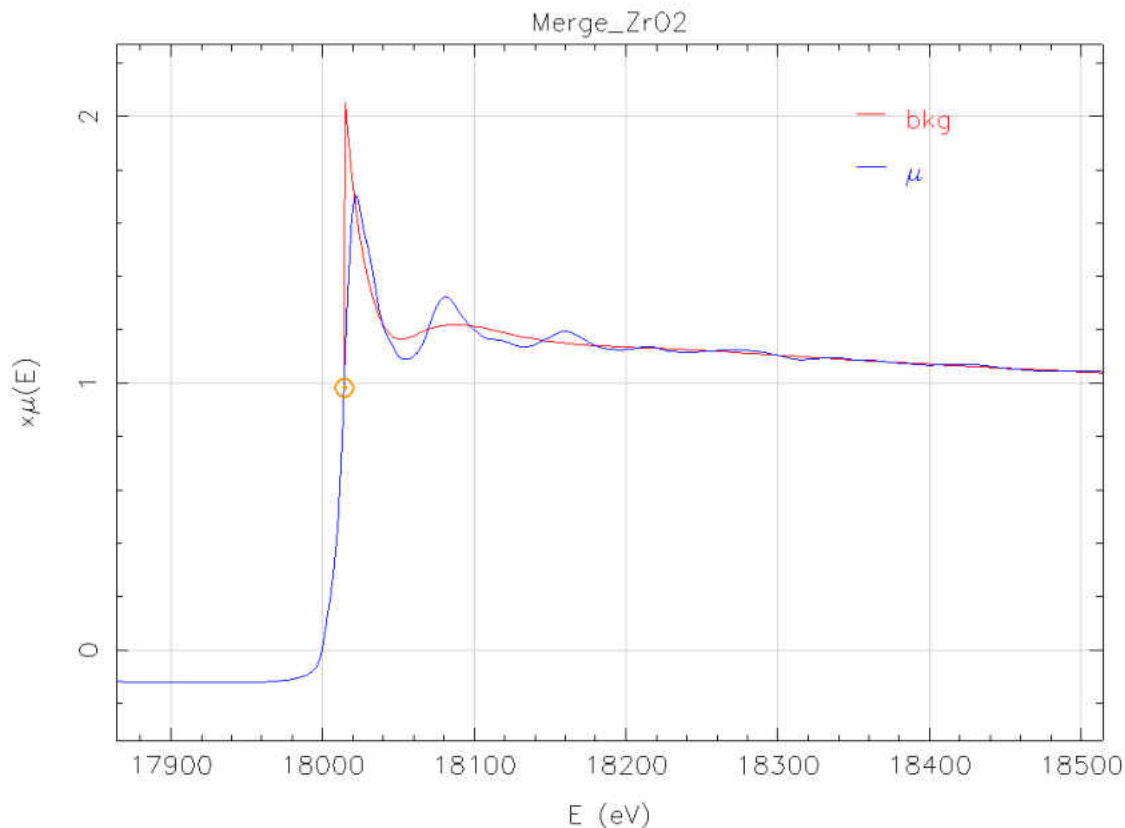
Figure 19. Background spline (red) approximated for K-edge XAFS spectrum $\mu(E)x$ of monoclinic-ZrO_2 (blue).

4.1.5 *k*-weighting

The reduced $\chi(k)$ function is a sum of damped sine waves [16, 18]. Thus amplitudes of $\chi(k)$ typically decay quickly at high *k*. When weighted by *k*, k^2, or k^3, the *k*-weighted $\chi(k)$ resembles sine waves of constant amplitude. Thus instead of using $\chi(k)$ directly, $k\chi(k)$, $k^2\chi(k)$, or $k^3\chi(k)$ is used for the presentation and analysis. Some suggest *k*-weighting is just making convenient choices for the analysis since a good fit shouldn't depend on the *k*-weight chosen [18]. Low *k*-weighting emphasizes low-*k* region and low-*Z* scatterers and high *k*-weighting emphasizes high-*k* region and high-Z scatterers. ATHENA and ARTEMIS provide *k*-weighting of 1, 2, and 3 at the same time to let users

perform three separate Fourier-transforms on the data and on the theoretical standard.

Each result from data is treated as if it is a separate data set, but the parameters used are applied simultaneously to provide best fitting results for all three. k-weighting of 2 or 3 is the most commonly used and recommended [16, 18, 22]. Usually a k-weight that provides a roughly constant amplitude for $\chi(k)$ is considered as a good choice. For this research, k-weighting of 3 was used [18]. The difference between $\chi(k)$ and $k^3\chi(k)$ is shown in **Figure 20**.
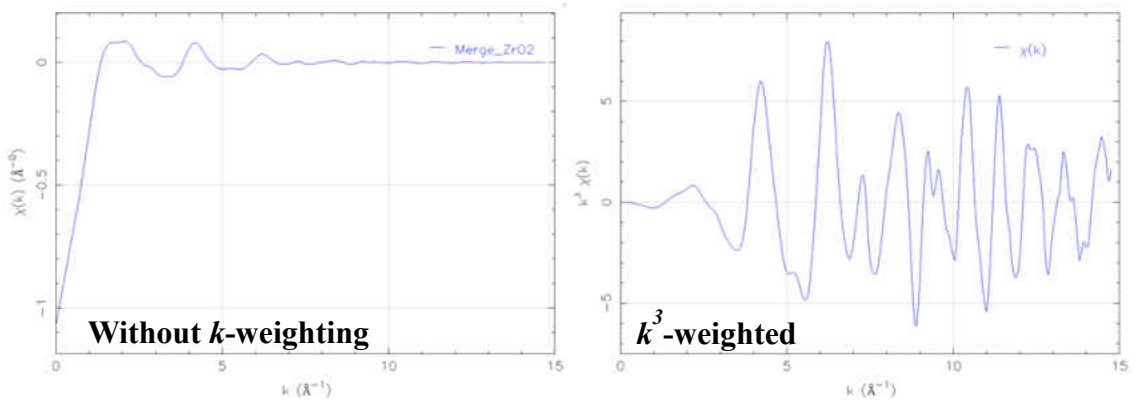
Figure 20. $\chi(k)$ (left) without weighting and $k^3\chi(k)$ (right) of monoclinic-ZrO_2.

4.1.6 Fourier transformation

For EXAFS data, Fourier transforming a finite k-range yields finite widths in R-space. Fourier-transform (FT) is a way to pick periodic frequencies out of the data from k-space to R-space [18]. FTs should not be considered as 'Radial distribution functions' because widths in R-space are determined by interval between k_{min} and k_{max} [16]. Sometimes peaks overlap when widths are greater than the distance difference Δr. Thus when peaks are closer than their widths (overlaps between peaks), resolving or separating different peaks clearly will be very hard. Also, when the truncation at one or both ends is

49

sharp, there will be additional 'ringing' of major peaks and sharp dependence on the *k*-range chosen. In order to avoid those problems, a window function, such as a Hanning window function or a Kaiser-Bessel window function, is applied before Fourier transformation, as shown in **Figure 21**. These two are the most commonly used window functions for EXAFS. A Hanning window function was used for RE-doped samples and a Kaiser-Bessel window function was used for Zr-doped samples with *dk* (width of the FT window sill in *k*-space) set to 1 Å^{-1} (1–3 Å^{-1} is a typical value range). Even though the Hanning window function is the most commonly used, the Kaiser-Bessel window function gave FTs that gave more reasonable parameters for Zr-doped samples. Changing window functions and *dk* often gives small changes to $\chi(k)$.
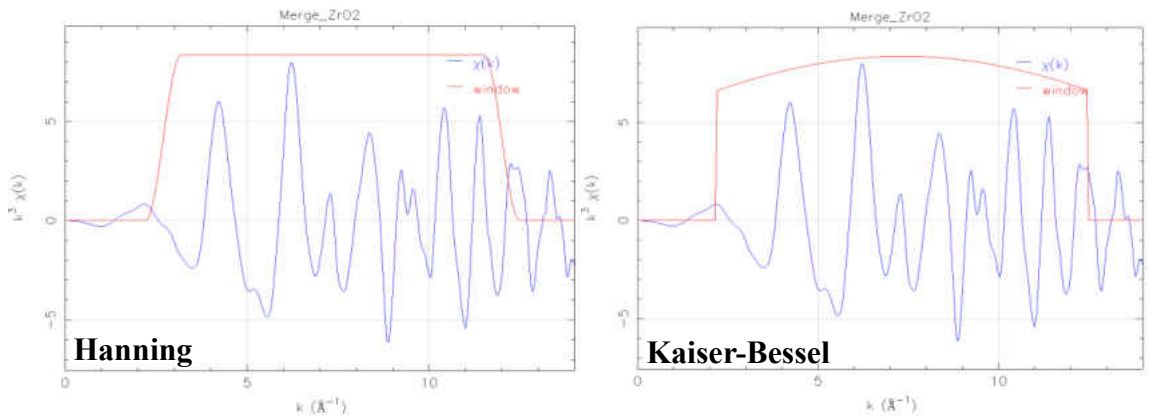
Figure 21. $k^3\chi(k)$ (Blue) of monoclinic-ZrO$_2$ with a Hanning window function (left) and a Kaiser-Bessel window function (right).

4.2 Data Analysis

The 'scattering path' is the path taken by the photoelectron as it propagates from the absorbing atom to neighboring atoms, scatters from one or more neighboring atoms, and returns to the absorbing atom. A photoelectron is said to take a single-scattering (SS) path when it scatters back from a neighboring atom and returns to the absorbing atom.

On the other hand, a photoelectron is said to take a multiple-scattering (MS) path when it undergoes more than one scattering event [18]. Based on structural information provided, FEFF builds atomic potentials (predicts how electrons will interact with an atom) and determines important scattering paths, *i.e.* builds paths from a selected central atom in a cluster of atoms, determines the degeneracy of the path, and filters out unimportant scattering paths. Using this information, FEFF creates a list of SS and MS paths and theoretically calculates $F(k)$ (effective scattering amplitude) from eq. (3.3.10) and $\delta(k)$ (effective scattering phase-shift) from eq. (3.3.9) for all scattering paths in a cluster of atoms. Because $F(k)$ and $\delta(k)$ depend on the atomic number Z of the scattering atom, EXAFS can be used to identify the atomic species of neighboring atoms.

The fitting of χ is usually done in R-space so that shells for fitting can be picked selectively, usually select SS paths and ignore MS paths. Fourier-transformed $\chi(R)$ contains real and imaginary parts and gives more meaningful fit statistics when we know that we're not fitting all the spectral features [22]. When modeling, we start with the atomic structure of a crystalline material which is expected to be similar to that of the sample for FEFF calculations [22]. When paths are generated by FEFF calculations, paths can be selected to model measured XAFS in ARTEMIS [22]. For our glass samples, only SS paths were considered since the contribution from MS paths was too small or negligible due to asymmetry and amorphous nature of our samples. Also, we started with crystal structures which were expected to share similar structural features with our samples.

4.2.1 Atomic shells

In $\chi(R)$, a peak corresponds to a coordination 'shell', *i.e.* a group of atoms at a similar distance from the absorber, or multiple 'shells' [16]. Thus the first peak in FTs is generally related with the nearest group of atoms and one of their SS paths is usually chosen as the first shell. The next peak in FTs corresponds to the second nearest group of atoms or groups of different atoms and one of their SS paths is usually chosen as the second shell or shells, etc. Often, a peak may contain more than one type of atoms. When that happens, $\chi(R)$ can be highly dependent on the transformed k-range, k-weighting, and other details [16]. Shells may or may not correlate well with the actual radial distribution since the width of a peak is not directly related to the width of an actual spatial distribution of atoms [16]. Also, the scattering phase-shift from the EXAFS equation ('$Sin(2kR_i + \delta_i(k))$' term) causes an average distance shift typically about 0.5 Å or so toward zero in the R-space because the position of the peak in R-space represents the average slope of the phase over the FT range in k-space [16]. But this shift in distance is consistent for different absorbing atoms which can be taken into account during data analysis.

4.2.2 *k*-range determination

Determining the most suitable k-range is critical to data analysis using ARTEMIS. Using processed data from ATHENA, usually a node between 2 and 3 Å^{-1} is chosen as k_{min} and considered as a fairly safe value (conservative choice). Choosing k_{min} is based on where $\chi(k)$ becomes independent of reasonable background choices [18].

Below $k_{min} = 2$ Å^{-1} (corresponds to 15 eV above E_0), the XAS spectra are heavily influenced by multiple scatterings, details of the background subtraction and the selection of E_0 [22]. For choosing k_{max}, we start from a node that looks clean (less noise) around 8 Å^{-1}. Then you choose more nodes at higher k. Then one has to compare FTs of chosen k-ranges. As you increase k_{max}, peaks are more resolved with larger amplitude and smaller width (well defined than before) in R-range. Eventually, noise will be greater than the signal at high k_{max}. The common approach is to set k_{max} to a value where the signal and noise is about the same size [22]. When noise is Fourier-transformed, they look like high frequency pulses in the real and imaginary part of the spectra all over in R-space. If you choose high k_{max}, then you might be adding more noise than the signal. Finding the cross over from a good change to a bad change in choosing the appropriate k-range is the main challenge. You can also use signal-to-noise ratio to choose k_{max}. By comparing FTs with different k-ranges, we need to choose a k-range relatively large (around $k = 8$ Å^{-1} or more) but not too large. Too many oscillations in R-space is an indication that the chosen k_{max} is too high. We can model the data and check the difference as you include more oscillations by increasing k_{max} to select the best k_{max} value [29]. Thus k_{max} is usually the end of useful data but when using k-weight of 2 or 3, the dependence in k_{max} will be low.

For RE-doped samples, $\chi(k)$ data was k^3-weighted and then Fourier transformed over the 3–8 Å^{-1} range. For Zr-doped samples, $\chi(k)$ data were k^3-weighted and then Fourier transformed over 2.7–9 Å^{-1} or 2.7–8 Å^{-1} range depending on noise contribution around k = 8 Å^{-1}. Two reference crystal samples (monoclinic-ZrO_2, zircon $ZrSiO_4$) were fitted using a wider k-range because their structures are well defined.

For chosen k-ranges, there might be small peaks due to multi-electron excitation effects [30, 31]. Multi-electron excitations have been observed and investigated in K- and L_{III}-edge EXAFS spectra of transition-metal ions [32, 33, 34]. Typically for RE-doped samples measured at L_{III}-edge, there might be a peak between $k = 5$ and 7 Å^{-1} due to the double-electron excitation (DEE: 2p, 4d $\rightarrow$ 5d, 5d) which distorts the fits (very small) [35]. Consequently, for glass samples DEE does not seriously affect the determination of the 1st shell for RE-doped samples. Also, for K-edge EXAFS spectrum of Zr-doped samples, a small peak around 7.7 Å^{-1} were also observed due to the DDE. In this work, the DDE effect was again minimized by applying k^3-weighting and using smaller k-range.

For choosing appropriate R-ranges for different shells, we chose R_{min} based on the background subtraction we used. Because the contribution from scattering paths corresponding to $R > 4$ Å was negligible for these samples, R_{max} was chosen to be around 4 Å [18].

4.2.3 Data modeling (one-shell or three-shell fitting method)

There are mainly five parameters fitted during the fitting process using ARTEMIS: the coordination number (or the degeneracy) N, the half-path length (or the mean distance for SS path) R, the XAFS Debye-Waller factor σ^2 (or the disorder parameter), the edge energy E_0, and the amplitude reduction factor S_0^2. These parameters are defined from the standard EXAFS equation in the section 3.3 [18]. We first run FEFF calculations using the known crystal structure of a reference sample whose atomic structure may be somewhat similar to that of the materials of interest in order to determine unknown parameters. Then, we feed those FEFF paths into ARTEMIS along

with measured data. FEFF will provide the nearest absorber-oxygen (scatterer) path that can be used to fit the first shell of our samples and we can choose more paths within the region of interest. Artemis allow users to choose suitable paths, limit (or constrain) the number of parameters used for certain paths, devise mathematical expressions for parameters.

After defining parameters of interest, one has to choose an appropriate number of parameters to use, according to available independent points in $\chi(k)$ data before fitting. The number of parameters used is limited by chosen k- and R-range by the Nyquist criterion [22, 27]. The Nyquist criterion allow users to compare independent points to variables being fit computed by IFEFFIT assuming that information is 'ideally packed' in the EXAFS signal. [22, 27] Thus, when fitting over a range in k or R, the number of independent points N_{ind} that need to be considered is given by

$$N_{ind} \approx \frac{2(k_{max} - k_{min})(R_{max} - R_{min})}{\pi} \approx \frac{(R_{max} - R_{min})}{\Delta R} \quad (4.2.1)$$

For modeling, crystalline standards such as $PrPO_4$, $NdPO_4$, $ErPO_4$, $DyPO_4$, $EuPO_4$, $Eu_1Na_1O_{12}P_4$, $Er_1Na_1O_{12}P_4$, $NdNa_{11}O_{12}P_4$, $ZrSiO_4$, and $\boldsymbol{\beta}$-ZrB_2O_5 [36] were used to create a relevant atomic coordination for FEFF calculations. For RE-doped glasses, fitting using one, two, or three shells was used depending on the signal-to-noise ratio at high k-region. For Zr-doped samples, two or three shells were used because signal-to-noise ratios were relatively higher than those for RE-doped glasses.

4.2.4 Parameter correlations and errors

In EXAFS, the reliability of fit parameters is greatly affected by correlations amongst them. If one of two correlated parameters is perturbed, then the uncertainty of the other one increases. From the EXAFS equation, S_0^2 and N are completely correlated and directly affect the amplitude. S_0^2 is usually a constant between 0.7 and 1 for experimental data [1, 16, 18] When you are fitting many shells, you may have enough information to uncouple the correlation between N and S_0^2 to fit them independently. When S_0^2 is defined, we can fix S_0^2 and focus on extracting out three main parameters, N_i, R_i, and σ_i^2 for selected paths according to the standard EXAFS equation. Also, N_i is strongly correlated with σ_i^2 at high k. In addition, when two shells overlap, the correlation between R_i and σ_i^2 increases and the uncertainties of both parameters increase [16, 18, 22].

4.2.4.1 Many-body effects (S_0^2 and λ_k)

The many-body effects depend on instantaneous positions of other electrons. In the solid state, many-body effects are negligible in most cases [17]. Interactions between electrons thorough Coulomb potential are related with many-body effects, such as λ_k (mean free path) and passive elections related effect S_0^2 (amplitude reduction factor). Due to many-body effects, small steps can be generated in $\mu(E)$. If known, it can be subtracted out by checking low-R background that is not removed [16]. λ_k is related with the contribution from electron-electron scattering (extrinsic losses) and ARTEMIS provides ways to account for effects of λ_k using empirical and theoretical models [18, 22].

S_0^2 is related with the relaxation of the absorbing atom due to the presence of the core-hole (intrinsic losses) [22]. Remaining electrons (passive electrons) in the absorber relaxes to the presence of the core-hole left behind. For experimental data for a particular beamline, S_0^2 is usually a constant due to energy resolution. When empirical effects, such as detector response and sample inhomogeneity are small, S_0^2 can be determined from a well-known standard (crystal reference samples) that was measured at the same time as your sample [22].

For RE-doped samples, no standards were measured under identical experimental conditions (at the same beamline under similar conditions) so S_0^2 was set to 1.0 according to previous EXAFS researches for RE-doped samples [37, 38]. For Zr-doped samples, two well-known standards (monoclinic-ZrO_2 and zircon) were measured under identical experimental conditions and their EXAFS fits were performed with known parameters (N_i, and R_i) fixed or constrained to their reported values. S_0^2 for Zr-doped samples was found to be about 1.00 for Zr-doped samples and confirmed with the published result [34].

CHAPTER V

RESULTS AND DISCUSSION

5.1 Rare-Earth Sodium Phosphate Glasses

5.1.1 Praseodymium-doped sodium phosphate glasses

Figure 22 shows k^3-weighted $\chi(k)$ of the four samples in k-space. **Figure 23** shows their Fourier transforms for a k-range of 3–8 Å^{-1}. This relatively narrow k-range is dictated by the relatively low signal-to-noise ratio at high k. Dominant peaks around 1.9 Å (without phase-shift correction) correspond to the nearest Pr-O coordination and show little change between four samples with different RE concentrations. Even though Fourier transforms shown in **Figure 23** have not been corrected for the phase-shift (typically around 0.5 Å), it is taken into account during the fitting process.

Figures 24 and **25** show experimental spectra (dotted line) and their fits (solid line) in k-space and R-space, respectively.

Praseodymium Polyphosphate crystalline structure $Pr(PO_3)_3$ [36] was used to calculate the scattering paths. The spectra were fitted using a one-shell model fit (a first oxygen shell using Pr-O single scattering path) due to low signal-to-noise ratio at high k region ($k > 8$). Due to narrow k-range used, the number of independent variables was kept to a minimum. The amplitude reduction factor S_0^2 was set to 1 based on previous EXAFS studies [37, 38].
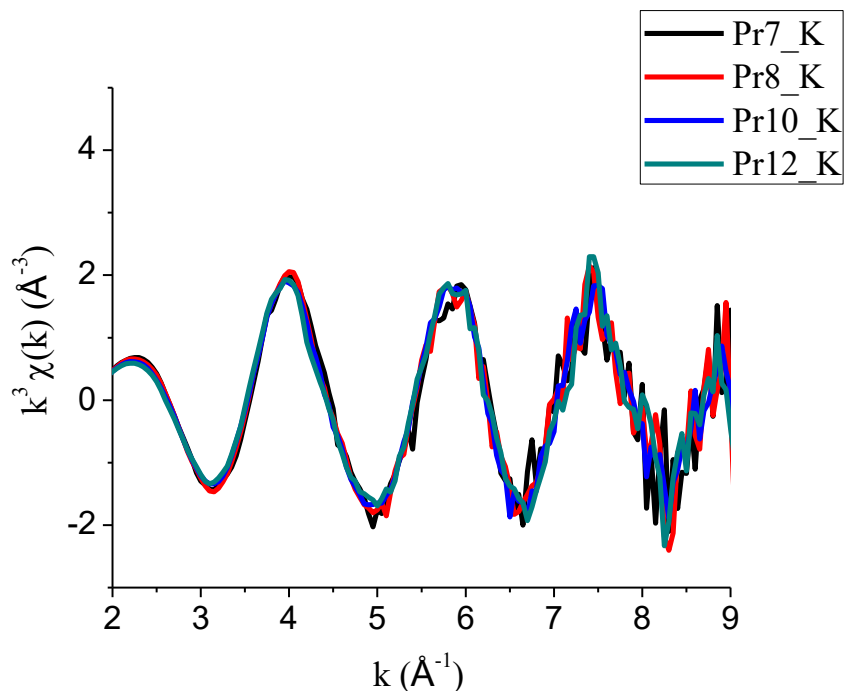
Figure 22. Comparison of measured $k^3\chi(k)$ (Å^{-3}) of praseodymium-doped sodium phosphates with four different compositions.
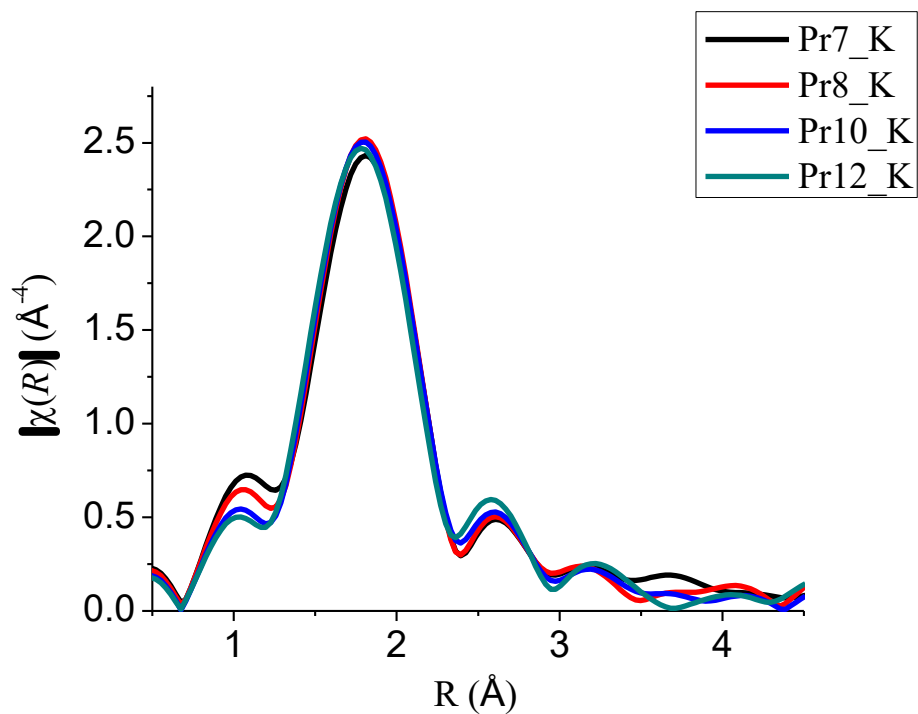
Figure 23. Comparison of Fourier transforms of $k^3\chi(k)$ (Å^{-3}) functions shown in **Figure 22.**
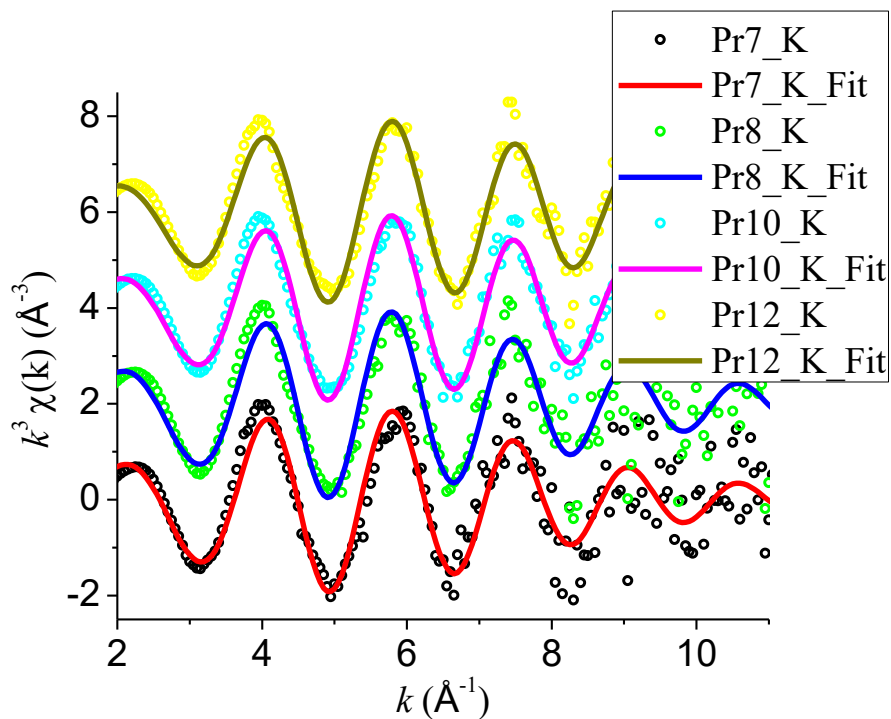
Figure 24. Experimental (dotted line) EXAFS functions $k^3\chi(k)$ (Å^{-3}) and their best fits (solid line) of praseodymium-doped sodium phosphates with four different compositions. The spectra and their fits are vertically separated by 2 Å^{-3} for clarity.
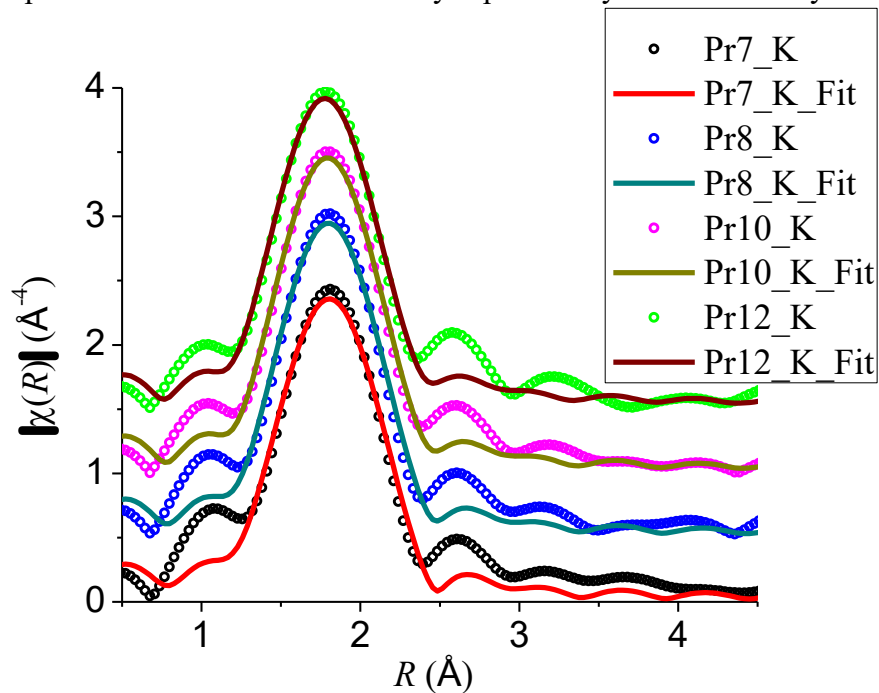
Figure 25. Fourier transforms of experimental (solid lines) EXAFS functions in R-space and their fits (dotted lines). The spectra and their fits are vertically separated by 0.5 Å^{-4} for clarity.

Table 6. Structural parameters obtained for praseodymium-doped sodium phosphates.

Sample	Atomic shell correlation	CN	R (Å)	σ^2 (Å^2)
Pr7 $x = 0.005$ $y = 0.395$	Pr-O(1)	10.8 ± 1.7	2.45 ± 0.04	0.013
Pr8 $x = 0.010$ $y = 0.390$	Pr-O(1)	10.4 ± 1.3	2.45 ± 0.03	0.012
Pr10 $x = 0.030$ $y = 0.370$	Pr-O(1)	9.5 ± 0.7	2.44 ± 0.02	0.011
Pr12 $x = 0.050$ $y = 0.350$	Pr-O(1)	9.1 ± 0.7	2.43 ± 0.02	0.011

Table 6 shows fit parameters for praseodymium-doped sodium phosphates. The first shell oxygen coordination number (CN_{Pr-O}) gradually decreases from 10.8 to 9.1 as Pr_2O_3 content increases which matches the range of 6 to 10 for metaphosphates with higher Pr_2O_3 content found by Anderson *et al* [40]. The high values of CN_{Pr-O} are due to the lower Pr_2O_3 content in metaphosphate glasses. A first oxygen shell was found at the distance of 2.43–2.45 Å which is in good agreement with the HEXRD data [41]. The mean square radial displacement (σ^2) was typically between 0.011–0.013 Å^2 and decreases as Pr_2O_3 content x increases.

5.1.2 Neodymium-doped sodium phosphate glasses

Figure 26 shows k^3-weighted $\chi(k)$ in k-space. **Figure 27** shows their Fourier transforms obtained using a k-range of 3–8 Å^{-1}. The height of dominant peaks around 1.9 Å correspond to the nearest Nd-O coordination and shows a gradual decrease as Nd_2O_3

content increases. EXAFS functions $k^3\chi(k)$ in **Figure 26** show double-electron excitation

(*2p, 4d → 5d, 5d*) around k = 6.1 Å^{-1} which is expected for L$_{III}$-edge EXAFS

spectroscopy [35]. As mentioned earlier DEE effect does not seriously affect the

determination of the 1st shell properties. and the relatively narrow *k*-range (3–8 Å^{-1}) used

further reduces artifacts due to this effect.

      Figure 28 shows experimental spectra (dotted lines) and their fits (solid lines) in

k-space, and **Figure 29** shows FTs (dotted lines) and their fits (solid lines) in *R*-space.

Available *k*-range is limited due to low signal-to-noise ratio at high *k* and L$_{II}$-edge

interference near L$_{III}$-edge.

      The crystalline structure of sodium neodymium metaphosphate (NdNaP$_4$O$_{12}$) [42]

was used to calculate the scattering paths. The spectra were fitted using a three-shell

model, *i.e.*, a first oxygen shell using Nd-O(1) single scattering path, a second

phosphorus shell using Nd-P single scattering path, and a third oxygen shell using Nd-

O(2) single scattering path. A Nd-Na single scattering path were not considered due to

lower contributions from a Nd-Na path and the resolution limits for EXAFS. From FEFF

calculations, the nearest Nd-Na coordination number is 1 and the path distance is 3.609 Å

for NdNaP$_4$O$_{12}$ [42].

      Due to narrow *k*-range (between 3 and 8) used, the number of independent

variables was kept to a minimum by using the same mean square radial displacement (σ^2)

for same shell types during the simultaneous fitting process. The amplitude reduction

factor S_0^2 was set to 1 according to the previous EXAFS studies [37, 38].

Figure 26. Comparison of measured $k^3\chi(k)$ (Å^{-3}) of neodymium-doped sodium phosphates with three different compositions. The arrow suggests the double-electron excitation (*2p, 4d → 5d, 5d*) [35].
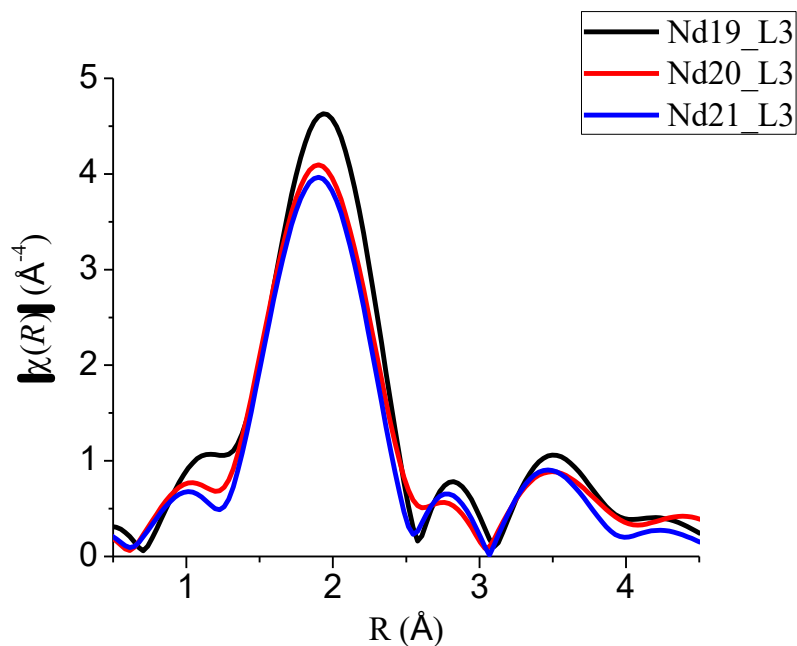
Figure 27. Comparison of Fourier transforms of $k^3\chi(k)$ (Å^{-3}) functions shown in Figure 26. Increasing height of the peak at around 1.9 Å with decreasing *x* indicates that nearest neighbor oxygen coordination number (CN$_{RE-O}$) increases as the neodymium concentration decreases.
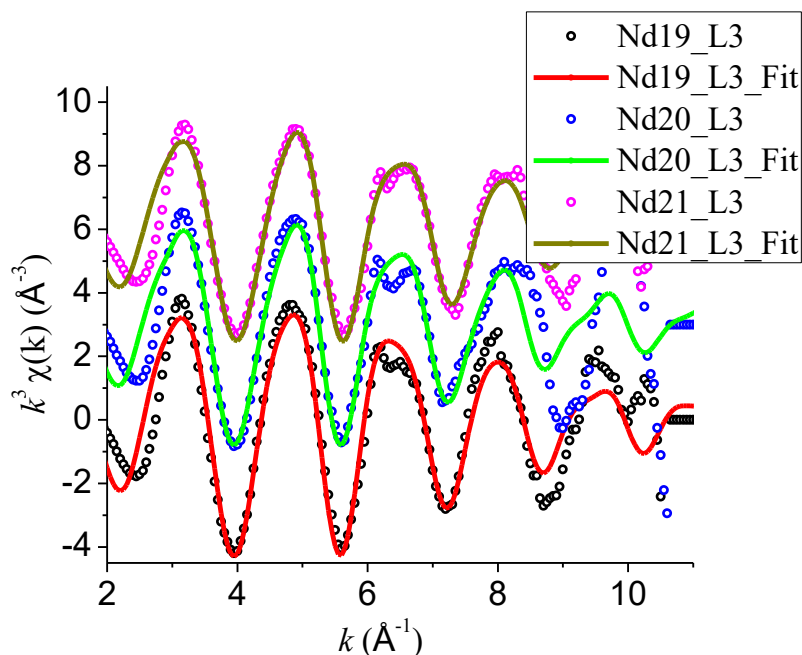
Figure 28. Experimental (dotted line) EXAFS functions and their best fits (solid lines) of neodymium-doped sodium phosphates with three different compositions. The spectra and their fits are vertically separated by 3 Å^{-3} for clarity.

Figure 29. Fourier transforms of experimental (dotted lines) EXAFS functions in *R*-space and their fits (solid lines). The spectra and their fits are vertically separated by 2 Å^{-4} for clarity.

Table 7. Structural parameters obtained for neodymium-doped sodium phosphates.

| Sample	Atomic shell correlation	CN	R (Å)	σ^2 (Å^2)
Nd19_L3	Nd-O(1)	8.3 ± 0.6	2.43 ± 0.02	0.011
$x = 0.047$	Nd-P	1.8 ± 1.5	3.81 ± 0.07	0.013
$y = 0.337$	Nd-O(2)	7.7 ± 4.0	4.56 ± 0.06	0.010
Nd20_L3	Nd-O(1)	7.3 ± 0.5	2.41 ± 0.02	0.011
$x = 0.083$	Nd-P	1.5 ± 1.3	3.80 ± 0.07	0.013
$y = 0.328$	Nd-O(2)	7.9 ± 3.6	4.57 ± 0.05	0.010
Nd21_L3	Nd-O(1)	6.9 ± 0.4	2.40 ± 0.02	0.012
$x = 0.127$	Nd-P	1.5 ± 1.1	3.80 ± 0.07	0.013
$y = 0.257$	Nd-O(2)	5.9 ± 3.0	4.53 ± 0.06	0.010

Table 7 shows structural parameters obtained from fits. The first shell $CN_{Nd-O(1)}$ increased from 6.9 to 8.2 as Nd_2O_3 content decreased from 0.127 to 0.047. This observation is consistent with reported results of 6 to 10 found by Bowron *et al* [43]. A first oxygen shell was found at the distance of 2.40–2.43 Å which is slightly higher than the 2.22–2.37 Å range found with High Energy X-ray Diffraction (HEXRD) technique by Gunapala [44]. As the first shell $CN_{Nd-O(1)}$ increases $R_{Nd-O(1)}$ also increases with decreasing Nd_2O_3 content.

A second shell was found at the distance of 3.8 Å, which is slightly higher than the reported value for metaphosphates without sodium (binary metaphosphate glasses) [37, 40, 43] and the mean distance range of 3.60–3.73 Å from the reported crystal structure [42]. But the values of Nd-P distance are consistent with L_{III}-edge EXAFS results of 3.85–3.87 Å for (binary metaphosphate glasses) by Karabulut *et al* [45]. The reduction of second shell's distance from 3.85 Å to 3.80 Å, is due to the decrease in Nd_2O_3 content. For the second phosphate shell, CN_{Nd-P} around the neodymium is found to vary between 1.5–1.8. The distance between a neodymium atom and its third oxygen

shell is 4.53–4.57 Å while $CN_{Nd-O(1)}$ of the third oxygen shell is between from 5.9–7.9. Also, no RE-RE correlations were found within the limits of the data (up to around 4.5 Å).

5.1.3 Europium-doped sodium phosphate glasses

Figures 30 and **31** show k^3-weighted $\chi(k)$ and their FTs in the k-range of 3–8 Å^{-1}, respectively. Major peaks around 1.9 Å represent near-neighbor Eu-O coordination. EXAFS functions $k^3\chi(k)$ in **Figure 30** show double-electron excitation (DEE: 2p, 4d → 5d, 5d) around k = 6.3 Å^{-1} which in agreement with previously reported data [35].

Figure 32 shows experimental spectra (dotted lines) and their fits (solid lines) in k-space, and **Figure 33** shows FTs (dotted lines) and their fits (solid lines) in R-space. In **Figures 31** and **33**, the ripples observed at values less than 1.25 Å are low-frequency noise due to Fourier components of the smooth background function ($\mu_{bkg}(E)$) and side lobes generated during the Fourier transform. During the fitting process, ripples below 1.25 Å were not considered for the fitting in R-space.

The crystalline structure of europium phosphate (EuPO$_4$) [46] was used to calculate the scattering paths. The spectra were fitted using a two-shell model (a first oxygen shell using Eu-O(1) single scattering path, and a second phosphorus shell using Eu-P single scattering path). A single mean square radial displacement (σ^2) was used for a given shell. The amplitude reduction factor S_0^2 was set to 1 according to the previous EXAFS studies [37].
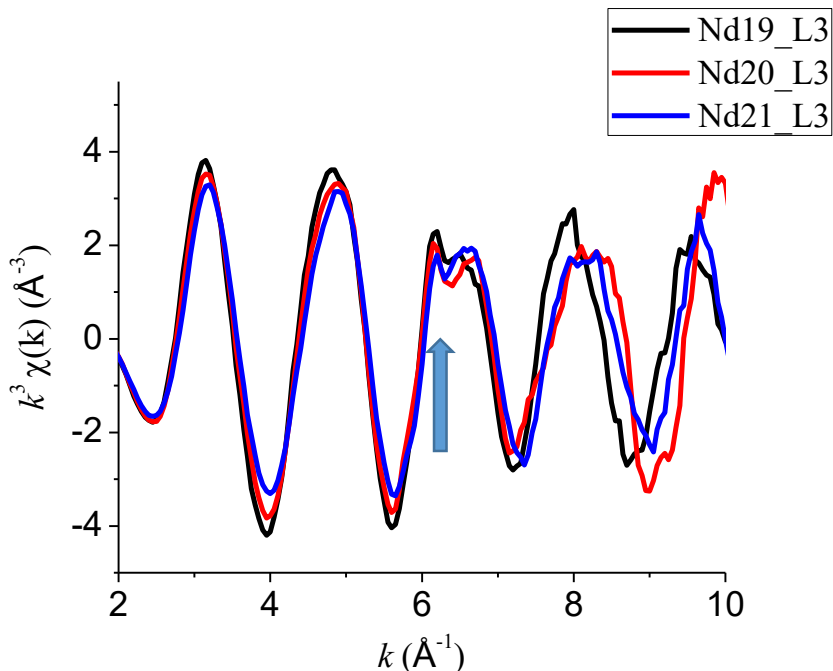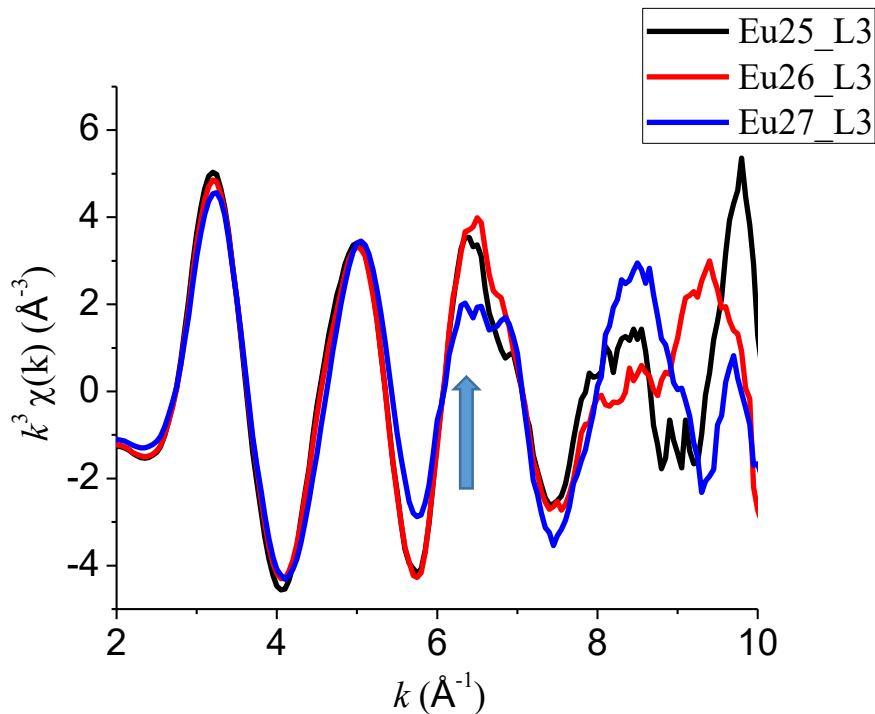
Figure 30. Comparison of measured $k^3\chi(k)$ (Å^{-3}) of europium-doped sodium phosphates with three different compositions. The arrow around 6.3 Å^{-1} suggests the double-electron excitation (*2p, 4d → 5d, 5d*) [35].

Figure 31. Comparison of Fourier transforms of $k^3\chi(k)$ (Å^{-3}) functions shown in Figure 30.

Figure 32. Experimental (dotted line) EXAFS functions and their best fits (solid lines) of europium-doped sodium phosphates with three different compositions. The spectra and their fits are vertically separated by 3 Å^{-3} for clarity.
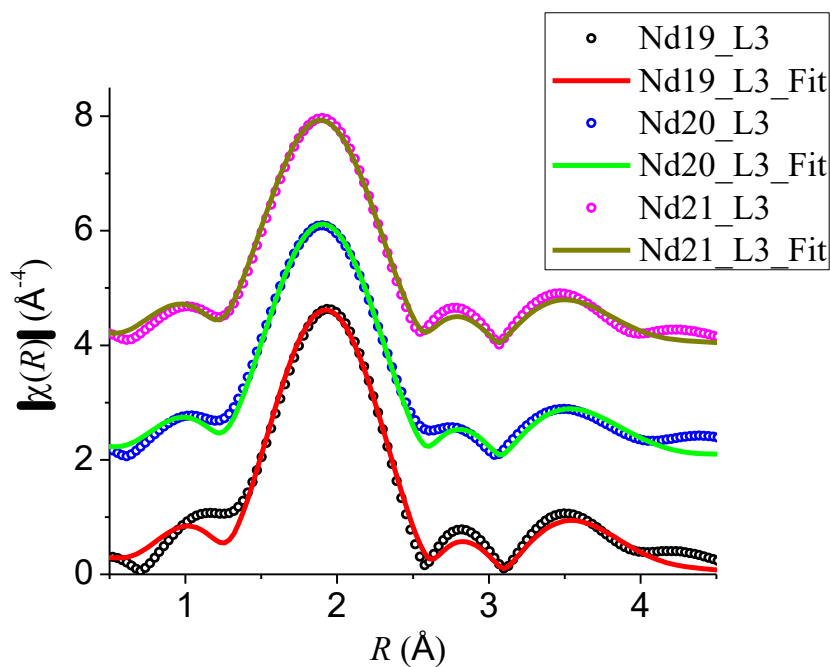

Figure 33. Fourier transforms of experimental (dotted lines) EXAFS functions in *R*-space and their fits (solid lines). The spectra and their fits are vertically separated by 2 Å^{-4} for clarity.

Table 8. Structural parameters obtained for europium-doped sodium phosphates.

Sample	Atomic shell correlation	CN	R (Å)	σ^2 (Å^2)
Eu25	Eu-O(1)	8.7 ± 0.5	2.38 ± 0.01	0.013
x = 0.052	Eu-P	3.8 ± 1.0	3.75 ± 0.03	0.011
y = 0.369				
Eu26	Eu-O(1)	8.8 ± 0.4	2.37 ± 0.01	0.013
x = 0.083	Eu-P	3.4 ± 0.8	3.74 ± 0.02	0.011
y = 0.320				
Eu27	Eu-O(1)	7.5 ± 0.5	2.36 ± 0.01	0.013
x = 0.130	Eu-P	3.2 ± 0.9	3.78 ± 0.03	0.011
y = 0.251				

Table 8 gives structural parameters obtained from data analysis. Eu-O coordination numbers for Eu25 (x = 0.052), and Eu26 (x = 0.083) were similar between 8.7 to 8.8 and decreased to 7.5 for Eu27 (x = 0.130). A first oxygen shell distances was between 2.38 and 2.36 Å which is slightly higher than the HEXRD data of 2.35 Å [43] and EXAFS studies for binary metaphosphates (x = 0.218) of 2.30–2.31 Å [48].

A second shell (Eu-P) was found at a distance of 3.74–3.78 Å which is similar to that was observed in our neodymium series and that reported for binary neodymium metaphosphates by Bowron *et al* [47]. However, it must be noted that smaller values (3.34 Å) for this second shell in binary metaphosphates have been reported elsewhere [48]. When compared with distance range between 3.11–3.71 Å of reported crystal structure of $EuPO_4$ [46], these results show the random network nature of the amorphous material. The previous reported results with shorter distances of 3.33–3.34 Å are, for binary metaphosphates with higher Eu_2O_3 content (x = 0.218) [48]. Europium metaphosphates with lower Eu_2O_3 content reflect the increase in shell distances for both Er-O mean distance and Er-P mean distance.

5.1.4 Dysprosium-doped sodium phosphate glasses

Figure 34 shows k^3-weighted $\chi(k)$ of two samples (Dy22 and Dy23) derived from K-edge absorption data and **Figure 36** shows k^3-weighted $\chi(k)$ of two samples (Dy22 and Dy24) derived from L_{III}-edge absorption data. **Figures 35** and **37** show their FTs in the k-range of 3–8 Å^{-1}, respectively. Major peaks around 1.8–2.0 Å represent the nearest Dy-O coordination. Note that there is no evidence of DEE in L_{III}-edge spectra as expected. [35].

The crystalline structure of dysprosium phosphate (DyPO$_4$) [49] was used to calculate the scattering paths. The L_{III}-edge spectra of dysprosium-doped sodium phosphates were fitted using a three-shell model (a first oxygen shell using Dy-O(1) single scattering path, a second phosphorus shell using Dy-P single scattering path, and a third oxygen shell using Dy-O(2) single scattering path). However, due to the low signal-to-noise ratio at higher k, K-edge spectra were analyzed using a single Dy-O shell.

Figure 38 shows K-edge experimental spectra (dotted lines) and their fits (solid lines) in k-space, and **Figure 40** shows L_{III}-edge experimental spectra (dotted lines) and their fits (solid lines) in k-space. **Figure 39** shows K-edge FTs (solid lines) and their fits (dotted lines) in R-space, and **Figure 41** shows L_{III}-edge FTs (solid lines) and their fits (dotted lines) in R-space. They are vertically shifted for comparison between samples. The amplitude reduction factor S_0^2 was set to 1.
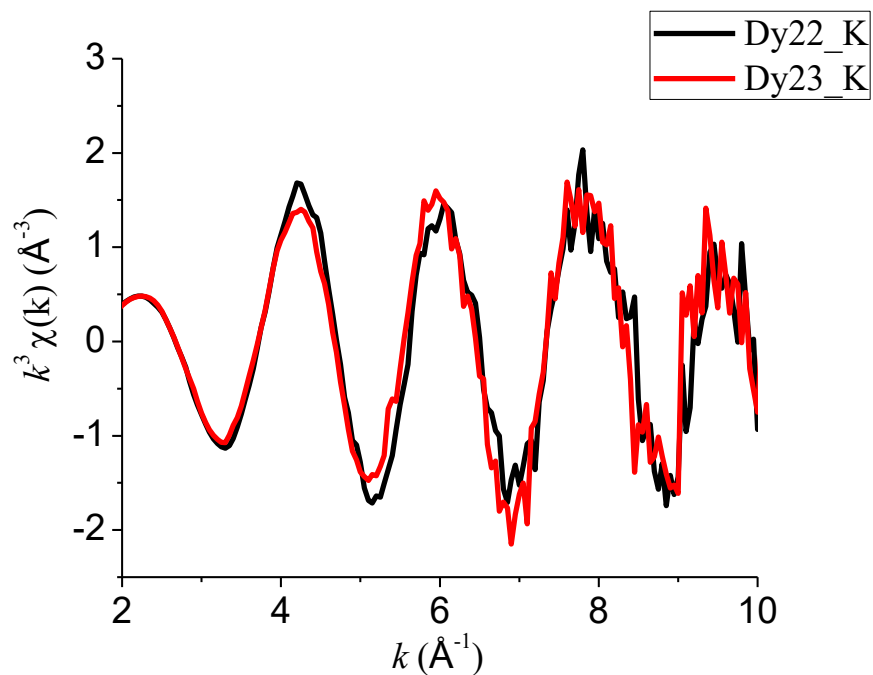
Figure 34. Comparison of measured $k^3\chi(k)$ (Å^{-3}) of dysprosium-doped sodium phosphates with two different compositions (x = 0.046 for Dy22 and x = 0.076 for Dy23).
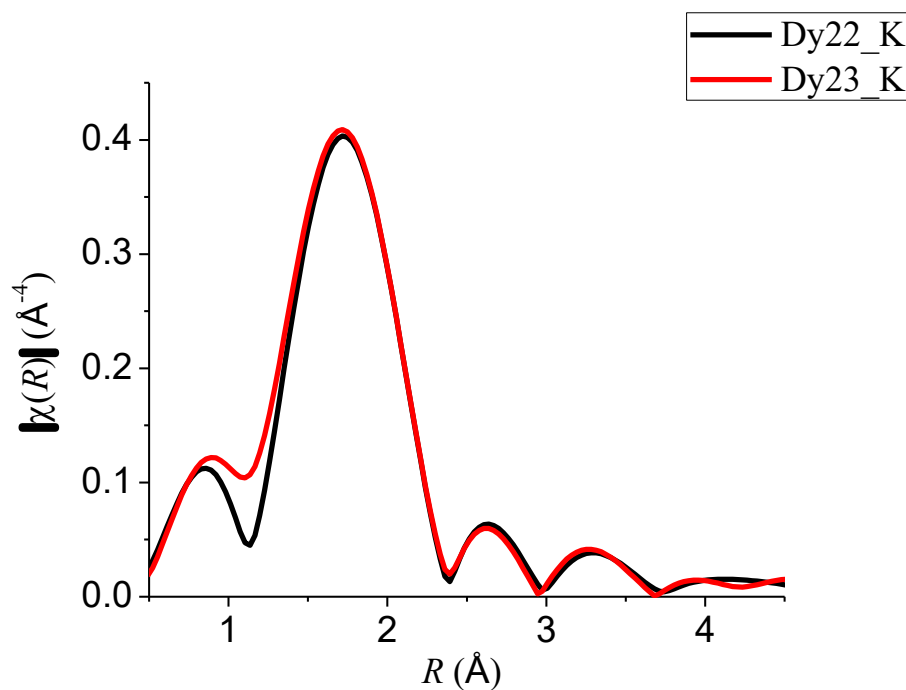
Figure 35. Comparison of Fourier transforms of $k^3\chi(k)$ (Å^{-3}) functions shown in Figure 34.
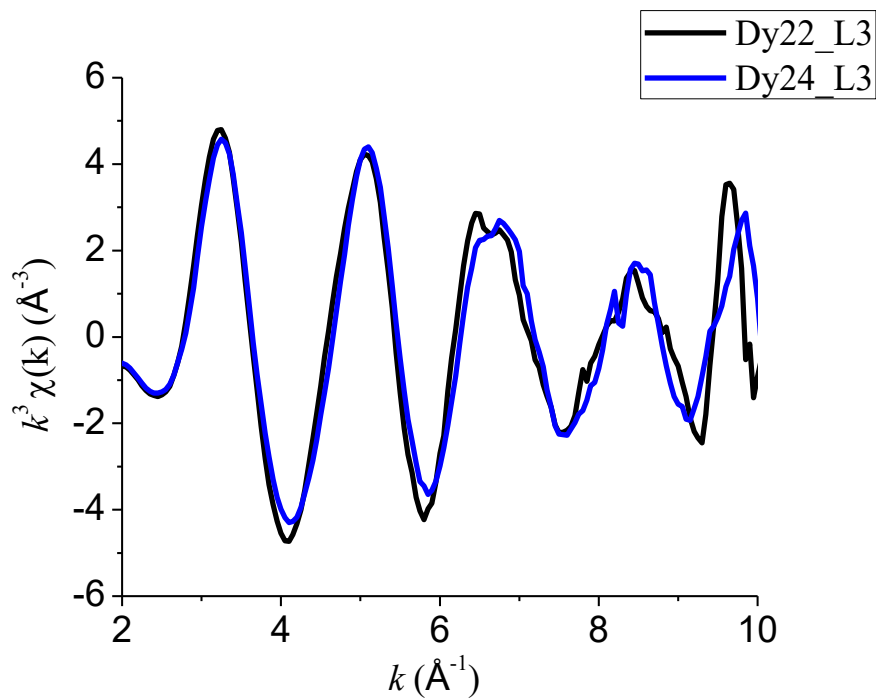
Figure 36. Comparison of Fourier transforms of $k^3\chi(k)$ (Å^{-3}) functions of dysprosium-doped sodium phosphates with two different compositions (x = 0.046 for Dy22 and x = 0.121 for Dy23).
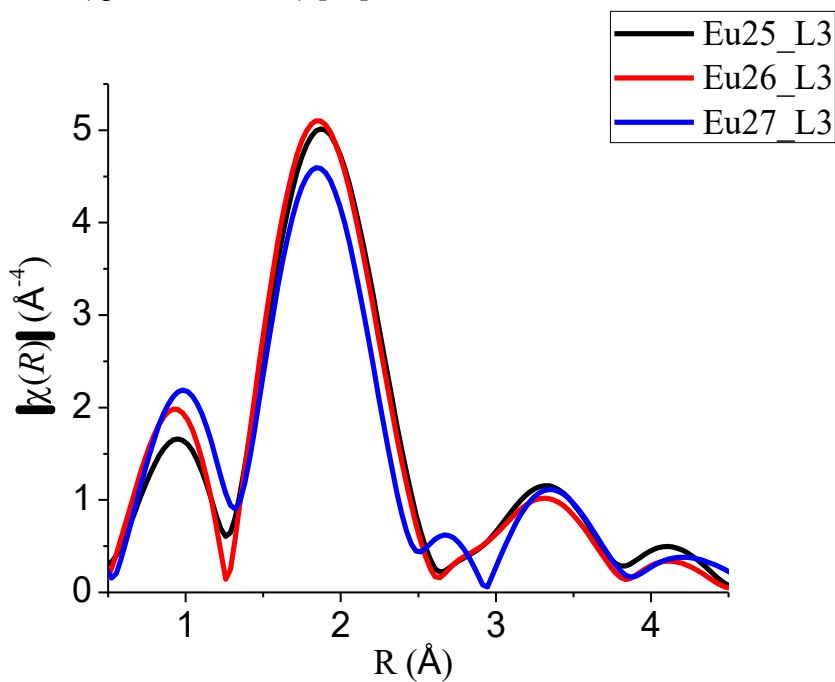

Figure 37. Comparison of Fourier transforms of $k^3\chi(k)$ (Å^{-3}) functions shown in Figure 36.
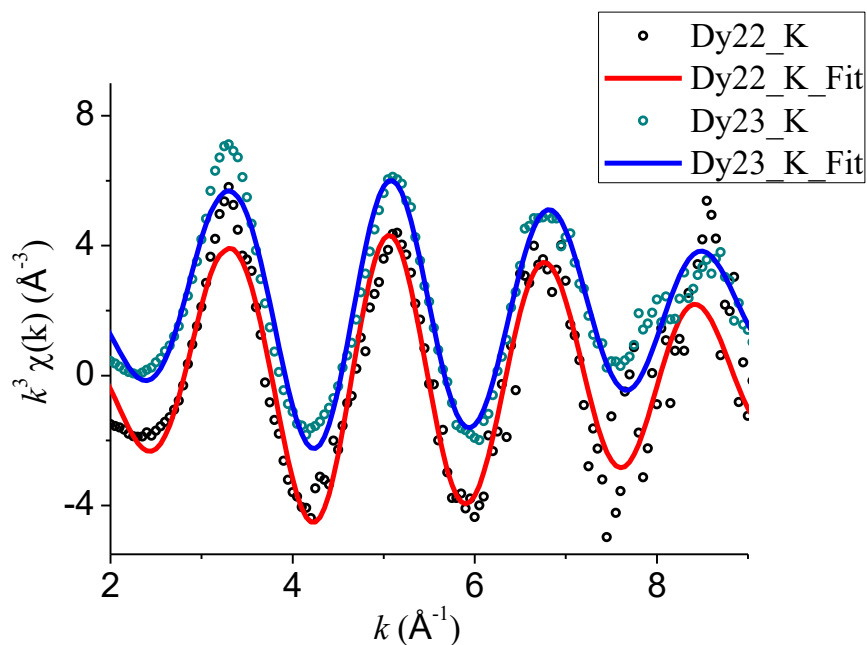
Figure 38. Experimental (dotted line) EXAFS functions $k^3\chi(k)$ and their best fits (solid lines) of dysprosium-doped sodium phosphates with two different compositions measured at K-edge. The spectra and their fits are vertically separated by 2 Å^{-3} for clarity.
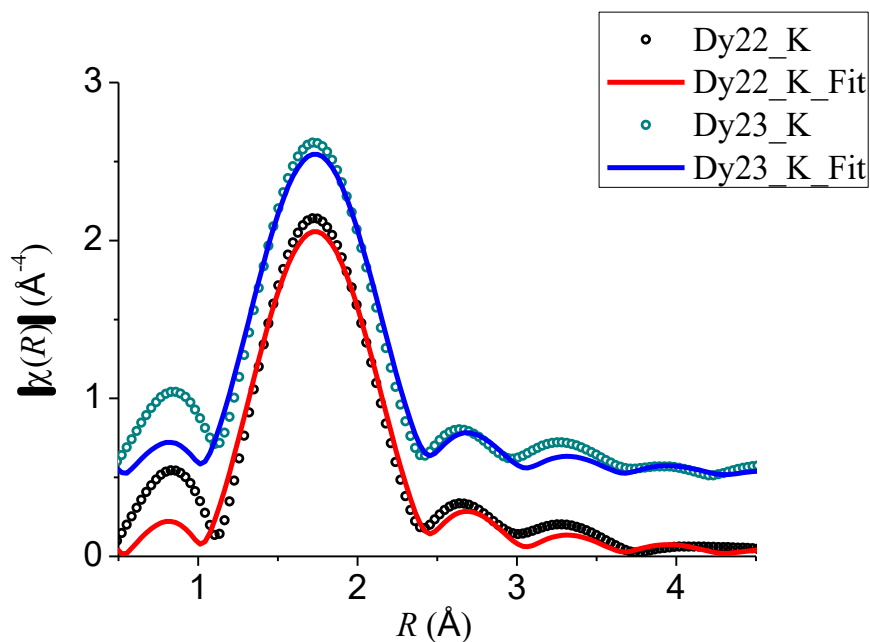
Figure 39. Fourier transforms of experimental (dotted line) EXAFS functions in *R*-space and their fits (solid lines) measured at K-edge. The spectra and their fits are vertically separated by 0.5 Å^{-4} for clarity.
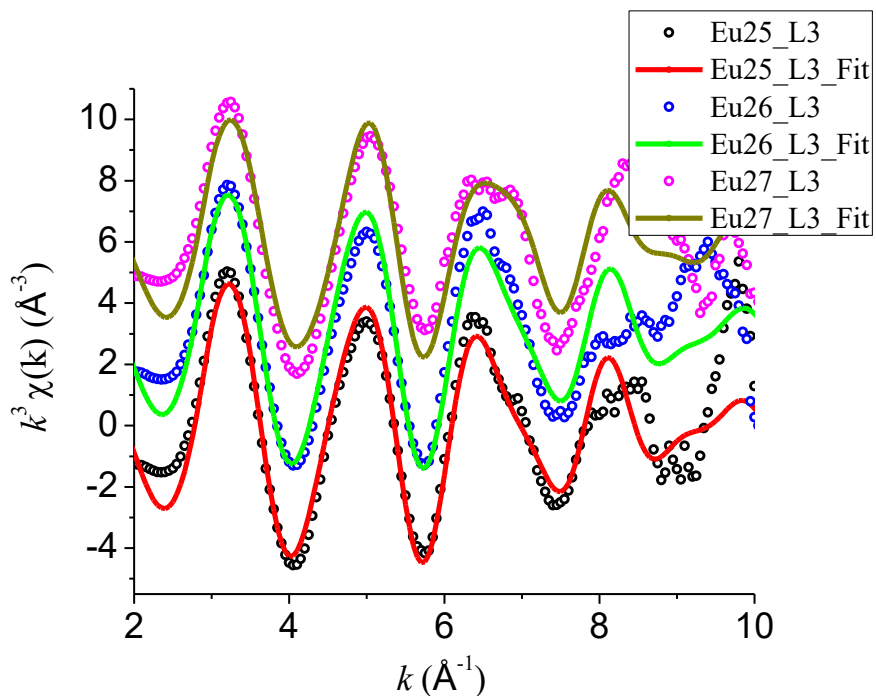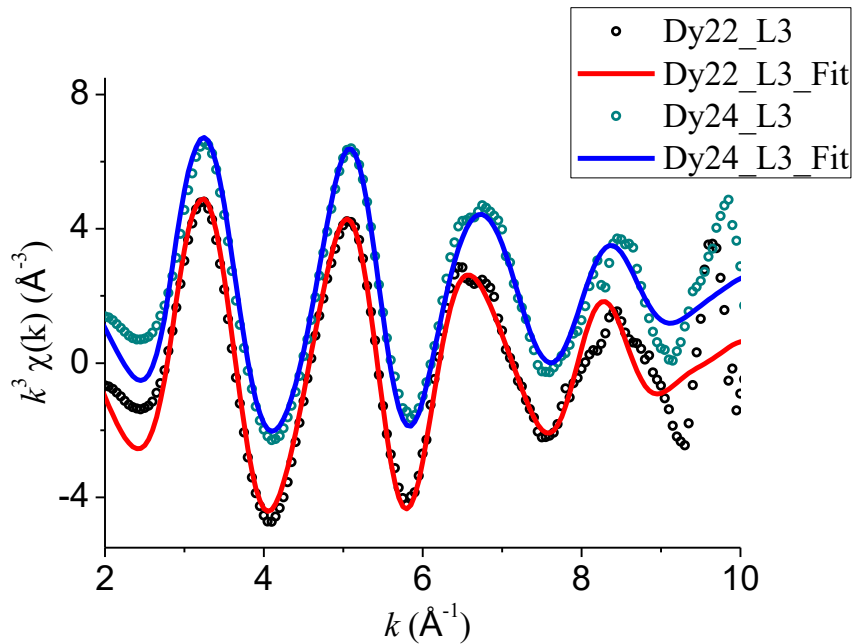
Figure 40. Experimental (dotted line) EXAFS functions $k^3\chi(k)$ and their best fits (solid lines) of dysprosium-doped sodium phosphates with two different compositions measured at L_{III}-edge. The spectra and their fits are vertically separated by 2 Å^{-3} for clarity.
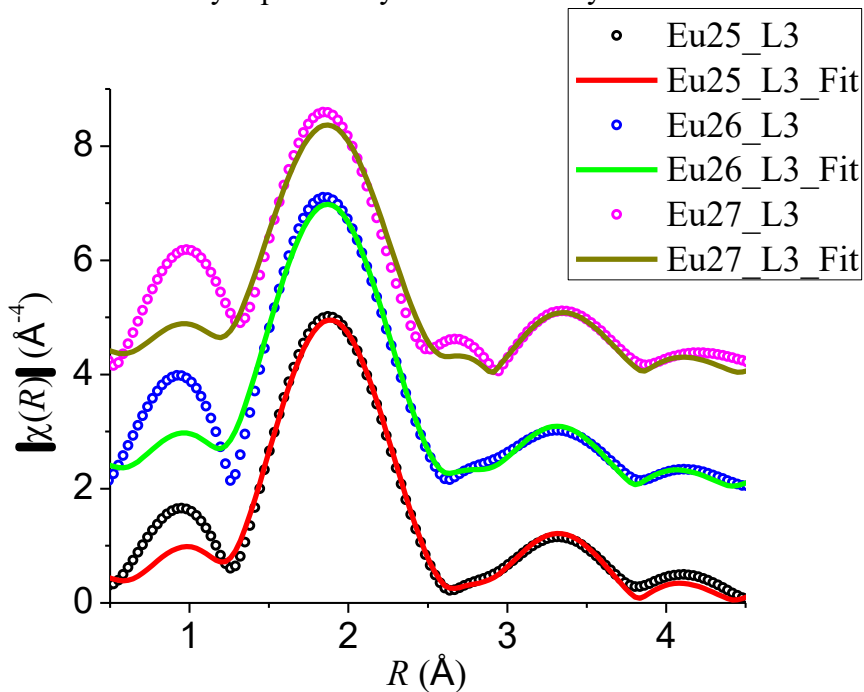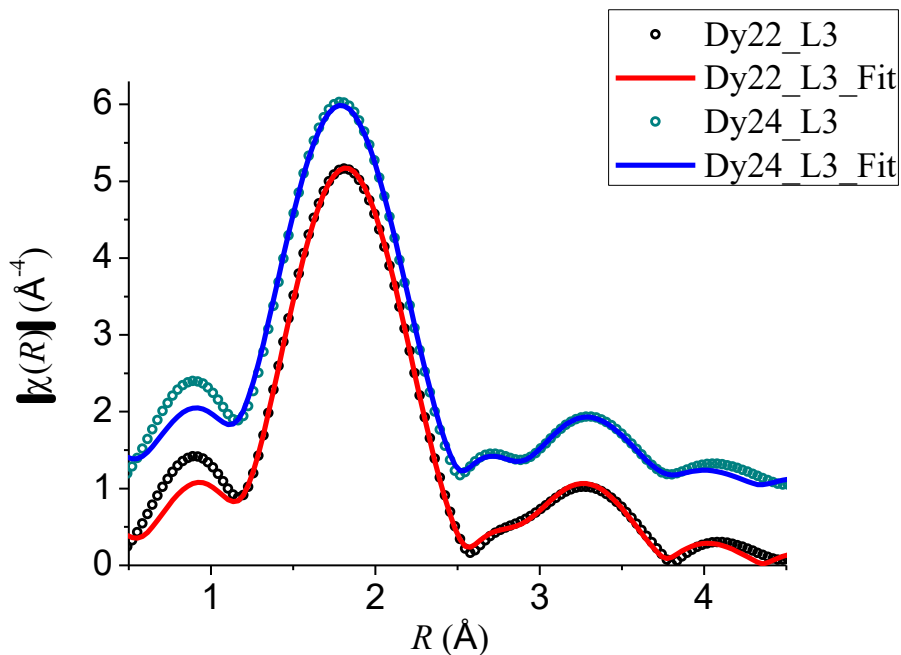

Figure 41. Fourier transforms of experimental (dotted line) EXAFS functions in R-space and their fits (solid lines) measured at L_{III}-edge. The spectra and their fits are vertically separated by 1 Å^{-4} for clarity.

Table 9. Structural parameters obtained for dysprosium-doped sodium phosphates.

Sample	Atomic shell correlation	CN	R (Å)	σ^2 (Å^2)
Dy22_K x = 0.046 y = 0.383	Dy-O(1)	9.7 ± 1.0	2.35 ± 0.03	0.011
Dy22_L$_{III}$ x = 0.046 y = 0.383	Dy-O(1) Dy-P Dy-O(2)	9.8 ± 0.3 2.1 ± 0.7 3.6 ± 2.0	2.32 ± 0.03 3.66 ± 0.01 3.99 ± 0.06	0.014 0.009 0.016
Dy23_K x = 0.076 y = 0.357	Dy-O(1)	9.4 ± 0.7	2.34 ± 0.02	0.011
Dy24_L$_{III}$ x = 0.131 y = 0.310	Dy-O(1) Dy-P Dy-O(2)	9.3 ± 0.2 1.4 ± 0.5 5.2 ± 1.5	2.30 ± 0.02 3.63 ± 0.02 3.99 ± 0.03	0.014 0.009 0.016

Fitting parameters analyzed for dysprosium sodium phosphate glasses studied are summarized in **Table 9**. Common XAFS DWF σ^2 was used for same shell types. Dy-O coordination numbers (CN$_{Dy-O}$) of Dy22 obtained from K-edge and the L$_{III}$-edge data are similar (9.7 and 9.8, respectively). As the Dy$_2$O$_3$ content increases, the value of CN$_{Dy-O}$ decreases to 9.8, 9.4 and 9.3 for Dy22 (x = 0.046), Dy23 (x = 0.076), and Dy24 (x = 0.131), respectively. A first oxygen shell distances tend to decrease from 2.35 Å to 2.30 Å as Dy$_2$O$_3$ content increases. Distance obtained from L$_{III}$-edge data (2.29–2.32 Å) matches better with those obtained from HEXRD data (2.30–2.31 Å) [43], as compared to distances obtained (2.34–2.35 Å) from K-edge data.

L$_{III}$-edge data could be fit with a second phosphorus shell at a Dy-P distance of 3.63–3.66 Å. When compared with crystal structure of DyPO$_4$: four oxygens at about 3.02 Å and four oxygens at about 3.77 Å for crystalline DyPO4 [46], the range of Dy-P distances mentioned above can be attributed to the random nature of the glass network.

The value of CN_{Dy-P} tends to decrease from 2.1 to 1.4 as Dy_2O_3 content increases. A third oxygen shell with a Dy-O(2) distance of 3.99 Å was found with L_{III}-edge data. The values of $CN_{Dy-O(2)}$ were 3.6 for Dy22 and 5.2 for Dy24.

5.1.5 Erbium-doped sodium phosphate glasses

Figure 42 and **43** show $k^3\chi(k)$ and their FTs in the k-range of 3–8 Å^{-1}, respectively, for erbium sodium phosphate glasses studies. **Figure 44** shows experimental spectra (dotted lines) and their fits (solid lines) in k-space, and **Figure 45** shows FTs (dotted lines) and their fits (solid lines) in R-space. They are vertically shifted for comparison between samples.

The crystalline structure of sodium erbium polyphosphate (NaEr(PO$_3$)$_4$) [50] was used to calculate the scattering paths. Available k-range is limited due to low signal-to-noise ratio at high k and, as a result, one-shell model fit using a Er-O single scattering path, was performed. The amplitude reduction factor S_0^2 was set to 1, same as other previous RE samples. XAFS DWF σ^2 was found for the first oxygen shell separately as the number of independent points in the data was enough to fit more unknown parameters for one-shell model fitting.
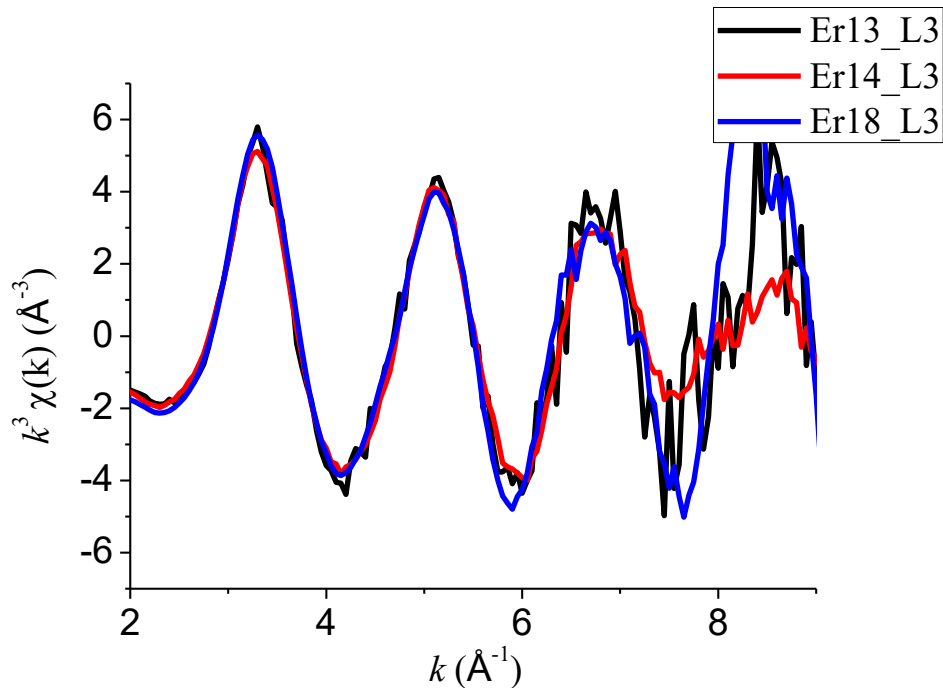
Figure 42. Comparison of measured $k^3\chi(k)$ (Å^{-3}) of erbium-doped sodium phosphates with three different compositions.
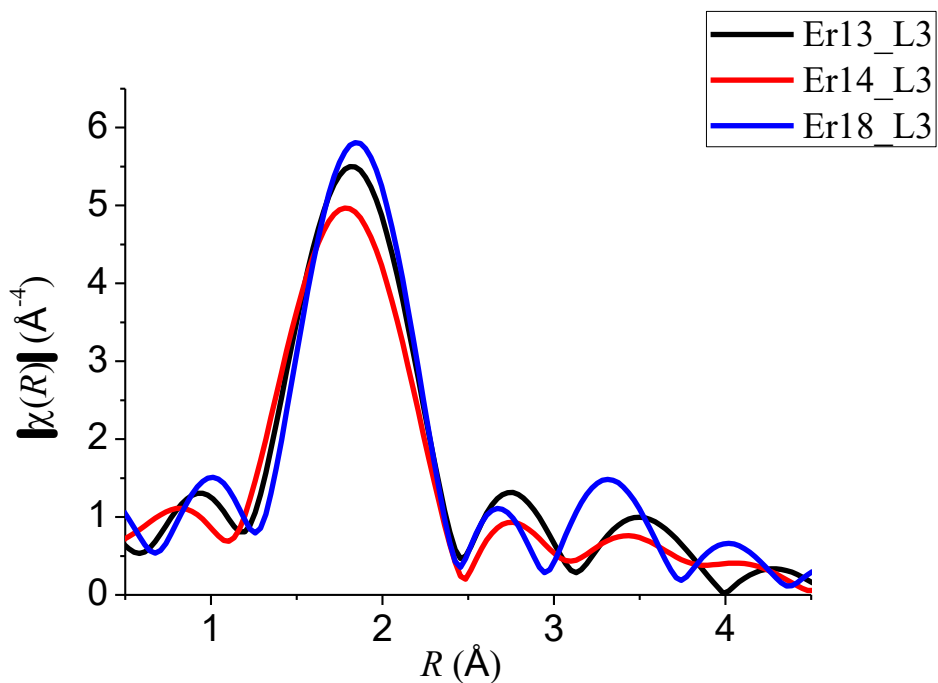
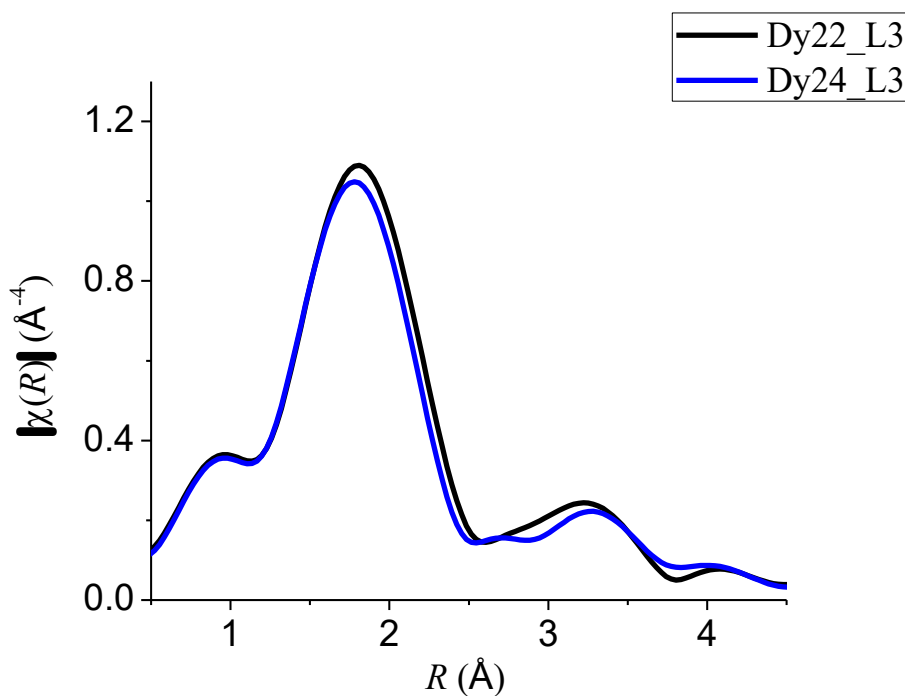**Figure 43.** Comparison of Fourier transforms of $k^3\chi(k)$ (Å^{-3}) functions shown in Figure 42.
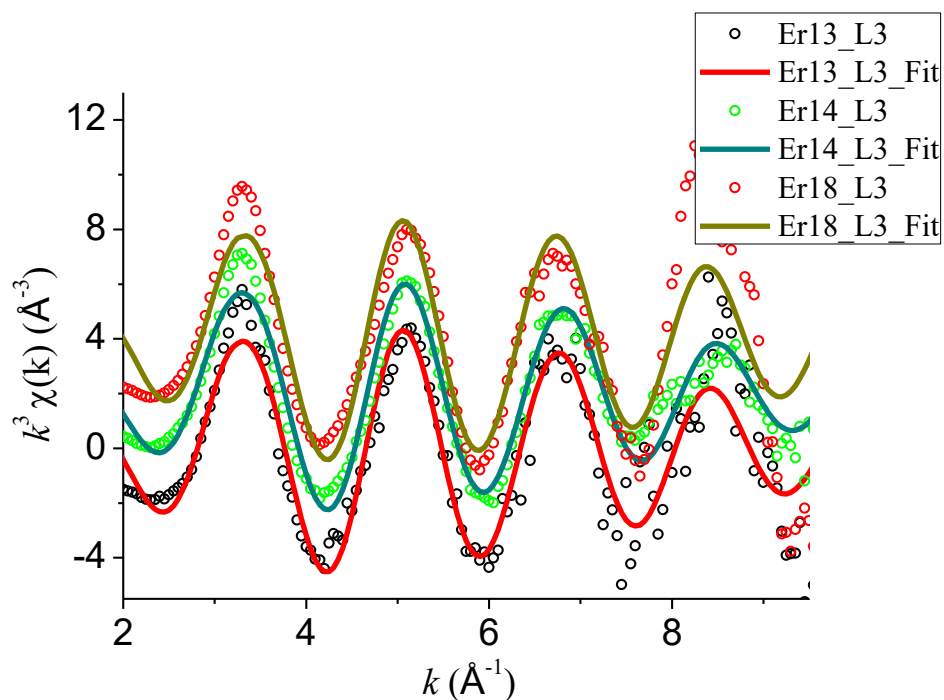
Figure 44. Experimental (Solid line) EXAFS functions and their best fits (dotted line) of erbium-doped sodium phosphates with three different compositions. The spectra and their fits are vertically separated by 2 Å^{-3} for clarity.
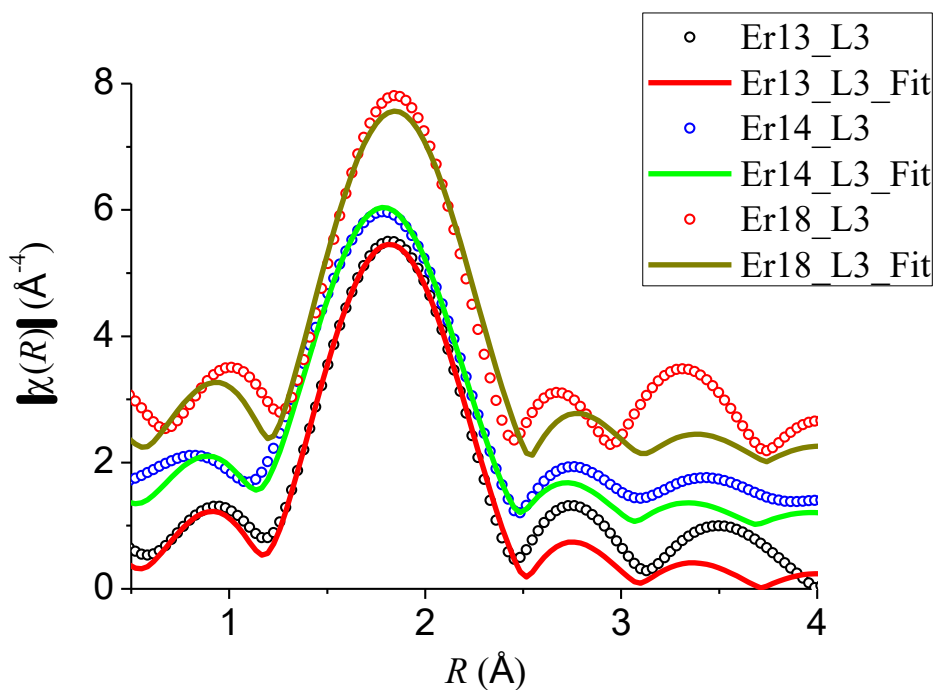
Figure 45. Fourier transforms of experimental (solid lines) EXAFS functions in R-space and their fits (dotted lines). The spectra and their fits are vertically separated by 1 Å^{-4} for clarity.

Table 10. Structural parameters obtained for erbium-doped sodium phosphates.

| Sample	Atomic shell correlation	CN	R (Å)	σ^2 (Å^2)
Er13 $x = 0.005$ $y = 0.395$	Er-O(1)	7.4 ± 2.4	2.28 ± 0.07	0.009
Er14 $x = 0.010$ $y = 0.390$	Er-O(1)	7.3 ± 0.7	2.26 ± 0.02	0.010
Er18 $x = 0.050$ $y = 0.350$	Er-O(1)	6.5 ± 1.6	2.30 ± 0.02	0.007

The structural parameters obtained for three glass samples are given in **Table 10**. A first oxygen shell was found at the distance of 2.26–2.30 Å, which is consistent with EXAFS study for ternary metaphosphates (x = 0.049–0.277) of 2.23–2.30 Å [44]. However, this distance is slightly higher than EXAFS results for binary metaphosphates of 2.22 Å (x = 0.239) [40]. The values of first oxygen coordination number CN_{Er-O} for Er13 was 7.39 and slightly decreased to 7.33 for Er14 (x = 0.010) then decreased to 6.50 for Er18 (0.050) with increasing Er_2O_3 content.

5.1.6 Effect of the composition

The first oxygen coordination number CN_{RE-O} varies between 6.9 and 10.8 depending on the RE element and its concentration. This is higher that the range of 5.7 to 8.1 reported by Anderson *et al* for binary metaphosphates with higher RE content (*x* = 0.187–0.254) [40]. The lower first oxygen coordination CN_{RE-O} values in our samples indicate that the clustering of RE atoms, common at higher RE concentration, appear to be less prevalent and that RE^{3+} cations are coordinated as isolated polyhedra within the

phosphate network [40, 44]. When the number of terminal oxygens (TOs) are lower than the number of RE^{3+} cations, there is not enough TOs to satisfy coordination requirement of isolated RE^{3+} cations [44]. Then modifier cations (RE^{3+} and Na^+) must cluster to share TOs via links, such as RE-O-RE, RE-O-Na, and Na-O-Na [44]. The RE coordination numbers for the first oxygen shell with RE content are plotted in **Figure 46**.

Figure 46 shows the variation of CN_{RE-O} with changing concentration of RE and changing type of RE. **Figure 47** shows a general decrease of RE-O mean distances with increasing RE content for a given type of rare-earth. It also shows some of the effect of the lanthanide contraction on RE-O mean distances [53]. The values of RE-O mean distance are consistent with the values of CN_{RE-O} except erbium series. As the value of CN_{RE-O} increases, the value of RE-O mean distance decreases for praseodymium-, neodymium-, europium-, and dysprosium-doped sodium phosphate glasses. There was no distinct correlation observed for erbium-doped sodium phosphate glasses. This may be due to relatively poor signal-to-noise ratios present in erbium K-edge data. The values of R_{RE-O} obtained tend to decrease from 2.45 Å (for praseodymium-doped sodium phosphate glasses) to 2.28 Å (for europium-doped sodium phosphates glasses) as the atomic number Z increases from 59 for praseodymium to 68 for erbium. Also, for similar RE contents range, praseodymium, neodymium, and erbium samples with RE content around 5 mol% show Z dependence for CN_{RE-O} and R_{RE-O}, due to the larger radii of RE^{3+} ion as Z decreases.
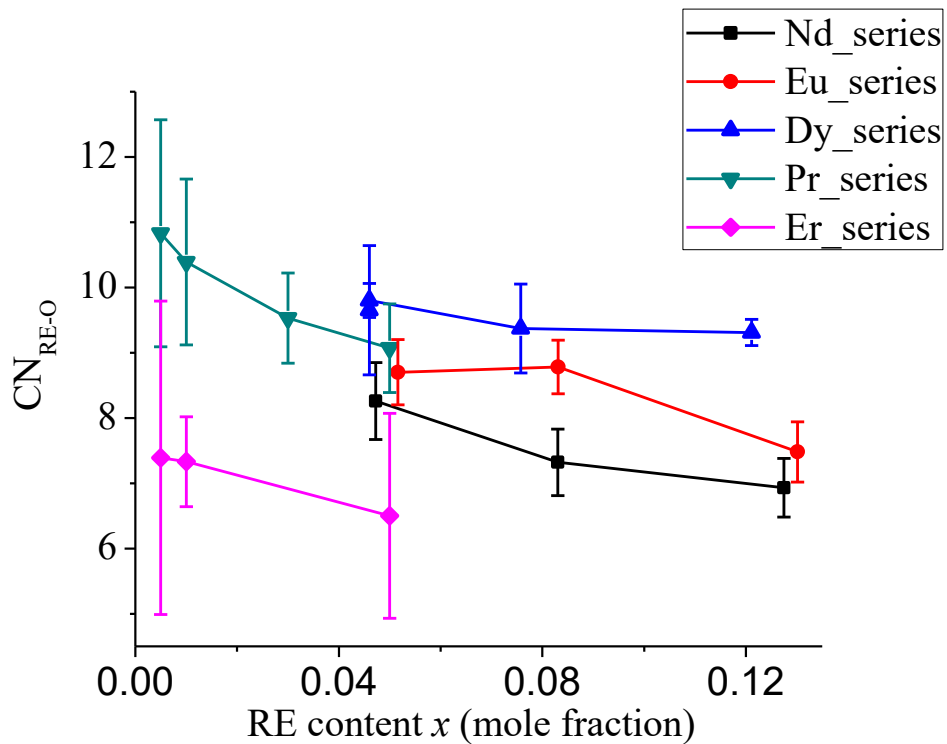
Figure 46. Dependence of the first shell RE-O coordination numbers on the composition.
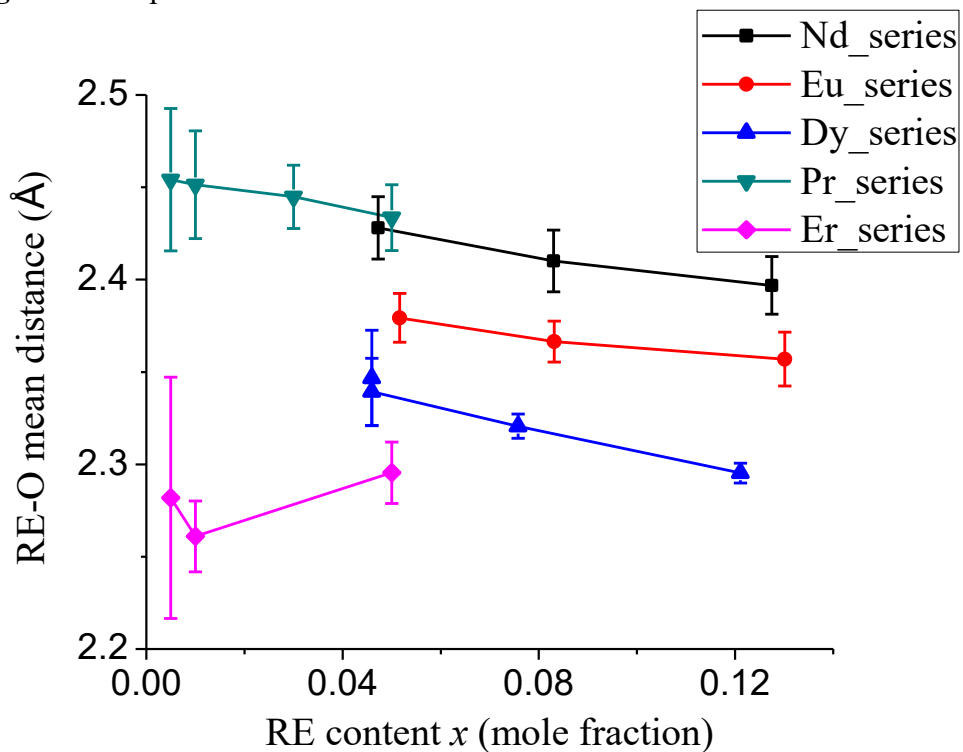
Figure 47. Effect of the composition on the RE-O mean distances.

Even though precautions were taken to minimize exposure to moisture during preparation, handling, and characterization of our samples, it appears that they absorbed some water over time. For a given RE series, the trends discussed previously appear to be more apparent for praseodymium and erbium series than for neodymium, europium, and dysprosium series. Praseodymium and erbium series had been in storage for a much shorter time than neodymium, europium, and dysprosium series prior to XAS measurement. Thus, the possibility of more water absorption for neodymium, europium, and dysprosium samples, needs to be considered. In phosphate glasses, water absorption alters P-O bonds to P-OH bonds (increases Q^2 and decreases Q^3) [52]. The hygroscopic nature of ultraphosphate glasses due to relatively large fraction of P_2O_5 content cannot be ignored even though Na_2O was added as a 'filler' in order to keep the amount of P_2O_5 content around 60–70 mol% and reduce hygroscopic nature of these glasses.

Also, due to low RE content (RE_2O_3) in investigated rare-earth doped sodium phosphate glasses, required thickness for XAS measurement was greater in order to increase the signal-to-noise ratio. There are limitations during the XAS absorber preparation (section 3.5). Current pellet method (using a pelletizer in **Figure 15**) used for the XAS absorber preparation, requires small amount of biobeads (polystyrene beads) added in order to maintain its pellet form during XAS measurement. Also, achievable thickness is limited using this preparation method. Lower RE content in praseodymium and erbium series (0.5–5 mol%) compared to other samples indicates ideal thickness of the XAS absorber is much greater. Since there was more noise introduced at high k region ($k > 8$ Å^{-1}), attempts were made in order to do the three-shell fitting method but were limited to one-shell fitting method.

EXAFS studies indicate that the RE coordination environment depends on the RE content in RE sodium phosphate glasses. As the RE contents decrease, there is an increase in average CN_{RE-O} and R_{RE-O}. These results related with the influence of the composition were expected by Hoppe [51] from his structural model (re-polymerization) and confirmed by XRD and other studies for binary ultraphosphates. This can be understood in terms of the number of TOs available inside the ultraphosphate glasses. For REUP glasses, as RE content decreases, the number of available TOs per RE^{3+} cations increases. Hoppe suggested that structures and properties of ultraphosphate glasses depend on the number of available TOs to coordinate the modifier cations and when there are sufficient TOs available, they tend to bond with each modifier cation [51]. Then modifier cations (RE^{3+} and Na^+) exist as isolated polyhedra within the phosphate network [44, 51]. The break of P-O-P links and conversion of the Q^3 into Q^2 units called 're-polymerization' of the glassy network by Hoppe, explains more TOs from Q^2 and Q^3 polyhedra are around these RE^{3+} cations; Modifier atoms (RE or Na) dominantly linked by RE-O-P bridges or Na-O-P bridges for these samples [51]. Hoppe suggested that system tends to stabilize at the point at which all of TOs occupy RE-O-P links or Na-O-P links for these samples [51].

The fitting model performed does not take into account multiple scattering path contributions and other single scattering shells with lower contributions (low degeneracy or greater path length). Due to amorphous nature of the samples, multiple scattering path contributions is much lower than the case of crystalline samples. The large statistical error is associated with shells at further distance partly due to the amorphous nature of the samples and low RE content (required sample's thickness increases). Therefore, we

expect higher errors related with second and third shell and RE-RE correlations were not found within the short-range order, up to 4 Å. Also, RE-Na single scattering path was not considered during the three-shell fitting, since Na^+ cations are expected to be around the position of second P-shell and their signal's strength is weaker than the second P-shell (lower coordination number expected than P-shell from concentration). The higher errors associated with second and third shell also reflect the decrease in EXAFS resolution at high R and contributions from multiple-scattering processes for amorphous materials [34, 44].

5.2 Zirconium-Doped Lithium Silicate Glasses and Glass-ceramics

The atomic-scale structure around zirconium cations of a series of Zr-doped (3–10 mol% ZrO_2 and atomic ratio Li/Si ≈ 0.8) lithium silicate (ZRLS) glass-ceramics and their parent glasses were studied using Zr K-edge XAS. The dependence on the composition and thermal treatment (used for crystallization in the case of ceramics) was investigated.

5.2.1 XANES of zirconium-doped lithium silicate glasses and glass-ceramics

XANES region, from 30 eV before the edge to about 40 eV after the edge, contains information about the oxidation state of the absorbing ion and its coordination geometry. XANES spectra for ZRLS samples were compared with those of known crystalline compounds. In **Figure 48**, XANES spectra of monoclinic-ZrO_2 (seven-fold coordination), zircon $ZrSiO_4$ (eight-fold coordination), and the samples with different heat treatments (same composition) are compared.
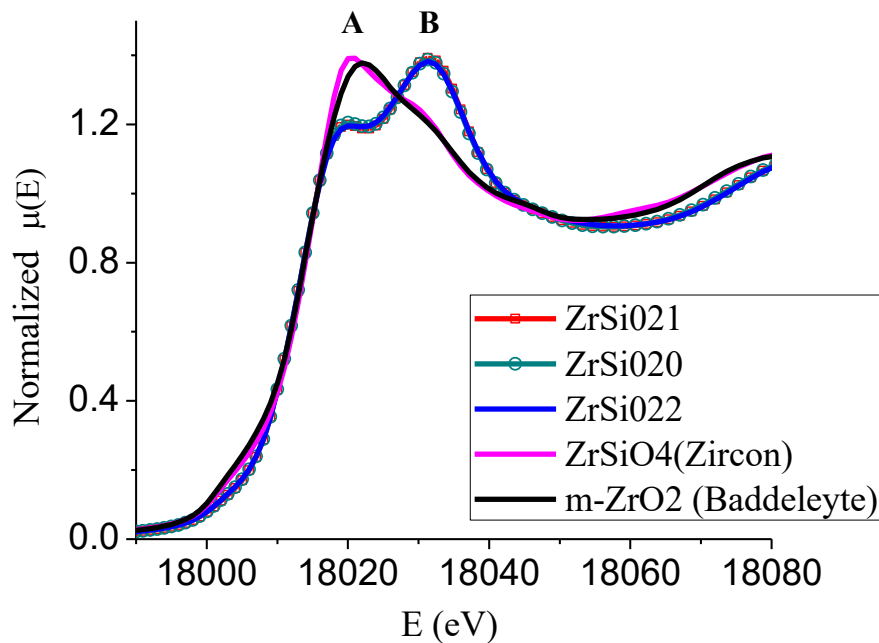
Figure 48. Normalized XANES spectra of monoclinic-ZrO_2, $ZrSiO_4$ (zircon) and samples with different thermal treatments. Note the double-peak (A & B) features of the white line.

XANES spectra in **Figure 48** display differences in the shape and the position of the main absorption edge (the white line) that splits into two components, feature A and feature B, (terms from previous studies [54, 55, 56]) with variable relative intensities depending on Zr coordination. In $ZrSiO_4$, Zr atom is present in eight-fold coordination with oxygen and show two well revolved features of the white line at about 18021 eV (feature A) and at 18030 eV (feature B). These features are shifted toward the higher energy by about 15–19 eV compared some previous studies [54, 55] but match those of others [56, 57].

For $ZrSiO_4$, feature A is prominent while feature B is not well resolved as was the case in some previous studies [54, 55]. In monoclinic-ZrO_2 (baddeleyite), Zr atom is present in seven-fold coordination with oxygen and shows a main feature A located at

around 18020 eV and a low intensity feature B at around 18030 eV. The XANES

spectrum of monoclinic-ZrO_2 is similar to that of $ZrSiO_4$ but feature A of monoclinic-

ZrO_2 is slightly shifted toward high energy compared to zircon $ZrSiO_4$. Four six-fold

coordinated vlasovite ($Na_2ZrSi_4O_{11}$) [55], catapleiite ($Na_2ZrSi_3O_9(H_2O)_2$) [57], and

zektzerite ($LiNaZrSi_6O_{15}$) [57] are characterized by a low-intensity feature A (line B) at

around 18020 eV and a higher intensity feature B (line C) at around 18031 eV [55, 57],

as shown in **Figure 49**.
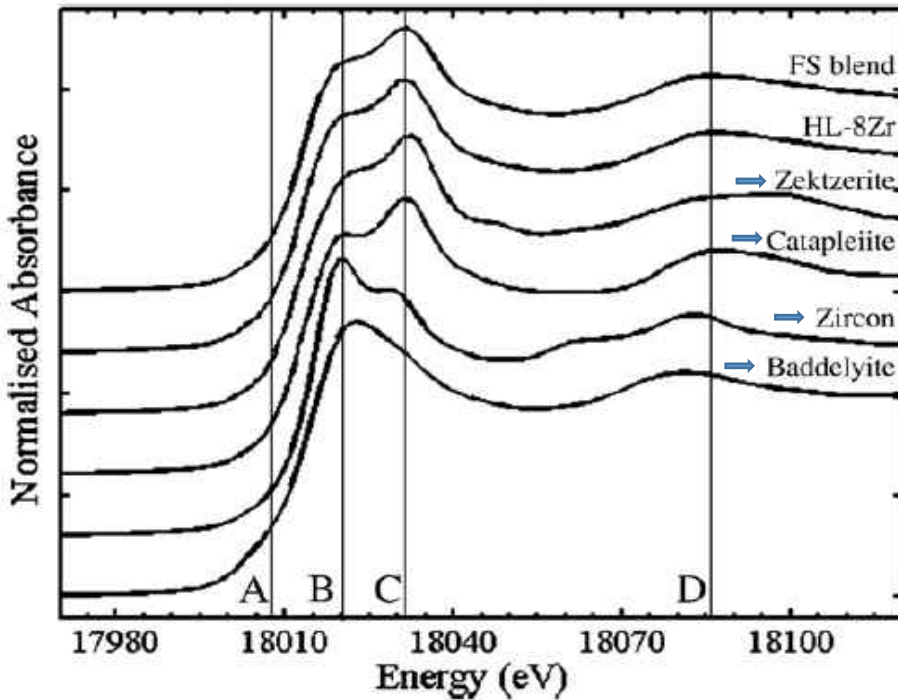
Figure 49. XANES data of four standards and two glass samples by Connelly *et al*. [57]

For ZRLS samples, XANES spectra presented show that the structural

environments of Zr in ZRLS glass and glass-ceramics with high feature B and low feature

A, are very similar to that seen in six-fold coordinated crystal structures of the catapleiite

and the zetzereite [57]. Also, the XANES spectra for ZRLS samples with different heat

treatments, suggest that, Zr^{4+} octahedral sites are relatively regular indicated from the

absence of pre-edge features (a small peak before the main absorption edge around the line A on **Figure 49**) on the XANES spectra as reported in other alkali silicate glasses [55, 57, 58]. The weak pre-edge peak observed in reported tetragonal ZrO_2 (higher symmetry compared to monoclinic-ZrO_2) corresponds to a $1s \rightarrow 4d$ transition when there is some p-d mixing (3d-4p orbitals of suitable symmetry) [56]. Additional shoulder feature (after the main absorption edge, between the line C and D) due to multiple scattering observed in reported tetragonal ZrO_2 was not observed for measured references (monoclinic-ZrO_2 and zircon $ZrSiO_4$) and Zr samples indicating they are less symmetric structures than tetragonal ZrO_2 [56, 57].

5.2.2 Effect of the composition

In order to study the influence on the composition on the local structure, samples with different ZrO_2 content, three $(ZrO_2)_p(Li_2O)_q(SiO_2)_s$ glass samples with ZrO_2 content p ranging from 0.035 to 0.094 were investigated.

Figure 50 shows Zr K-edge k^3-weighted $\chi(k)$ EXAFS measured at 20 K and **Figure 51** shows their FTs. The k-range used was 2.7–9 Å (higher k-range possible because high signal-to-noise ratio) and a Kaiser-Bessel window was used in all fits with a value of dk = 1 Å^{-1} for their FTs. The shape and position of the EXAFS spectra of three glass samples show little change (almost identical) in both k- and R-spaces.

Crystal Structure of zircon $ZrSiO_4$ [60] was used for scattering path calculations. The spectra were fitted using a three-shell model (a first oxygen shell using Zr-O(1) single scattering path, a second silicon shell using Zr-Si single scattering path, and a third oxygen shell using Zr-O(2) single scattering path). The value of S_0^2 was fitted for all

crystalline references (monoclinic-ZrO_2 and zircon $ZrSiO_4$) and set to the value of 1.00 acquired by fitting crystalline standards using a three-shell model. Therefore, $S_0^2 = 1.00$ was applied for the EXAFS analysis and its value is consistent with previous studies of 1.00–1.05 [55, 57]. Measured $\chi(k)$ EXAFS spectra for ZRLS samples with different compositions were fitted simultaneously with equal σ^2 for same shell types. The experimental spectra (dotted lines) and their fits (solid lines) in k-space are shown in **Figure 52** and FTs (dotted lines) and their fits (solid lines) in R-space are shown in **Figure 53**. The spectra and their fits are vertically separated for clarity between samples.
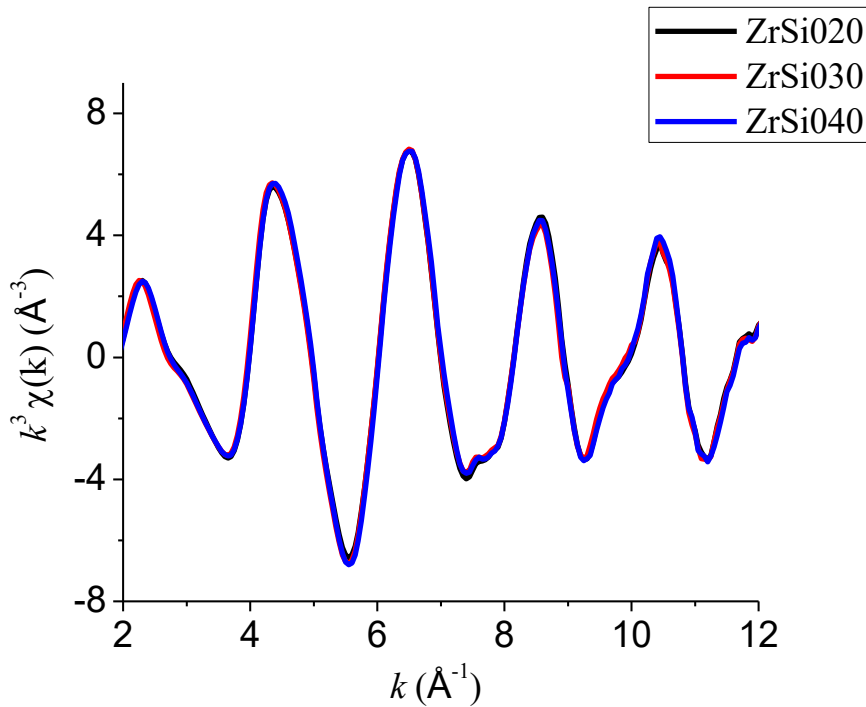
Figure 50. Experimental EXAFS functions $k^3\chi(k)$ (Å^{-3}) for zirconium-doped lithium silicate glasses with different compositions.
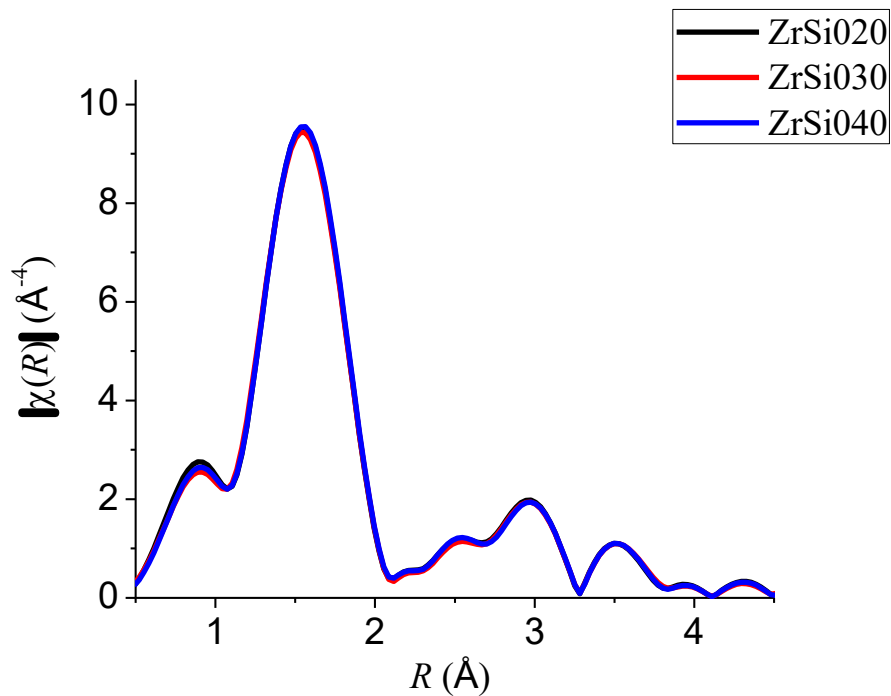
Figure 51. Fourier transforms of $k^3\chi(k)$ (Å^{-3}) of zirconium-doped lithium silicate samples. They show almost no change with different amount of ZrO_2 contents.
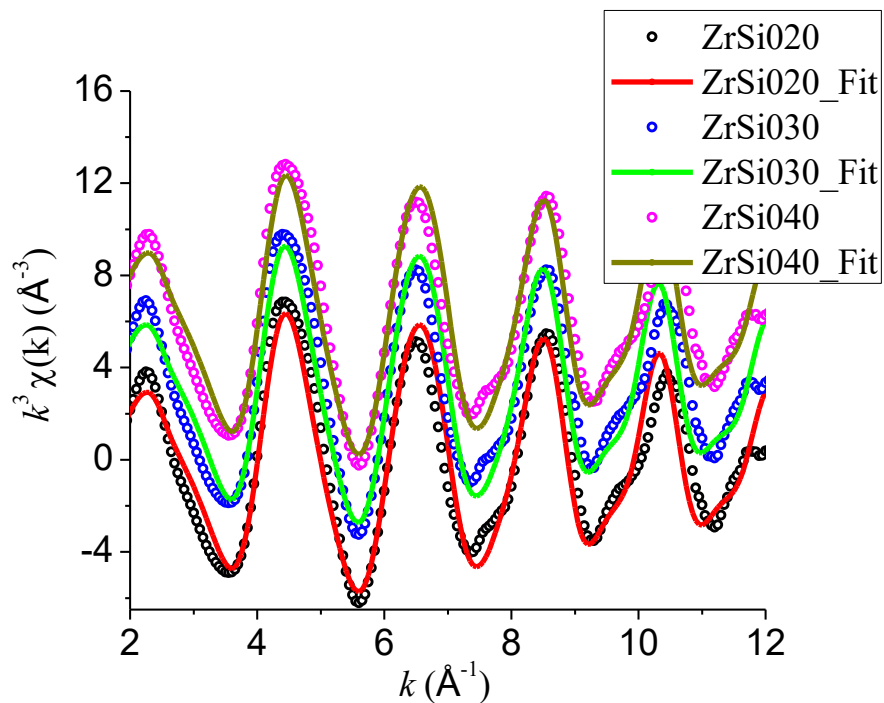
Figure 52. Experimental EXAFS functions $k^3\chi(k)$ (Å^{-3}) plots (dotted line) and their (solid line) fits. The spectra and their fits are vertically separated by 3 Å^{-3} for clarity.
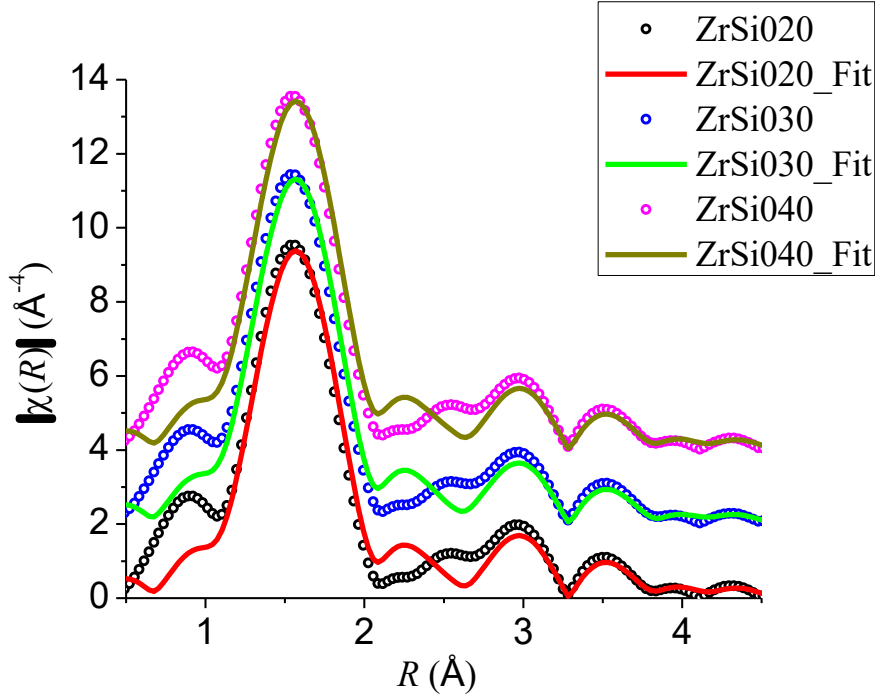
Figure 53. Fourier transforms of experimental EXAFS functions (dotted lines) and their fits (solid lines). The spectra and their fits are vertically separated by 2 Å^{-4} for clarity.

$k^3\chi(k)$ spectra of three samples with different amount of Zr almost overlap each other. FEFF calculations of monoclinic-ZrO_2 (baddeleyite) crystalline reference show CN_{Zr-O} of 7 between 2.05 Å to 2.29 Å [61]. Also, FEFF calculations for zircon $ZrSiO_4$ shows CN_{Zr-O} of 4 at 2.13 Å, CN_{Zr-O} of 4 at 2.27 Å, CN_{Zr-Si} of 2 at 2.99 Å, CN_{Zr-Si} of 4 at 3.63 Å, and CN_{Zr-Zr} of 4 at 3.63 Å. This result suggests an overlap of Zr-Si SS path and Zr-Zr SS path at the same distance with the same degeneracy of 4. For these fitting models, a Zr-Zr SS path was not used since ZrO_2 content is much smaller than Si content and EXAFS spectra show little change with different ZrO_2 content. Thus, the second shell observed in the FTs at around 3 Å (without phase correction of 0.5 Å) suggests mainly Si as the most reasonable second nearest neighbor for ZRLS glasses (Zr-O-Si correlation dominant). However, a small contribution of Zr (Zr-O-Zr) cannot be ruled out.

Mismatch between 2–2.5 Å is expected to be Fourier wiggles from the nearest oxygen peak. Additional zirconium shell below 3.626 Å is not expected from previous FEFF calculations even for crystalline zircon $ZrSiO_4$ and confirmed from compositional independence of these samples. Attempts were made to define additional silicon shell between first oxygen and second silicon shells. But due to limits related available parameters compared to available independent points in EXAFS data, additional shell fitting was not suitable. Lithium shell can be proposed (26.7–28.4 mol%)

Table 11. Structural parameters obtained for ZRLS samples with different compositions. '*p*' represents ZrO_2 content, '*s*' represents SiO_2 content.

Sample	Atomic shell correlation	CN	R (Å)	σ^2 (Å^2)
ZrSi020	Zr-O(1)	6.2 ± 0.5	2.10 ± 0.01	0.004
p = 0.035	Zr-Si and/or Li	3.0 ± 1.9	3.77 ± 0.05	0.005
s = 0.681	Zr-O(2)	7.4 ± 6.1	4.17 ± 0.07	0.007
ZrSi030	Zr-O(1)	6.2 ± 0.5	2.10 ± 0.01	0.004
p = 0.054	Zr-Si and/or Li	3.0 ± 1.9	3.78 ± 0.05	0.005
s = 0.668	Zr-O(2)	7.4 ± 6.1	4.18 ± 0.07	0.007
ZrSi040	Zr-O(1)	6.2 ± 0.5	2.10 ± 0.01	0.004
p = 0.094	Zr-Si and/or Li	2.9 ± 1.9	3.78 ± 0.05	0.005
s = 0.639	Zr-O(2)	7.3 ± 6.1	4.17 ± 0.07	0.007

Structural parameters determined by EXAFS are presented in **Table 11**. A first oxygen shell was found at the average distance of 2.10 Å with the CN_{Zr-O} of 6.2 which is a very close to those of zektzerite (2.08 Å) [57, 62] and aluminoborosilicate nuclear glass (2.09 Å) [63]. Also, fitted disorder factor (σ^2) was about 0.004 Å^2 for the first oxygen shell indicating that structural disorder is very low for these glasses (close to that of crystalline references). This is quite likely because the thermal disorder factor was minimized because measurements were done at 20 K. These results indicate that Zr is

six-fold coordinated to oxygen with a small radial disorder σ^2 (structural disorder dominant and thermal disorder minimized).

A second Si-shell was fitted at the average distance of 3.77–3.78 Å which is higher than the 3.59 Å and 3.44 Å Zr-Si bond lengths of crystalline catapleiite and crystalline zektzerite, respectively [57]. The CN_{Zr-Si} is approximately 3 which is only half of that observed (6) for catapleiite and zektzerite. This difference is expected because of the disorder in glasses.

The second shell CN_{Zr-Si} extracted from EXAFS analysis (3) is quite low and shows some misfits around 2.5 Å correspond actual distance of 3 Å (after phase correction). From FEFF calculations of zektzerite [62], there are contributions from two lithium atoms at 2.97 Å and a sodium atom at 3.39 Å. There are also silicon atoms 3.45–3.50 Å with degeneracy of six (four silicon atoms at around 3.45 Å and two silicon atoms at around 3.50 Å) further away than glass modifier atoms (Li, Na) from zirconium absorber for zektzerite. Si was considered as the most plausible second nearest neighbor, but contribution of lithium atoms cannot be ruled out from FEFF calculations of zektzerite. Attempts to fit an additional shell related with lithium atoms was not successful due to phase difference (EXAFS signal canceling out each other when they are close to each other due to phase difference) since there is strong Si-shell contributions around 3.77 Å expected after Li-shell's position of 2.97 Å and strong first O-shell contribution close by at 2.10 Å. Expected lithium contribution is around 3 Å (around 2.5 Å in FTed EXAFS functions $\chi(R)$) but due to existence of the strong first O-shell and the Si-shell nearby, additional Li-shell fitting was limited.

Also, attempts to fit the second shell with Zr atoms were unsuccessful and from the very low composition dependence, the existence of Zr-O-Zr links were precluded. Also, from the FEFF calculations for zektzerite, Zr-Zr single scattering path was not identified up to 4.64 Å. Best reasonable results were obtained by considering Si as the second shell (Zr-O-Si linkages). From the almost identical EXAFS spectra with different amount of ZrO_2 content, we can expect no Zr within the range of interest (< 4.5 Å). There might be polycrystalline phases around the Zr atom with small amount of contribution of Zr atoms below 4 Å while most contributions are from Si atoms around 3.77–3.78 Å.

There are larger uncertainties on the structural parameters calculated for the second Si-shell and third O-shell due to the limited k-range of the data and the difficulty of constraining number elements, such as Si and Li to the EXAFS functions [55, 58]. For our measured EXAFS spectra, using greater k-range will introduce more contributions from multiple scattering paths. Also, generally EXAFS spectra for amorphous materials, contributions from the nearest dominant peak (usually the nearest O-shell) is much greater than other shells.

Within the resolution of our EXAFS analysis, the number of second neighbors in our ZRLS glasses, similar to findings for simplified aluminoborosilicate nuclear glass by Caurant *et al*. [63]. The results also suggest Zr is coordinated to six oxygen atoms from SiO_4 tetrahedral units. Also, the presence of additional Li atoms in the second coordination shell, might be slightly underestimated since ZrO_6 octahedra are expected to preferentially charge compensated by Li^+ cations, linking the ZrO_6 octahedral and SiO_4 tetrahedral units. Thus ZrO_2 is expected to modify Na+ cations distribution within the glassy network. A reasonable structure would require that two of the oxygens bonded to

the central Zr atoms, and they are bonded to two Si atoms but also bonded to one or two Li atoms, in a geometry similar to that found in zektzerite [55, 62].

Structural parameters in **Table 11** strongly suggests that Zr^{4+} cation coordination environments are unchanged when ZrO_2 content increases. The EXAFS and the XANES results together imply that the coordination environment of Zr^{4+} cations in these glasses has a high degree of order as compared to an average glass and that the structural parameters of this environment is nearly independent of ZrO_2 content. Also, Zr^{4+} cation coordination environments are dominated by Zr-O-Si correlations as seen in zirconia-silica xerogels with p ≈ 0.1 [34]. [similar results observed from [63] with $ZrO_2 = 1.90$–5.69 mol% and $SiO_2 ≈ 60$ mol%]

5.2.3 Effect of the thermal treatments

In order to study the effect of the thermal treatments (crystallization process) on the Zr coordination environment, two series of samples with different thermal treatments were investigated. Two samples, ZrSi021 and ZrSi031 were obtained by annealing their parent glasses, ZrSi020 and ZrSi030, respectively, at 520 °C for 10 min for nucleation. ZrSi022 and ZrSi032 were obtained by first taking the parent glasses first through the above mentioned nucleating process and then annealing at 720 °C for 20 min for crystal growth. Consequently, compositions of ZrSi020, ZrSi021, and ZrSi022 are identical. So are the compositions of ZrSi030, ZrSi031, and ZrSi032. Six samples (two glass samples, two nucleated samples, and two crystallized (ceramic) samples) were investigated by Zr K-edge EXAFS spectroscopy at 20 K.

Figure 54 and **56** show EXAFS functions $k^3\chi(k)$ of ZRLS glasses before thermal treatments and ZRLS glass-ceramics after thermal treatments (nucleation and crystal growth). **Figure 55** and **57** show corresponding FTs for the samples. Their spectra are similar with only slight differences related with the first oxygen peaks around 1.5 Å without the phase correction (about 0.5 Å). EXAFS spectra for both series, show similar behaviors after the thermal treatments. After the nucleation process, the first oxygen peaks tend to rise and then after the additional crystal growth process they tend to fall slightly which is different from previous results (Chapter 5.2.1) with different compositions.

Figure 58 and **60** show experimental spectra (dotted lines) and their fits (solid lines) in *k*-space, and **Figure 59** and **61** shows FTs (dotted lines) and their fits (solid lines) in *R*-space. Same fitting methods from previous EXAFS analysis for the composition change were used. Two series with same composition (different thermal treatments) were fitted simultaneously with σ^2 set to equal for same shell types.
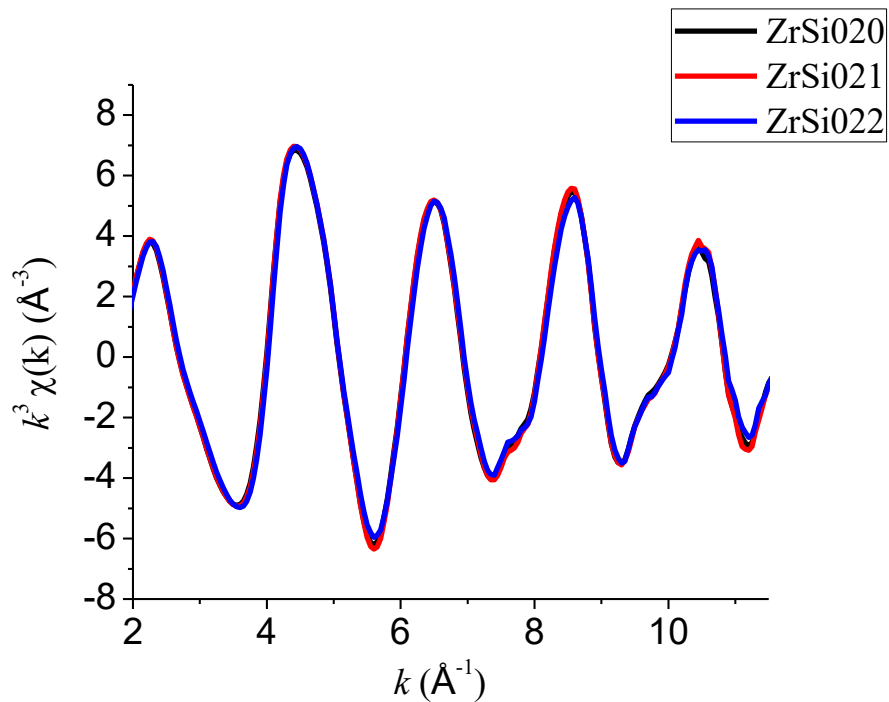
Figure 54. Experimental EXAFS functions $k^3\chi(k)$ ($Å^{-3}$) of zirconium-doped lithium silicate samples (p = 0.035, s = 0.681) with different thermal treatments.
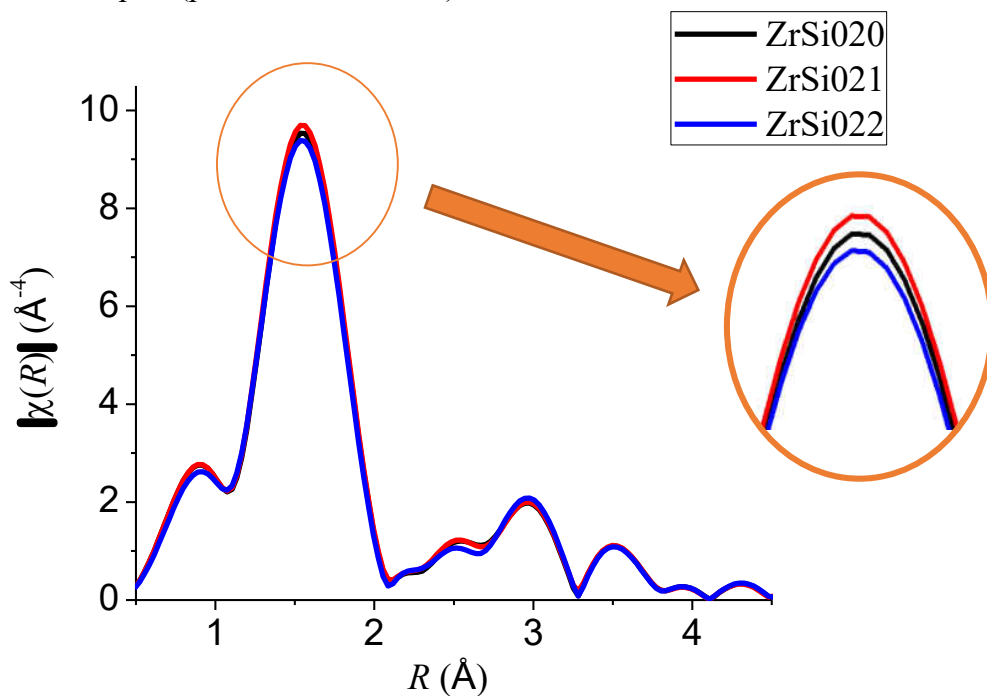
Figure 55. Comparison of Fourier transforms of $k^3\chi(k)$ ($Å^{-3}$) functions of zirconium-doped lithium silicate samples (p = 0.035, s = 0.681) with different thermal treatments shown in Figure 54.
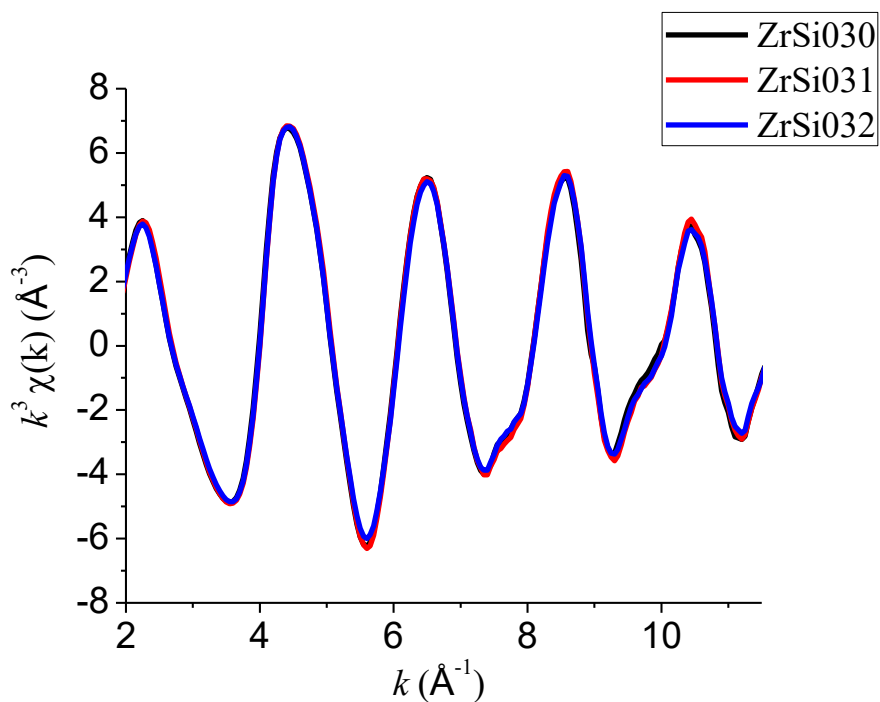
Figure 56. Experimental EXAFS functions $k^3\chi(k)$ (Å^{-3}) of zirconium-doped lithium silicate samples (p = 0.054, s = 0.668) with different thermal treatments.
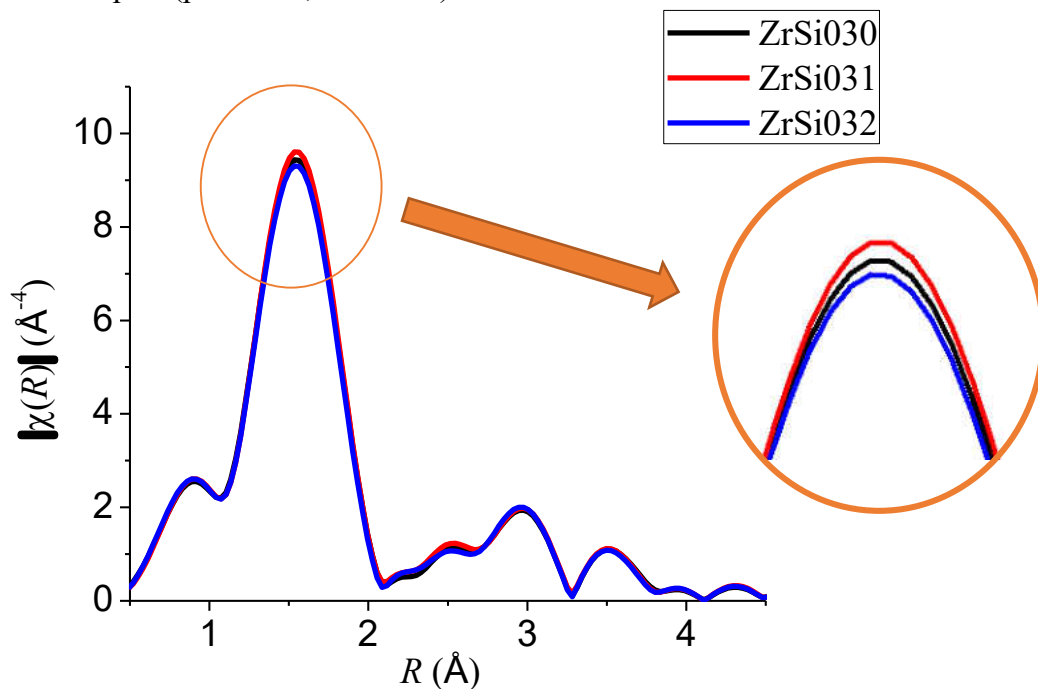
Figure 57. Comparison of Fourier transforms of $k^3\chi(k)$ (Å^{-3}) functions of zirconium-doped lithium silicate samples (p = 0.054, s = 0.668) with different heat treatments shown in Figure 56.
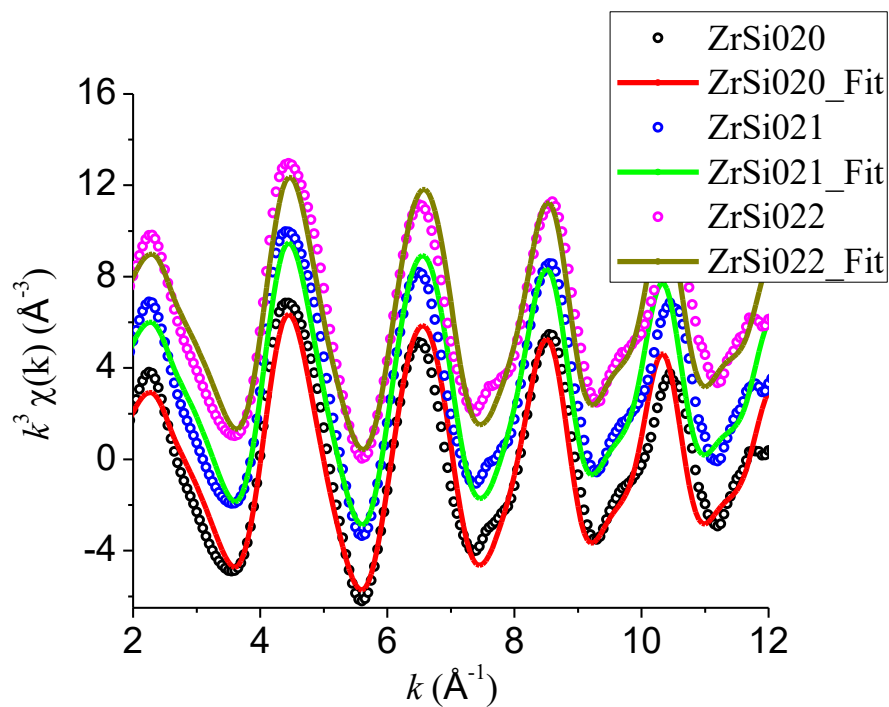
Figure 58. Experimental (dotted line) EXAFS functions $k^3\chi(k)$ (Å^{-3}) and their best fits (solid line) of zirconium-doped lithium silicate samples (p = 0.035, s = 0.681) with different thermal treatments. The spectra and their fits are vertically separated by 3 Å^{-3} for clarity.
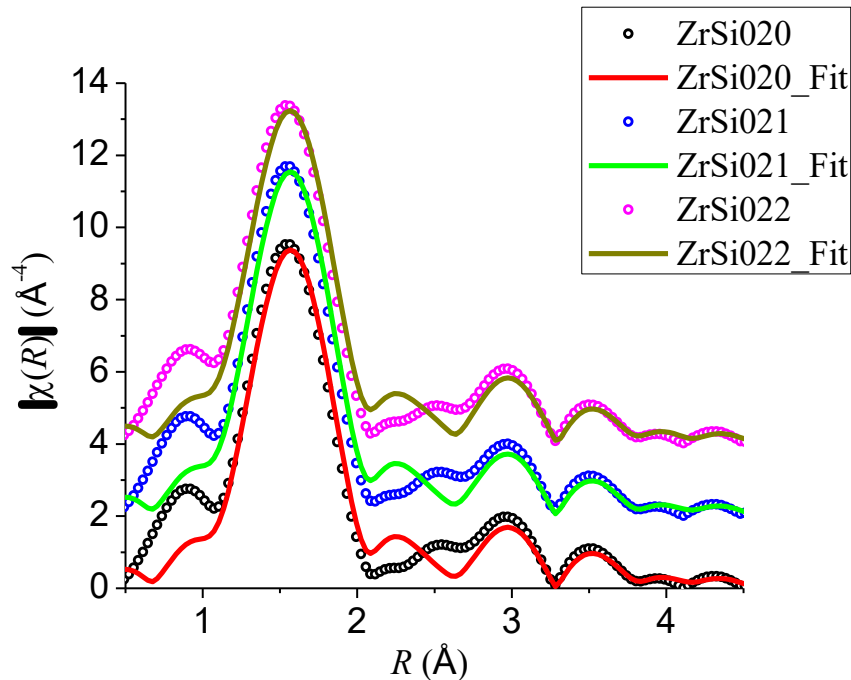
Figure 59. Fourier transforms of experimental (dotted lines) EXAFS functions in *R*-space and their fits (solid line) of zirconium-doped lithium silicate samples (p = 0.035, s = 0.681). The spectra and their fits are vertically separated by 2 Å^{-4} for clarity.
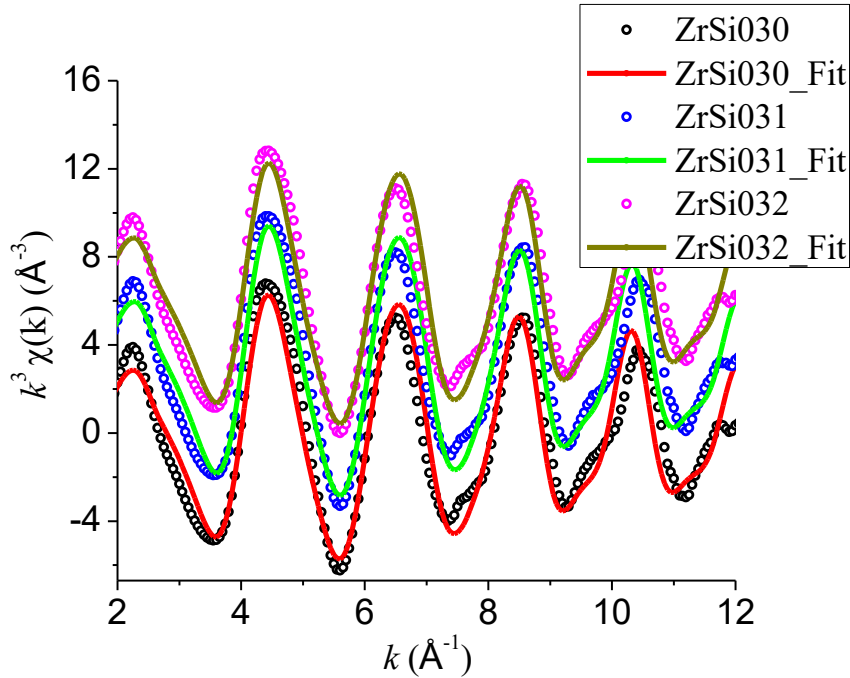
Figure 60. Experimental (dotted line) EXAFS functions $k^3\chi(k)$ ($Å^{-3}$) and their best fits (solid line) of zirconium-doped lithium silicate samples (p = 0.054, s = 0.668) with different thermal treatments. The spectra and their fits are vertically separated by 3 $Å^{-3}$ for clarity.
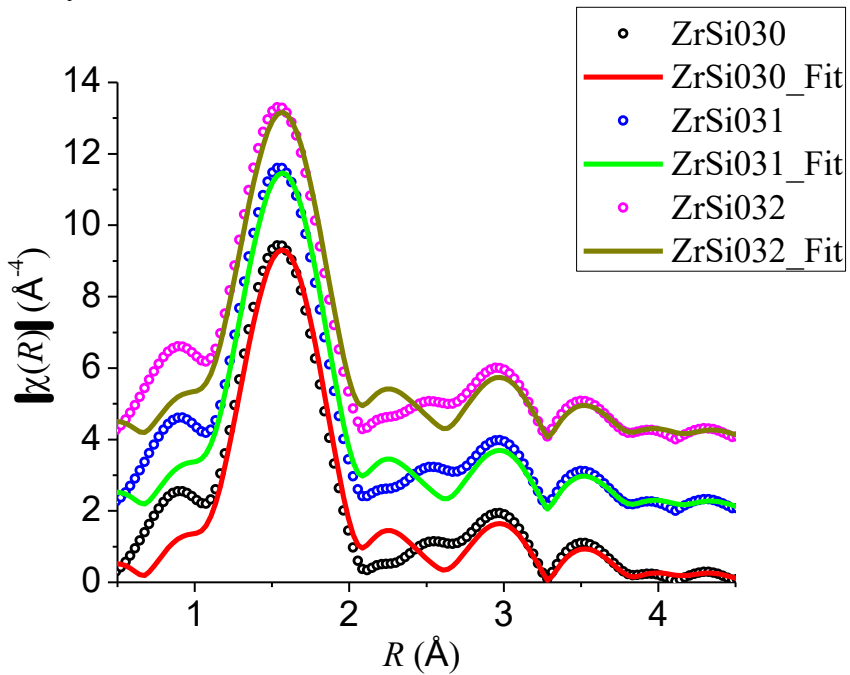
Figure 61. Fourier transforms of experimental (dotted lines) EXAFS functions in *R*-space and their fits (solid line) of zirconium-doped lithium silicate samples (p = 0.054, s = 0.668) with different thermal treatments. The spectra and their fits are vertically separated by 2 $Å^{-4}$ for clarity.

Table 12. Structural parameters obtained for ZRLS samples with different thermal treatments. σ^2 were set to equal for same shell types. 'p' represents ZrO_2 content and 's' represents SiO_2 content.

Sample	Atomic shell correlation	CN	R (Å)	σ^2 (Å^2)
ZrSi020	Zr-O(1)	6.2 ± 0.5	2.10 ± 0.01	0.004
p = 0.035	Zr-Si and/or Li	3.0 ± 1.9	3.77 ± 0.05	0.005
s = 0.681	Zr-O(2)	7.4 ± 6.1	4.17 ± 0.07	0.007
ZrSi021	Zr-O(1)	6.3 ± 0.6	2.10 ± 0.01	0.004
p = 0.035	Zr-Si and/or Li	3.1 ± 2.0	3.78 ± 0.05	0.005
s = 0.681	Zr-O(2)	7.8 ± 6.3	4.17 ± 0.07	0.007
ZrSi022	Zr-O(1)	6.1 ± 0.5	2.10 ± 0.01	0.004
p = 0.035	Zr-Si and/or Li	3.3 ± 1.9	3.77 ± 0.05	0.005
s = 0.681	Zr-O(2)	7.6 ± 5.9	4.16 ± 0.07	0.007
ZrSi030	Zr-O(1)	6.2 ± 0.5	2.10 ± 0.01	0.004
p = 0.054	Zr-Si and/or Li	3.0 ± 1.9	3.78 ± 0.05	0.005
s = 0.668	Zr-O(2)	7.4 ± 6.1	4.18 ± 0.07	0.007
ZrSi031	Zr-O(1)	6.3 ± 0.5	2.10 ± 0.01	0.004
p = 0.054	Zr-Si and/or Li	3.0 ± 1.9	3.78 ± 0.05	0.005
s = 0.668	Zr-O(2)	7.7 ± 6.1	4.17 ± 0.07	0.007
ZrSi032	Zr-O(1)	6.1 ± 0.5	2.10 ± 0.01	0.004
p = 0.054	Zr-Si and/or Li	3.2 ± 1.9	3.77 ± 0.05	0.005
s = 0.668	Zr-O(2)	7.5 ± 6.1	4.17 ± 0.07	0.007

The structural parameters determined by EXAFS are in **Table 12.** A first oxygen shell was found at the average distance of 2.10 Å with the coordination number CN_{Zr-O} between 6.1 and 6.3. After the nucleation process, CN_{Zr-O} tends to increase from 6.2 to 6.3 for ZrSi021 and ZrSi031. The Zr-O mean distance and the disorder factor σ^2 remain the same. After the additional crystal growth process, CN_{Zr-O} tend to decrease from 6.3 to 6.1 for ZrSi022 and ZrSi032, respectively, while other parameters remain the same. (very small reduction observed less than about 0.004 Å for R_{Zr-O}).

A second silicon shell was fitted at the average distance of 3.77 Å and the coordination number of CN_{Zr-Si} was from 3.0 with little changes observed after the nucleation process. The CN_{Zr-Si} slightly increases from 3.0 to 3.3 and from 3.0 to 3.2 for ZrSi022 and ZrSi032, respectively, after the thermal treatments. But little changes were observed for other parameters (R_{Zr-Si} and σ^2). The evidence for contribution of Zr atoms with Zr-Zr distance below 4 Å was not observed. Also, the contribution of Li atoms around 2.97 Å cannot be ruled out.

The results suggest that the structural environment around Zr is six-fold coordination dominant and they were formed around Zr during the glass formation. Small changes related with the Zr-O coordination number were observed after nucleation and crystal grow processes indicating thermal treatments slightly alter the local structure around Zr. From EXAFS results, the influence of thermal treatments is higher than the influence of the composition on the local structure around Zr. Also, the formation of a polycrystalline phases similar to the orthorhombic zektzerite is more dominant for ZRLS glass-ceramics as observed from the reduction of CN_{Zr-Si} from 6.19–6.20 to 6.06–6.07 for ZrSi022 and ZrSi032, respectively. Thus, these results suggest that dominant ZrO_6 species are linked to SiO_4 tetrahedral units within silicate glass and glass-ceramics, and the structure is similar to the environment the zektzerite [57, 62].

5.3 Zirconium-Doped Lithium Borate Glasses

5.3.1 Effect of the composition

In order to study the influence of the composition on the local environment of Zr in the Zr-doped lithium borate (ZRLB) glasses, $(ZrO_2)_p(Li_2O)_q(Al_2O_3)_r(B_2O_3)_{1-p-q-r}$ glass

samples with different ZrO_2 contents (2–5.7 mol% of ZrO_2 and atomic ratio Li/B ≈ 0.25–0.18) were investigated by Zr K-edge EXAFS spectroscopy at 20 K.

5.3.1.1 XANES of zirconium-doped lithium borate glasses

The XANES spectra of the monoclinic-ZrO_2, zircon $ZrSiO_4$, and ZRLB glasses with different composition are shown in **Figure 62**. **Figure 63** compares two crystalline reference samples (monoclinic-ZrO_2 and zircon $ZrSiO_4$), ZRLS (ZrSi020) glass, and ZRLB glass (ZrB050).
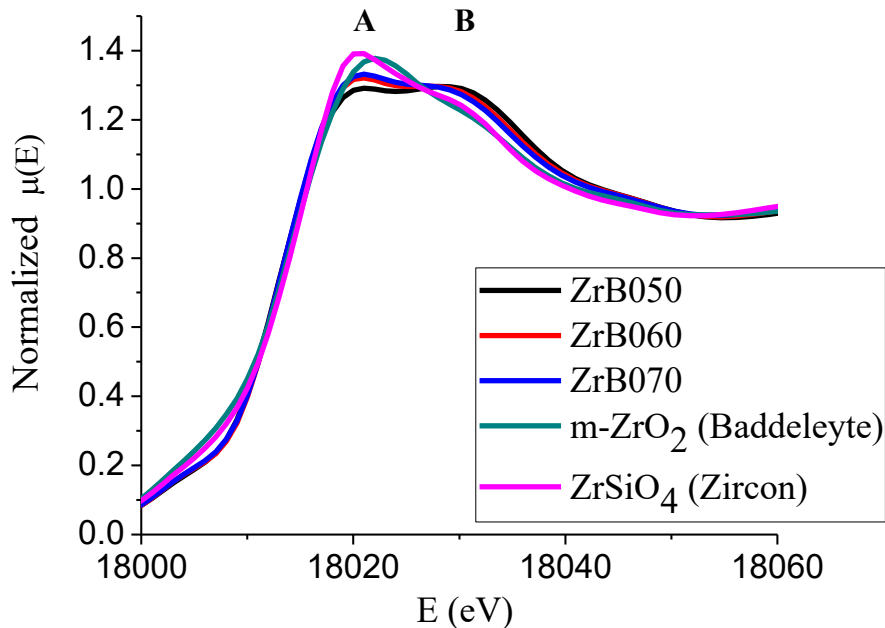
Figure 62. XANES spectra of monoclinic-ZrO_2 (seven-fold coordination), zircon $ZrSiO_4$ (eight-fold coordination), and zirconium-doped lithium borate glasses with different compositions.
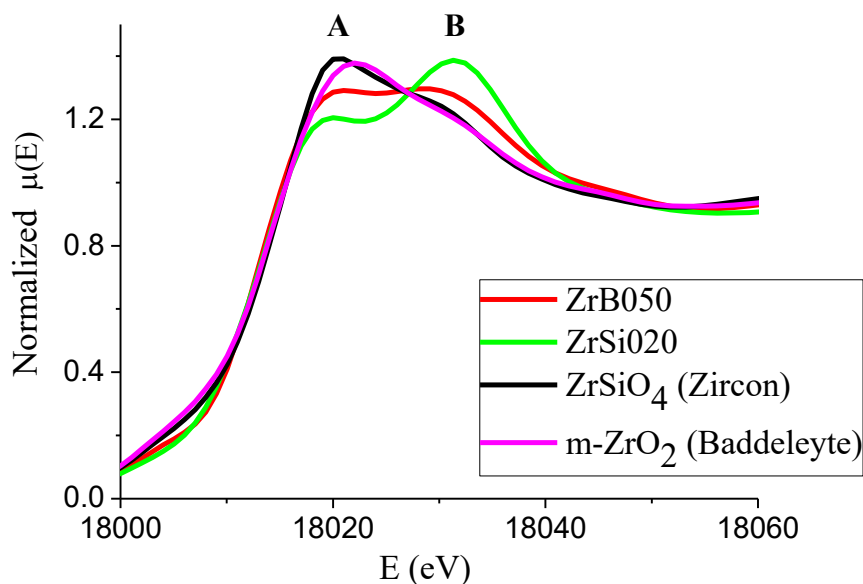
Figure 63. XANES spectra of two crystalline reference samples, a zirconium-doped lithium borate glass (p = 0.020), and a zirconium-doped lithium silicate glass (p = 0.035).

The XANES spectra in **Figure 62** show that feature A of ZRLB glasses is weaker (less intense) than that of monoclinic-ZrO_2 and feature B is also weaker than that of ZRLS glasses, as shown in **Figure 63**. For ZRLB glasses, feature A is comparable with feature B and feature A rises and feature B falls with increasing ZrO_2 content, as shown in **Figure 62**. **Figure 63** shows the main absorption peak being asymmetric with a higher peak on the left-hand side (feature A > feature B) for monoclinic-ZrO_2 (seven-fold coordination) and the main absorption peak being asymmetric with a higher peak on the right-hand side (feature B > feature A) for ZRLS glass (six-fold coordination dominant). This observation suggests that the first oxygen coordination of ZRLB glasses is between the monoclinic-ZrO_2 and ZRLS glass which implies the presence of two different Zr environments (oxidation states) in ZRLB glasses, *i.e* mixed structure of six- and seven-fold coordination. These observations provide a basis for describing the coordination environment around Zr for EXAFS analysis.

103

5.3.1.2 EXAFS of zirconium-doped lithium borate glasses

Figure 64 shows zirconium K-edge EXAFS spectra and **Figure 65** shows the corresponding FTs of the k^3-weighted $\chi(k)$ EXAFS oscillations for the ZRLB glasses with different compositions. Major peaks around 1.6 Å shows the nearest Zr-O coordination and the position those peaks tends to shift toward higher R and the height decreases with increasing ZrO_2 content.

Crystal structure of ternary zirconium borate, high-pressure phase $\beta\text{-}ZrB_2O_5$ [36], was used for FEFF calculations. The spectra were fitted using a three-shell model (a first oxygen shell using Zr-O(1) SS path, a second borate shell using Zr-B SS path, and a third oxygen shell using Zr-O(2) SS path). The value of S_0^2 was determined to be 1.00 acquired by fitting crystalline standards using a three-shell model from previous. The k-range used was 2.7–8 Å which is narrower than the k-range of 2.7–9 Å for ZRLS glasses due to noise introduced at higher k (k > 8). A Kaiser-Bessel window was used for FTs and they were fitted simultaneously with equal σ^2 for same shell types. The experimental spectra (dotted lines) and their fits (solid lines) in k-space are shown in **Figure 66** and FTs (dotted lines) and their fits (solid lines) in R-space are shown in **Figure 67**. The spectra and their fits are vertically separated for clarity.
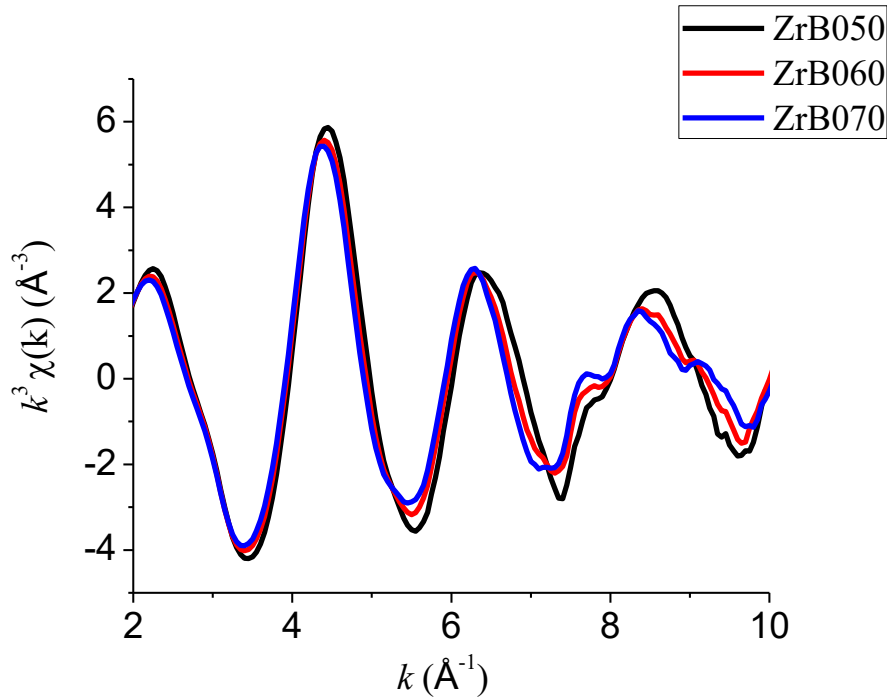
Figure 64. Experimental EXAFS functions $k^3\chi(k)$ (Å^{-3}) of zirconium-doped lithium borate glasses with three different compositions.
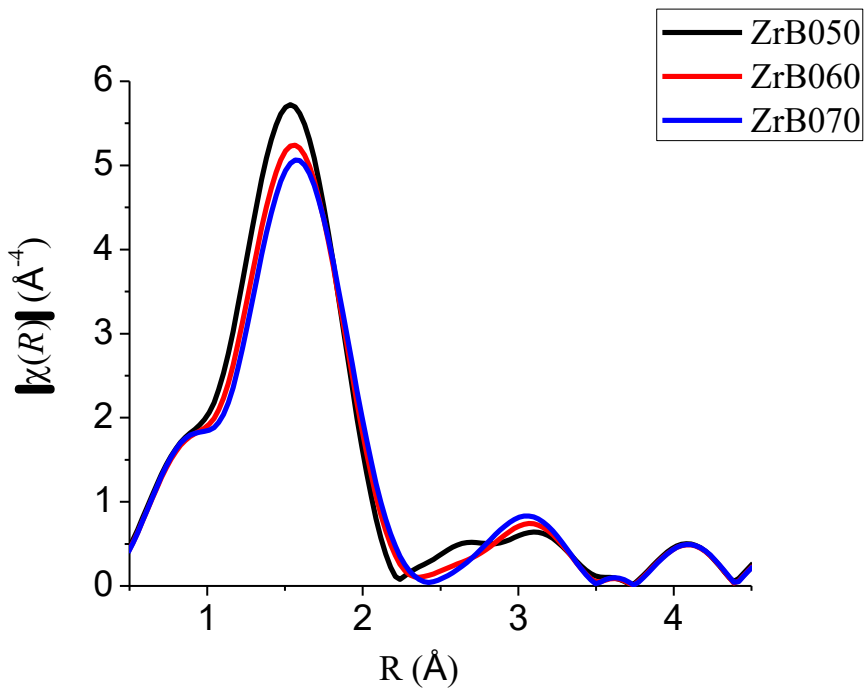
Figure 65. Comparison of Fourier transforms of $k^3\chi(k)$ (Å^{-3}) functions shown in Figure 64. The peaks around 1.6 Å indicate that the nearest neighbor oxygen coordination numbers (CN_{Zr-O}) increases with decreasing ZrO_2 content.
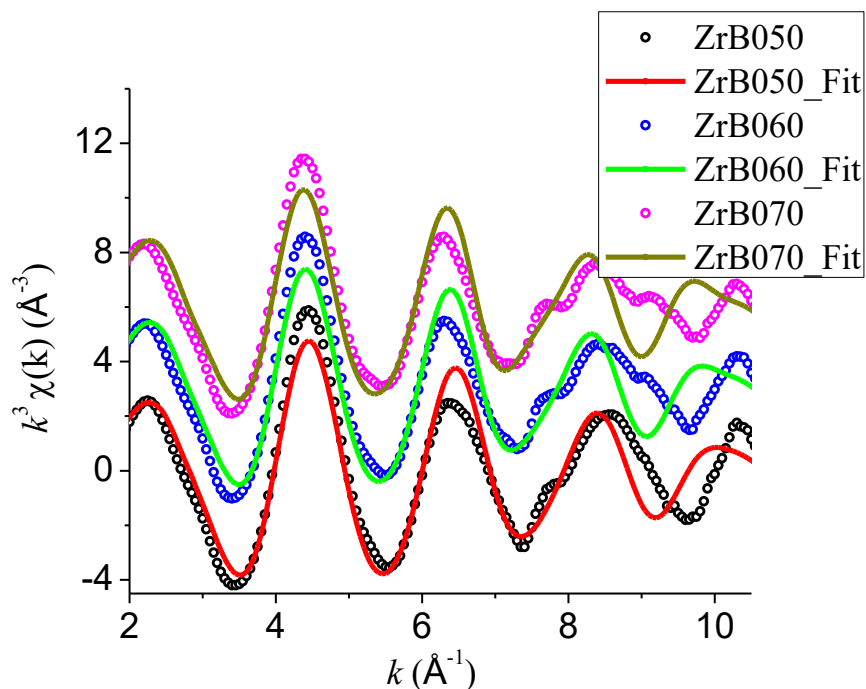
Figure 66. Experimental (dotted line) EXAFS functions $k^3\chi(k)$ (Å^{-3}) and their best fits (solid line) of zirconium-doped lithium borate samples with different compositions. The spectra and their fits are vertically separated by 3 Å^{-3} for clarity.
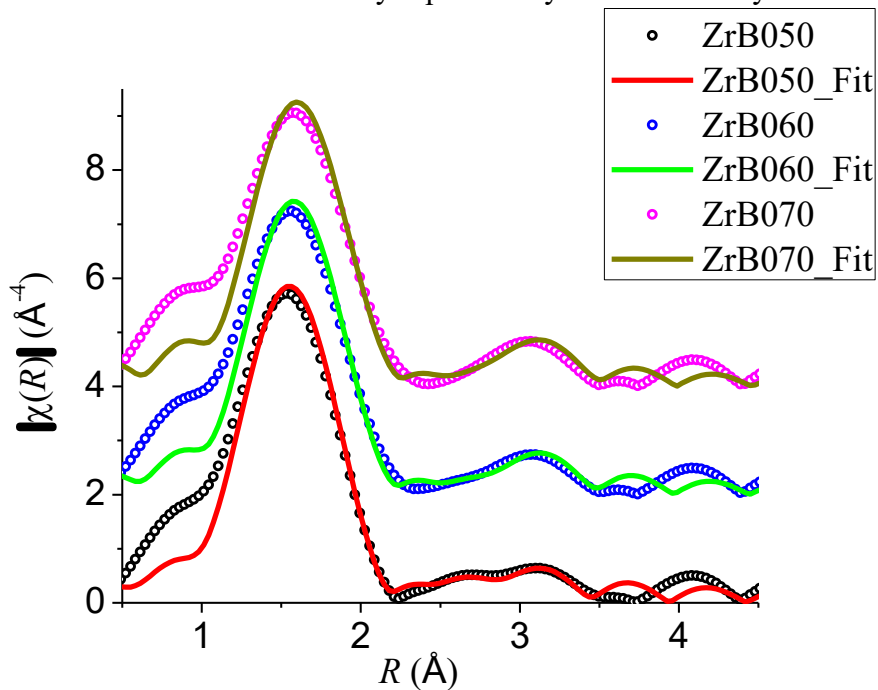
Figure 67. Fourier transforms of experimental (dotted line) EXAFS functions in *R*-space and their fits (solid lines). The spectra and their fits are vertically separated by 2 Å^{-4} for clarity.

Table 13. Structural parameters obtained for ZRLB samples. '*p*' represents ZrO_2, '*y*' represents B_2O_3.

Sample	Atomic shell correlation	CN	R (Å)	σ^2 (Å^2)
ZrB050	Zr-O(1)	6.83 ± 0.66	2.14 ± 0.02	0.010
p = 0.02	Zr-B and/or Li	4.71 ± 6.24	3.28 ± 0.02	0.008
y = 0.771	Zr-O(2)	6.51 ± 6.28	3.45 ± 0.02	0.015
ZrB060	Zr-O(1)	6.31 ± 0.58	2.16 ± 0.02	0.010
p = 0.038	Zr-B and/or Li	5.49 ± 5.08	3.31 ± 0.02	0.008
y = 0.780	Zr-O(2)	7.23 ± 5.17	3.50 ± 0.02	0.015
ZrB070	Zr-O(1)	6.13 ± 0.55	2.18 ± 0.02	0.010
p = 0.057	Zr-B and/or Li	5.93 ± 4.56	3.33 ± 0.02	0.008
y = 0.790	Zr-O(2)	8.03 ± 4.66	3.52 ± 0.02	0.015

The coordination shells are expected to be wider in ZRLS glasses due to dominant three-fold structure of $(BO_3)^{3-}$ (triangular or near trigonal planar structure) in borate glasses. **Table 13** shows the structural parameters determined by EXAFS analysis. For ZRLB glasses, $CN_{Zr-O(1)}$ of the first oxygen shell decreased from 6.83 to 6.13 as ZrO_2 content increased from 0.020 to 0.057. The Zr-O mean distance $R_{Nd-O(1)}$ increases from 2.14 to 2.18 Å as ZrO_2 content increases. Also, a wide Zr-O mean distance range is observed for the edge-sharing BO_4 tetrahedral structure in high-pressure phase *β-ZrB₂O₅* [36]. The values of Zr-O mean distance $R_{Nd-O(1)}$ are within the wide Zr-O mean distance range of 2.08–2.41 Å with the eight-fold oxygen coordination calculated by FEFF calculations for *β-ZrB₂O₅* (crystal structure of ternary zirconium borate at high pressure phase, synthesized under high-pressure / high-temperature conditions) [36]. The XAFS disorder factor σ^2 for these samples were higher than the case of ZRLS glass samples indicating that their structural disorder is greater.

A second borate shell was found at the distance of 3.28–3.33 Å, which is shorter than Zr-Si distance of 3.77 Å and within the Zr-B mean distance range of 2.90–3.40 Å

reported for β-ZrB_2O_5 [36]. The CN_{Zr-B} and the R_{Zr-B} tend to increase from 4.71 to 5.93 and from 3.28 to 3.33 Å, respectively, as ZrO_2 content increases. The CN_{Zr-B} is ranging from 4.71 to 5.93, which is smaller than the coordination number of 9 for β-ZrB_2O_5 [36] but higher than the CN_{Zr-Si} of 3.04–3.26 for ZRLS glasses. These results were expected because of the more disordered glass network (three-fold structure) of ZRLB glasses as compared to ZRLS glasses and smaller ionic radius of B^{3+} cations (0.41 Å for B^{3+} and 0.54 Å for Si^{4+}) [64].

A Zr-Zr path with degeneracy of one was calculated with a path distance of 3.44 Å from FEFF calculations of β-ZrB_2O_5 [36]. But due to low ZrO_2 content for these glasses, Zr contribution within the range of interest (< 4 Å) is excluded. Attempts were made to fit the second Zr-shell but they did not provide reasonable values. Also, expected Zr-Zr path contribution is low from the path degeneracy of one from the FEFF calculations of β-ZrB_2O_5 and low ZrO_2 content preclude the existence of Zr-O-Zr linkages for these glasses similar to the case of ZRLS samples. Best reasonable results were obtained by considering a B-shell as the second shell (Zr-O-B linkages) similar to the previous analysis for ZRLS samples. There may be some Zr-Zr clustering at higher ZrO_2 content but not within the ZrO_2 content range investigated in this study. Also, the contribution of Li atoms around 2.97 Å cannot be ruled out. Li atoms are expected near the fitted B-shell but due to the resolution limits for EXAFS, a Li coordination shell was not fitted.

EXAFS and XANES together imply that Zr coordination environment in these glasses is lower than seven-fold coordination in monoclinic-ZrO_2, but greater than six-fold coordination observed in ZRLS glass-ceramics. XANES suggested that there might be mixture of phases similar to that of six- and seven-fold coordination around Zr but the

Zr-O mean distance $R_{Nd-O(1)}$ range of 2.14–2.18 Å suggests the formation of a disordered structure different from monoclinic-ZrO_2 and zektzerite for ZRLB glasses.

5.4 Effect of the Composition and the Thermal Treatments

Figure 68 shows the Zr coordination numbers for the first oxygen shell as a functions of ZrO_2 content p. The effect of the composition on the Zr-O mean distances are plotted in **Figure 69**. ZrSi_1 represents ZRLS samples after the nucleation process and ZrSi_2 represents ZrSi_1 samples after the additional crystal growth process in **Figure 68 and 69**.
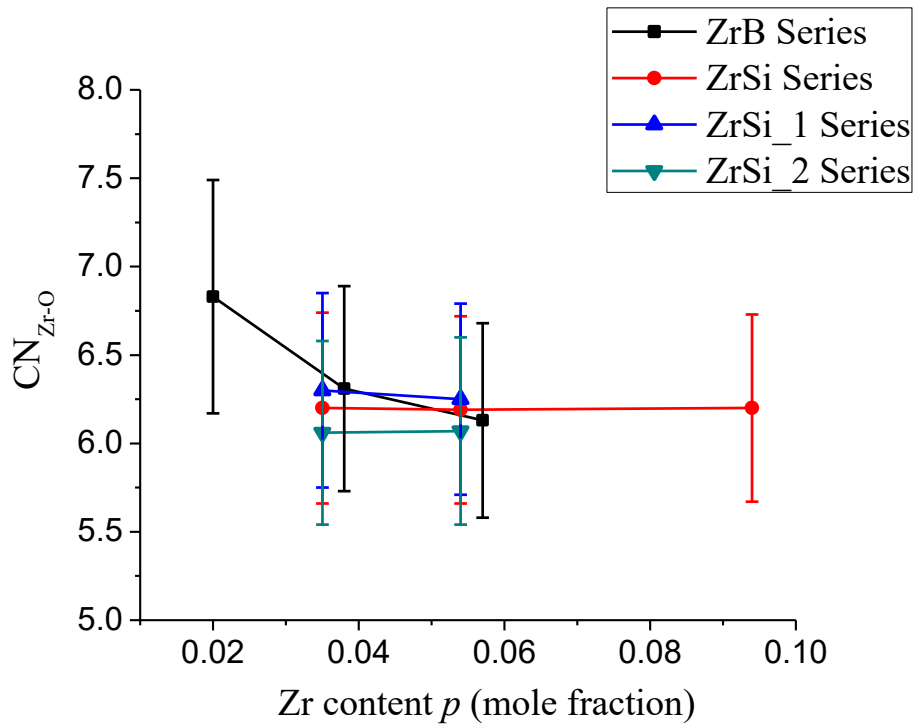
Figure 68. Effect of the composition and the thermal treatments on the first shell Zr-O coordination numbers.
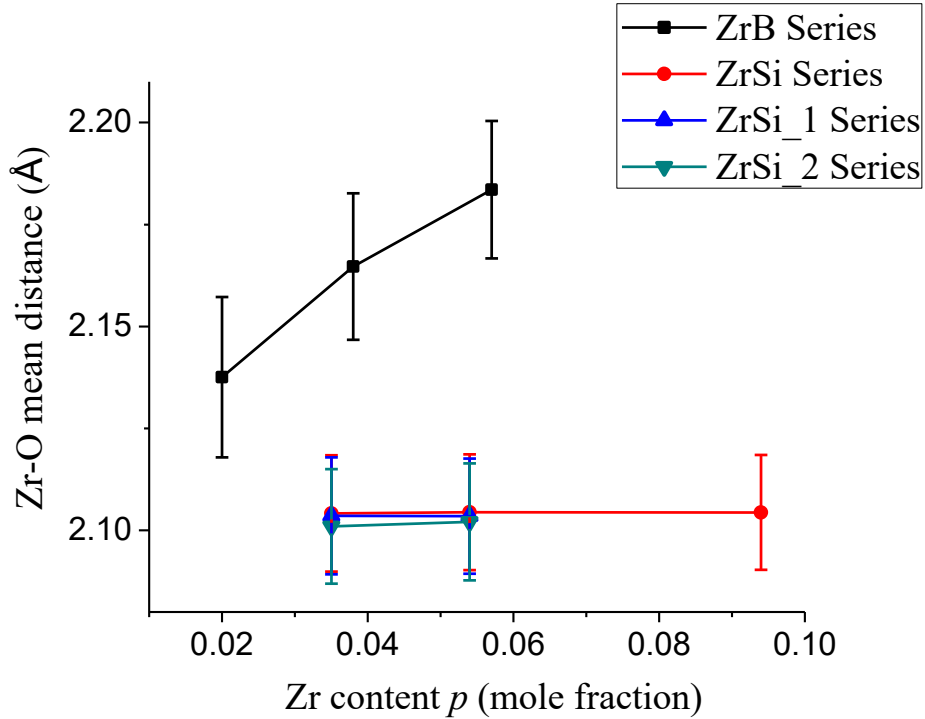
Figure 69. Effect of the composition on the Zr-O mean distances.

For ZRLS samples, composition dependence of the first shell oxygen coordination number and the distance is negligible within the investigated ZrO_2 content. However, noticeable changes in these parameters were observed in heat treated samples. ZRLS glass-ceramics from nucleation and crystal growth processes, generated a zirconium environment more similar to that in six-coordinated orthorhombic zektzerit. Low disorder parameter σ^2 (about 0.003 Å^2) for the first oxygen shell indicates that ZRLS glass samples were more ordered than ZRLB glasses.

Structural parameters of ZRLB samples show significant compositional dependence. As the ZrO_2 content increases, there is a decrease in CN_{Zr-O} and an increase in R_{Zr-O}. The coordination number CN_{Zr-O} is found to be vary between 6.13 to 6.83 depending on the ZrO_2 content, indicating two different oxidation structures resembling six-coordinated zektzerite and seven-coordinated monoclinic-ZrO_2, exist. Higher disorder

110

parameter σ^2 for the first oxygen shell indicates these samples were more disordered than ZRLS samples. Since vibrational (thermal) disorder factor was minimized by measuring ZRLS and ZRLB samples at 20 K, results indicate that structural disorder is low for ZRLS samples but it is high for ZRLB samples.

CHAPTER VI

CONCLUSIONS

The atomic-scale structure of rare-earth doped ultraphosphate glasses $(RE_2O_3)_x(Na_2O)_y(P_2O_5)_{1-x-y}$, where RE = Pr, Nd, Eu, Dy, and Eu ($0.005 \leq x \leq 0.130$ and $0.3 \leq x + y \leq 0.4$), has been investigated using the extended X-ray absorption fine structure (EXAFS) spectroscopy. The local environment of each RE^{3+} cations, such as coordination numbers, interatomic distances, disorder parameters, and their dependence on the concentration of the RE content, has been studied using RE L_{III}-edge (RE = Nd, Er, Dy, and Eu) and K-edge (RE = Pr and Dy) extended X-ray absorption fine structure (EXAFS) spectroscopy.

The nearest oxygen coordination number (CN_{RE-O}) is found to be vary between 6.5 to 10.3 depending on the type and concentration of RE. The RE-O coordination number increased from 6.5 to 10.8 with decreasing RE content for praseodymium, neodymium, and dysprosium, and erbium series. For europium-doped sodium phosphate glasses, Eu-O coordination number increased from 8.7 to 8.8 then decreased to 7.5 with increasing Eu_2O_3 content. For the first oxygen shell, the RE-O distances (R_{RE-O}) range between 2.43–2.45 Å, 2.43–2.40 Å, 2.38–2.36 Å, 2.35–2.30 Å, and 2.28–2.30 Å for praseodymium-, neodymium-, europium-, dysprosium-, and erbium-doped sodium phosphate glasses, respectively. The RE-O distance decreased with increasing RE content for praseodymium, neodymium, europium, and dysprosium samples. For erbium series, The Er-O distance decreased from 2.28 Å to 2.26 Å then increased to 2.30 Å with

increasing Er_2O_3 content possibly due to low signal-to-noise ratio. For praseodymium and erbium series, in investigated composition range of 0.5–5 mol%, signal-to-noise ratio was low due to low RE content where thickness requirement is quite large in order to make pellets (absorbers for EXAFS) for XAS measurement. Second shell around RE^{3+} cations consists of phosphorus atoms, with the RE-P distance about 3.63–3.80 Å for neodymium, europium, and dysprosium series with the second coordination number CN_{RE-O} ranging from 3.63 to 3.81. RE-RE correlation from clustering of RE atoms (RE-O-RE linkage) was not observed indicated by the high RE-O coordination number and the high number of terminal oxygens (TOs) for ultraphosphates.

The atomic-scale structure of zirconium-doped lithium silicate (ZRLS) glasses $(ZrO_2)_p(Li_2O)_q(SiO_2)_s$ in the compositional region of $0 \leq p \leq 0.10$, $0.25 \leq q \leq 0.30$, and $s = 1 - p - q$, two sets of ZRLS glass-ceramics after crystallization process (nucleation and crystal growth), and three zirconium-doped lithium borate (ZRLB) glasses $(ZrO_2)_p(Li_2O)_q(Al_2O_3)_r(B_2O_3)_{1-p-q-r}$ in the compositional region of $0.02 \leq p \leq 0.06$, $0.14 \leq q \leq 0.20$, and $0.00 \leq r \leq 0.01$, were investigated using Zr K-edge X-ray Absorption Spectroscopy (XAS). EXAFS and X-ray Absorption Near Edge Structure (XANES) spectroscopic analysis have been performed using zirconium K-edge XAS at 20 K.

In the case of ZRLS glass samples, XANES spectra exhibited the main peak features similar to those of six-fold coordinated zektzerite. EXAFS results for ZRLS glasses within the investigated compositional range (ZrO_2 content between 0.035–0.094) reveal that Zr coordination environment remains virtually unchanged for different amount of ZrO_2 content. During the glass to glass-ceramic conversion process, small changes

were observed. After the crystallization process, the nearest oxygen coordination number CN_{Zr-O} decreased from 6.2 to 6.1 while the average Zr-O distance (R_{Zr-O}) remained similar around 2.10 Å with a very small deduction observed less than 0.004 Å. For heat treated samples the local structure around Zr is similar to zektzerite.

In contrast, immediate coordination environment of ZRLB glasses appear to change markedly with the zirconium concentration. Observation from XANES spectra, suggests that zirconium coordination environment is between the monoclinic-ZrO_2 and ZRLS glasses which suggests the presence of two different zirconium environment mixed in ZRLB glasses. Parameters obtained from EXAFS indicate that zirconium coordination environment depends on ZrO_2 content. The nearest oxygen coordination number (CN_{Zr-O}) decreased from 6.8 to 6.1 and the average Zr-O distance increased from 2.14 to 2.18 Å with increasing ZrO_2 content. The change in average Zr-O distance from 2.14 to 2.18 Å from EXAFS suggest that zirconium coordination environment in these glasses have an amorphous local environment different from monoclinic-ZrO_2 and zektzerite. These results indicate that the structural role of Zr^{4+} cations in ZRLS and ZRLB glasses may be significantly different.

REFERENCES

[1] Shelby, J. E. (1997). *Introduction to glass science and technology, Royal Society of Chemistry*, Cambridge.

[2] Paul, A. (1982). *Chemistry of Glasses*, New York; Chapman and Hall

[3] Campbell J. H. & Suratwala, T. I. (2000). *Nd-doped phosphate glasses for high-energy/high-peak-power lasers*, J. Non-Cryst. Solids, 263&264 p. 318-341.

[4] Bach, H., Neurot, N. (1998). *The Properties of Optical Glass*, Springer Verlag.

[5] Weber, M.J. (1990). *Science and technology of laser glass*, J. Non-Cryst. Solids 123 208-222.

[6] Weber, M.J. (1979). *Handbook on the Physics and Chemistry of Rare Earths*, Vol.4, eds K.A Gschneidner Jr and L Eyring, North-Holland, Amsterdam, Ch. 35.

[7] Cole, J. M., Newport, R. J. (2007). *Direct observation of the R − R separation in rare-earth phosphate glasses*", J. Non-Cryst. Solids 353, 1773.

[8] Casasola, R., Rincón, J. Ma., Romero, M. (2012). *Glass-ceramics glazes for ceramic tiles – a review*, Journal of Material Science, 47, 553-582.

[9] Hoppe, U., Brow, R. K., Ilieva, D., Jovari, P., and Hannon, A. C. (2005), J. Non-Cryst. Solids, 351, 3179.

[10] Galoisy, L., Pélegrin, E., Arrio, M.-A., Ildefonse, P., Calas, G., Ghaleb, D., Fillet, C., & Pacaud, F. (1999). *Evidence for 6-Coordinated Zirconium in Inactive Nuclear Waste Glasses*, Journal of the American Ceramic Society, 82: 2219–2224.

[11] Kingery, W. D., Bowen, H. K., & Uhlmann, D. R. (1976). *Introduction to ceramics*, J. Wiley & Sons, New York.

[12] Brow, R. K. (2000). *Review: the structure of simple phosphate glasses,* J. Non-Cryst. Solids 263&264, 1.

[13] Liebau, F. in: Keefe, M., & Novortsky, A. (Eds.), (1981). *Structure and Bonding in Crystals II*, Academic Press, New York.

[14] Karabulut, M., Metwalli, E., Wittenauer, A. K., Brow, R. K., Marasinghe, G. K., Booth, C. H., Bucher, J. J. & Shuh, D. K. (2005). *An EXAFS investigation of rare-earth local environment in ultraphosphate glasses*, J. Non-Cryst. Solids 351 (2005) 795.

[15] Gunapala, E. S. (2011). *A study of the atomic structure of vitreous rare earth phosphates using high energy X-ray diffraction technique*, Ph.D thesis, UND.

[16] Bunker, G. (2010). *Introduction to XAFS: A Practical Guide to X-ray Absorption Fine Structure Spectroscopy,* Cambridge University Press.

[17] Koningsberger, D. C., Prins, R., ed., (1988). *X-ray absorption : principles, applications, techniques of EXAFS, SEXAFS, and XANES*, In Chemical Analysis Vol. 92, D. C., John Wiley & Sons.

[18] Calvin, S. (2013). *XAFS for Everyone*, CRC Press

[19] Sayers, D.E., Stern, E.A., & Lytle, F. (1971). *New Technique for Investigating Noncrystalline Structures: Fourier Analysis of the Extended X-Ray-Absorption Fine Structure*, Phys. Rev. Lett. 27, 8, 1204-1207.

[20] Stern E.A., (1974). *Theory of the extended X-ray-absorption fine structure*, Physical Review B10: 3027-3037.

[21] Lytle, F. W., Sayers, D. E., Stern, E. A. (1975). *Extended X-ray-absorption fine-structure technique. II. Experimental practice and selected results*, Physical Review B 11: 4825-4835. DOI:http://dx.doi.org/10.1103/PhysRevB.11.4825

[22] Newville, M. (2010). *EXAFS Analysis*, Consortium for Advanced Radiation Sources, Univ. of Chicago.

[23] Ravel, B. & Newville, M. (2005). *ATHENA, ARTEMIS, HEPHAESTUS: data analysis for X-ray absorption spectroscopy using IFEFFIT,* Journal of Synchrotron Radiation 12, 537–541. doi:10.1107/S0909049505012719

[24] Khalid, S. (2008, October 30). *XAFS Instrumentation and Sample Preparation workshop.* Retrieved from http://www.bnl.gov/ps/nsls/workshops/2008/exafs/files/4_Khalid.pdf

[25] NSLS EXAFS workshop, (2003). Retrieved from http://xafs.org/Workshops/NSLS2003?action=AttachFile&do=get&target=Calvin.pd

[26] Newville, M., (2001). *IFEFFIT*: *interactive XAFS analysis and FEFF fitting*, Journal of synchrotron radiation 8 (2), *322-324*.

[27] Ravel R., *ATHENA User's guide, (ATHENA XAS data processing).* Retrieved from http://cars9.uchicago.edu/~ravel/software/doc/Athena/html/params/e0.html

[28] Newville, M., Livins, P., Yacoby, Y., Stern, E. A., & Rehr, J. J. (1993). *Near-edge x-ray-absorption fine structure of Pb: A comparison of theory and experiment*, Phys. Rev. **B**47, 14126-14131.

[29] Kelly, S. *Basics of EXAFS data analysis.* Retrieved from http://xafs.org/Tutorials?action=AttachFile&do=get&target= Basics_of_XAFS_to_chi.pdf

[30] Zhang, K., Stern, E. A., Rehr, J. J., & Ellis, F. (1991). *Double electron excitation in atomic Xe*, Phys. Rev. B44, 2030.

[31] Kodre, A., Arcon, I., Padeznic, J., Preseren, R., & Frahm, R. (2002). *Multielectron excitations in X-ray absorption spectra of Rb and Kr*, J. Phys. B **35**, 3497-3513.

[32] Salem, S. I., Kumar, A., & Lee, P. L. (1982). Phys. Rev. A 25, 2069.

[33] Bianconi, A., Garcia, J., Benfatto, M., Marcelli, A., Natoli, C. R., & Ruiz-Lopez, M. F. (1991). Phys. Rev. B 43, 6885.

[34] Mountjoy, G., Pickup, D. M., Anderson, R., Wallidge, G. W., Holland, M. A., Newporta, R. J., & Smith, M. E. (2000). *Changes in the Zr environment in zirconia-silica xerogels with composition*, Phys. Chem. Chem. Phys., 2, 2455-2460.

[35] Ohta, A., Kagi, H., Tsuno, H., Nomomura, M., & Kawabe, I. (2008). *Influence of multi-electron excitation on EXAFS spectroscopy of trivalent rare-earth ions and elucidation of change in hydration number through the series,* American Mineralogist, Volume 93, pages 1384–1392.

[36] Knyrim, J. S. & Huppertz, H. (2008). *High-pressure Synthesis, Crystal Structure, and Properties of the First Ternary Zirconium Borate β-ZrB$_2$O$_5$*, Z. Naturforsch. 63b, 707 –712.

[37] Hemantha, A. (2011). *An X-ray absorption study of the atomic structure of novel vitreous rare-earth phosphates*, A Ph.D. Dissertation, University of North Dakota.

[38] Ganegoda, H. (2006). *An Extended X-ray Absorption Fine Structure Study of Rare Earth Phosphate Glasses*, A Master's Thesis, University of North Dakota.

[39] Jouini, A., Ferid, M., Gacon, J. C., Grosvalet, L., Thozet, A., & Trabelsi – Ayadi, M. (2003). *Crystal Structure and Optical Study of Praseodymium Polyphosphate Pr(PO3)3*, Mater. Res. Bull., 38 [11–12] 1613–22.

[40] Anderson, R., Brennan, T., Cole, J. M., Mountjoy, G., Pickup, D. M., Newport, R. J., & Saunders, G. A. (1999). *An extended x-ray absorption fine structure study of rare-earth phosphate glasses near the metaphosphate composition*, J. Mater. Res., Vol. 14, No. 12.

[41] Zhang, K. (2012). *A high energy X-ray diffraction investigation of sodium phosphate glasses doped with less than 5 Mol% praseodymium oxide*, A Master's Thesis, University of North Dakota.

[42] Koizumi, H. (1976). *Sodium neodymium metaphosphate Na Nd P4 O12*, Acta Crystallographica B (24,1968-38,1982) 32, 2254-2256.

[43] Bowron, D.T., Saunders, G.A., Newport, R.J., Rainford, B.D., & Senin, H.B. (1996). *EXAFS studies of rare-earth metaphosphate glasses,* Phys. Rev. B 53, 5268.

[44] Gunapala, E. S. (2011). *A study of the atomic structure of vitreous rare earth phosphates using high energy X-ray diffraction technique*, A Ph.D. dissertation, University of North Dakota.

[45] Karabulut, M., Marasinghe, G. K., Metwalli, E., Wittenauer, A. K., Brow, R. K., Booth, C. H., & Shuh, D. K. (2002). *Neodymium and erbium coordination environments in phosphate glasses*, Phys. Rev. B 65, 104206.

[46] Ni, Y., Hughes, J.M., Mariano, A.N. (1995). *Crystal chemistry of the monazite and xenotime structures,* American Mineralogist, 80, p.21-26.

[47] Bowron, D.T., Newport, R.J., Rainford, B.D., Saunders, G.A., & Senin, H. B. (1995). *EXAFS and x-ray structural studies of $(Tb_2O_3)_{0.26}(P_2O_5)_{0.74}$ metaphosphate glass*, Phys. Rev. B 51, 5739.

[48] Anderson, R., Brennan, T., Cole, J. M., Mountjoy, G., Pickup, D. M., Newport, R. J. & Saunders, G. A. (1998). *An extended x-ray absorption fine structure study of rare-earth phosphate glasses near the metaphosphate composition*, J. Non-Cryst. Solids 232-234, 286-292.

[49] Milligan, W.O., Mullica, D.F., Beall, G.W., & Boatner, L.A. (1983). *The structures of three lanthanide orthophosphates,* Inorganica Chimica Acta. 70, 133-136,

[50] Maksimova, S. I., Masloboev, V. A., Palkina, K. K., Sazhenkov, A. A., & Chibiskova, N. T. (1988). *Preparation and structure of sodium erbium polyphosphate, NaEr(PO3)4*, Zhurnal Neorganicheskoi Khimii, 33, 2503-2505.

[51] Hoppe, U. (1996). *A structural model for phosphate glasses*, Journal of Non-Crystalline Solids, vol. 195, no. 1-2, pp. 138–147. doi:10.1016/0022-3093(95)00524-2

[52] Mercier, C., Montagne, L., Sfihi, H., Palvit, G., & Boivin, J.C. (1998). Journal of Non-Cryst. Solids 224, 163.

[53] Housecroft, C. E.; Sharpe, A. G. (2004). *Inorganic Chemistry* (2nd ed.). Prentice Hall. pp. 536, 649, 743.   ISBN 978-0130399137

[54] Robinson, K., Gibbs, G. V., & Ribbe, P.H. (1971). *The structure of zircon: A comparison with garnet*, Am. Mineral. Vol. 56, 782-790.

[55] Louvel, M., Snachez-Valee, C., Malfait, W. J., Testemale, D., & Hazemann, J. L. (2013). *Zr complexation in high pressure fluids and silicate melts and implications for the mobilization of HFSE in subduction zones*, Geochimica et Cosmochimica Acta 104.

[56] Meneghetti, F., Wendel, E., Mascotto, S., Smarsly, B. M. Tondello, E., Bertagnolli, H., & Gross, S. (2010). *Combined use of XAFS, XRD and TEM to unravel the microstructural evolution of nanostructured ZrO_2–SiO_2 binary oxides: from nanometres down to the molecular domain*, CrystEngComm, 12, 1639–1649. doi: 10.1039/b911004f

[57] Connelly, A.J., Hyatt, N.C., Travis, K.P., Hand, R.J., & Maddrell, E.R. (2011). *Predicting the preference for charge compensation in silicate glasses,* Phys. Chem. Glasses-Eur. J. Glass Sci. Technol. Part B 52, 64-67.

[58] Farges, F. (1996). *Does Zr–F ''complexation'' occur in magmas?*, Chem. Geol. 127, 253–268.

[60] Finger, L.W., (1974). *Refinement of the Crystal Structure of Zircon,* Carnegie Institution of Washington: Yearbook, 73, 544-547.

[61] Smith, D. K., Newkirk, H. W. (1965). *The crystal structure of baddeleyite (monoclinic ZrO_2) and its relation to the polymorphism of ZrO_2*, Journal of publication, Acta Crystallographica, Vol. 18, p983 – 991.

[62] Ghose, S., Wan, C. (1978). *Zektzerite, Na Li Zr Si6 O15: a silicate with six-tetrahedral-repeat double chains, American Mineralogist*, 63, 304-310.

[63] Caurant, D., Quintas, A., Majerus, O., Loiseau, P., Charpentier, T., Vermaut, P., & Dussossoy, J. (2010). *Structural and Crystallization Study of a Simplified Aluminoborosilicate Nuclear Glass Containing Rare-earths: Effect of ZrO_2 Concentration.* MRS Proceedings, 1265, 1265-AA03-02. doi:10.1557/PROC-1265-AA03-02.

[64] Shannon, R. D. (1976). *Revised effective ionic radii and systematic studies of interatomic distances in halides and chalcogenides,* Acta Crystallogr A 32: 751–767. doi:10.1107/S0567739476001551.

[65] Askeland, D. R., Phule, P. P., (2006). *The Science and Engineering of Materials*, 5th Edition, Thomson

[66] Smekal, A. (1951). *On the structure of glass.* Journal of Glass Technology 35:392-94.